TESIS DOCTORAL

Nonlinear effects in low-dimensional systems: graphene membrane and electron transport in semiconductor superlattices

Autor:

Miguel Ruiz García

Directores:

Luis L. Bonilla

Antonio Prados

Instituto Gregorio Millán Barbany
Departamento de Ciencia e Ingeniería de Materiales e Ingeniería Química

Leganés, septiembre de 2017

TESIS DOCTORAL

Nonlinear effects in low-dimensional systems: graphene membrane and electron transport in semiconductor superlattices

Autor: Miguel Ruiz García

Directores: Luis L. Bonilla y Antonio Prados Montaño

Firma del tribunal calificador:

	(Nombre y Apellidos)	Firma
Presidente:		
Vocal:		
Secretario:		

Calificación:

Leganés, de de

A mis padres, Teresa y Paco.
A ti, Carmen.

Acknowledgments

This thesis has been carried out in the Modelling and Numerical Simulation Group within the Department of Materials Science and Gregorio Millán Institute, at Universidad Carlos III de Madrid (UC3M). I have been really fortunate to work under the supervision of my Ph.D. advisors Luis L. Bonilla (UC3M) and Antonio Prados (Universidad de Sevilla). They provided me with an excellent environment for my studies, introduced me to very interesting and challenging problems, guided me through obstacles, and most importantly, taught me how to work and develop scientific research.

I came to Madrid in 2012, after my Physics undergraduate studies in University of Seville (2007-2012). During the first year I studied a Master Degree in Materials Science and Engineering (UC3M), which helped me becoming familiar with experimental techniques that are extensively used in graphene studies. After that, this PhD work was developed form fall 2013 to summer 2017. I am really thankful to my advisors for their help and support guiding me during the sometimes slightly discouraging and most often extremely delayed process of applying for PhD fellowships to the Spanish government. If it were not for the alternative funding that Luis provide me during more than one year while we were waiting for the final decision of the Formación de Profesorado Universitario (FPU) fellowship I would not have been able to complete this thesis. I really appreciate it.

I gratefully acknowledge financial support from:

- Spanish Ministerio de Educación Cultura y Deporte (MEC) through the FPU program.

- Spanish Ministerio de Economía y Competitividad (MINECO) Grant No. MTM2014-56948-C2-2-P and FIS2011-28838-C02-01 and Comunidad de Madrid Grant No. P2009/ENE-1597(HYSYCOMB).

- MINECO–Residencia de Estudiantes fellowship.

- UC3M through the Personal Investigador en Formación program and for the funding received for a research stay at University of California, Santa Barbara.

- Prof. Andrej Košmrlj for funding my position at Princeton University as a Visiting Student Research Collaborator.

- Prof. Björn Birnir for partially funding my stay at University of Iceland.

- Institute for Advanced Study and Park City Mathematics Institute for the funding received to attend the 2014 summer session.

One of the things that I have enjoyed the most during this process it is the interaction with so many different people. Many of them are amazing scientists that have influenced my way to see the world. I have to stress my attendance to the IAS/PCMI 2014 summer session and the research stays that I did in University of Iceland (Reikiavik, Iceland), University of California, Santa Barbara (Santa Barbara, CA, USA), École Normale Supérieure (Paris, France) and Princeton University (Princeton, NJ, USA). I am very thankful for the hospitality received from my stay advisors, Björn Birnir, Pierre Le Doussal and Adrej Košmrlj, I have learnt a great deal with them and they have been really productive experiences.

Finally, the collaborations with Profs. Holger T. Grahn, Francisco Guinea and John C. Neu have also been really insightful experiences that I hope will continue in the future.

Agradecimientos

Quiero reunir aquí a las personas que han hecho que este proceso que ahora termina haya sido una experiencia estupenda. Seguro que olvido a alguien, por favor, perdóname.

En primer lugar, quería mencionar de nuevo a mis directores de tesis, Luis y Antonio, porque, además de guiarme e instruirme durante este proceso, sé que he ganado dos buenos amigos.

El ambiente de trabajo en nuestro grupo en la UC3M no podía ser mejor. De estos años me llevo un gran recuerdo de la experiencia compartida con todos sus miembros, desde los profesores -Manuel, Jesús, Eduardo, Jose María- a los compañeros -Filipo, Víctor, Andrés, Mario, David, Pedro, Gil, Jacobo, Sergei, Rafa, Emanuel, Rocío, Carolina y Antonio-. Sé que contaba con el apoyo de todos, pero no hubiera sido lo mismo sin Juan y Carlos.

Las estancias son también un periodo especial, donde el tiempo pasa un poco más lento, para lo bueno y para lo malo. Mucha gente ayudaron a que estas experiencias fueran más divertidas, principalmente alrededor del equipo de remo de UCSB, el Colegio de España en París y los VSRC de Princeton. Mi mayor alegría es saber que conservo amigos de cada unos de estos sitios, Ryan, Christian, Paula, Gonzalo, Tristan y Markus.

El último año de tesis viví en la Residencia de Estudiantes. Esta experiencia fue intensa y sé que la llevaré conmigo donde vaya. Paco, María Elena, Ana, José Manuel, Álvaro, Arantxa, Miguel, Pilar, Óscar (x2), Paula, Sergio, Raphael, Miryam, Laura y Diego, muchas gracias por todo, aunque perdamos el contacto espero que sigamos conservando el cariño. Juan también estaba aquí, qué suerte, sin ironía :)

Tengo la suerte de poder contar con mucha gente fuera de todo lo que rodea una tesis. Principalmente Javi y Eli, con su cariño y amistad a pesar de la distancia, sé que siempre podré contar con vosotros.

Todo lo que he sido y soy se lo debo a mis padres. Incluida la independencia de la que a veces he abusado. Gracias, os quiero mucho.

Carmen, tú eres mi futuro, a ti, te lo diré al oído.

Preface

This PhD dissertation deals with two different topics: Mechanics of graphene from a statistical mechanics approach, where internal interactions and effects due to temperature are considered. And electron dynamics and chaos in semiconductor superlattices, where we aim at enhancing the chaotic behavior, with its applicability to random number generation in mind.

It is not our purpose to bridge these two different topics. But we do believe that with the rise of nanotechnology and the ever-increasing interdisciplinary of science, studies where different topics are approached and discussed are highly desirable.

Nanotechnology already rules our life. However, it is still surprising how much progress has been achieved without a fully understanding of the physics governing these structures. In particular, out-of-equilibrium behavior and non-linear responses are present in every nanostructure, but, sometimes, it is possible to avoid their effects at large time scales or small interactions. However, the increasing demand of better and/or new performances makes them sometimes unavoidable, or even, desirable.

Micro-metric samples of graphene or semiconductor superlattices cannot be studied taking into account every microscopic interaction, which makes it necessary to use mesoscopic models with a certain range of validity. Throughout this work, we have tried to improve our understanding of the topics stated above, using mesoscopic physical models and techniques from statistical mechanics and dynamical systems. We hope that the obtained results will help the scientific community to gain insight into these fascinating topics and will motivate new research in this direction.

List of publications

This thesis contains, at least partially, the work appeared in the following papers:

- **Ruiz-Garcia, M**, Essen, J, Carretero, M, Bonilla, L L, and Birnir, B, *Enhancing chaotic behavior at room temperature in GaAs/(Al,Ga)As superlattices*, Physical Review B, **95**, 085204 (2017)
- Yin, Z, Song, H, Zhang, Y, **Ruiz-Garcia, M**, Carretero, M, Bonilla, L L, Biermann, K and Grahn, H T, *Noise-enhanced chaos in a weakly coupled GaAs/(Al,Ga)As superlattice*, Physical Review E, **95**, 012218 (2017).
- **Ruiz-Garcia, M**, Bonilla, L L, and Prados, A, *STM-driven transition from rippled to buckled graphene in a spin-membrane model*, Physical Review B, **94**, 205404 (2016).
- Bonilla, L L, **Ruiz-Garcia, M**, *Critical radius and temperature for buckling in graphene*, Physical Review B, **93**, 115407 (2016).
- **Ruiz-Garcia, M**, Bonilla, L L, and Prados, A, *Ripples in hexagonal lattices of atoms coupled to Glauber spins*, J. Stat. Mech.: Theor. Exp., P05015 (2015)
  Highlighted in Revista Española de Física, 29 (3), 26 (2015).

Contents

Chapter 1

Introduction

1.1 Statistical approaches to mechanics of graphene

1.1.1 Graphene

Most people have heard something about graphene, like its extraordinary mechanical and electronic properties or the amazing fact that it is a one-atom thick crystal membrane. Hearing about the process that lead to its discovery through the Nobel Lecture of A. K. Geim [61] may be one of the most encouraging and also fun experiences. In this story, Geim tells us about his previous research experience, revisit his successes and failures, and points to the "thought clouds" that brought him and his team to the measure of a metallic field effect which switched between $2D$ electron and hole gases by changing the gate voltage on few layers of atomic-thick graphite samples [109], the *Science* paper which marks the birth of graphene, see figure 1.1.

Due to the existent vast literature about graphene, we will outline here only some of its main features. Graphene is a one-atom-thick crystal in which atoms are ordered on a hexagonal periodic lattice. Each atom is bounded to its three nearest-neighbors through covalent bonds, therefore, the remaining electron from the four valence electrons of every carbon atom is unbounded. The atomic orbitals of carbon atoms hybridize in a sp^2 configuration, where the three ones that will form covalent bonds with their nearest-neighbors are included in a plane and the unbound electron occupies an orbital perpendicular to this plane, see figure 1.2.

The chemical structure of graphene, and mainly the geometry of its orbitals, is the main reason for the high conductivity (or electron mobility) of graphene. The electron mobility excess of 200000 cm^2 V^{-1} s^{-1} at electron densities of $\sim 2\ 10^{11}$ cm^{-2} [18].

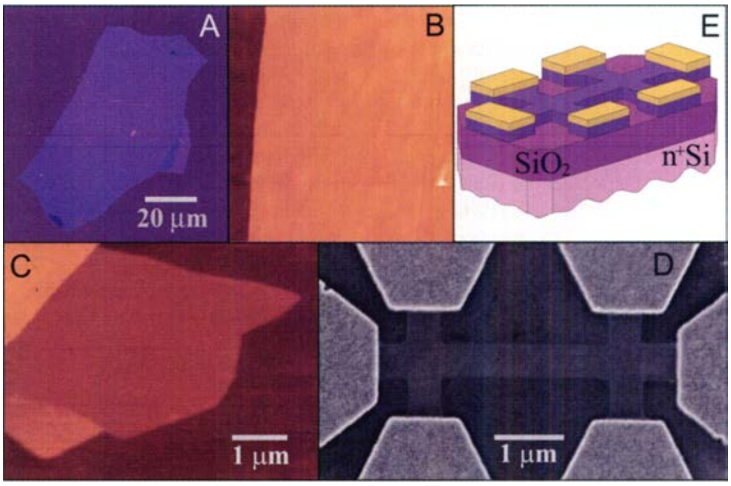

Figure 1.1: Different images reprinted from [109]. A) Photograph (in normal white light) of a relatively large multilayer graphene flake with thickness $\sim$ 3 nm. B and C) AFM images of multilayer and monolayer graphene, respectively. D and E) Scanning electron microscopy and schematic view of the device used to measure electric properties of graphene.

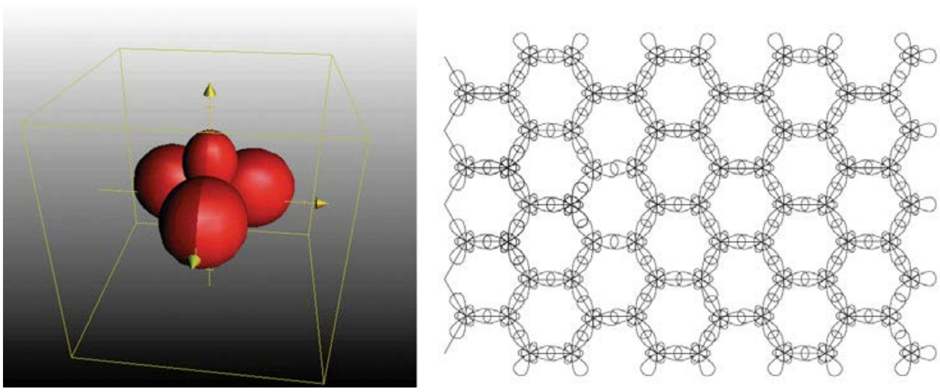

Figure 1.2: Sketch of the sp^2 hybridization of carbon orbitals in graphene. The left panel shows the electron probability distribution in the different orbitals for a sp^2 hybridization. The right panel depicts the hexagonal lattice of graphene, where atomic orbitals are overlapping to form covalent bonds. Reprinted from [38]

.

One of the most famous features of graphene is the linear dispersion relation of its charge carriers close to the vertices of its hexagonal Brillouin zone, which gives them the denomination of Dirac fermions. This feature was theoretically derived in the 40's by Wallace to understand the band structure of graphite [140]. Using a nearest-neighbor tight-biding approach, in which the Hamiltonian of the crystal is computed taking into account orbital overlapping only between nearest-neighbors, and diagonalizing this operator, one can obtain the famous Dirac points of graphene band structure, see figure 1.3. For more detailed derivations of the tight-biding approach consult [38, 82, 126].

Even though electronic properties of graphene are its most famous feature, its mecanical properties are also really unique. Its Young modulus it is estimated to be $E \approx 1$ terapascals, obtained using the effective thickness ~ 3.4Å of graphene from the value of the 2D Young modulus $Y \approx 340$ Nm^{-1} [89]. That establishes graphene as the strongest material ever measured. In contrast, its bending rigidity is estimated around $\kappa \approx 1$ eV [50]. This makes graphene an extremely difficult to stretch material, but very easily bendable. Then, thermal fluctuations are expected to play an important role for graphene. In addition, mechanical effects as rippling or bending are also discussed in this introduction.

1.1.2 Thermal fluctuations

The same as graphene has been a 'CERN on one's desk' for relativistic quantum phenomena, taking advantage of its linear dispersion relation (effectively massless particles). It is expected to be a real testbed for the role of thermal fluctuations in the effective modification of the mechanical properties of membranes.

The first surprising fact in relation with graphene and thermal fluctuations is the mere existence of this material. The divergence of out-of-plane fluctuations for $2D$ soft membranes [41, 104] can be interpreted as the impossibility of producing stable $2D$ membranes at room temperature. Before graphene, researchers always found impossible to produce nanometric thick materials, see for example [49]: in the process of producing these ultra-thin materials, they would coagulate forming islands and mounds.

However, graphene is always produced as part of a $3D$ structure, either peeling it form bulk graphite or growing it epitaxially on a substrate, which quenches thermal fluctuations. This process enables it to avoid the crumpling instability. Once a mono-layer is created, this crystalline membrane can be placed on a different substrate, whose van der Waals forces will prevent it

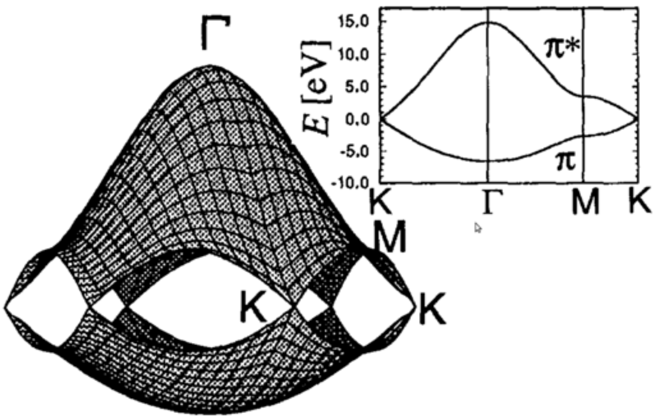

Figure 1.3: Figure containing the main ingredients to compute the linear dispersion relation in graphene. Top panel shows: on the left, hexagonal lattice of graphene with unit vectors $\mathbf{a_1}$ and $\mathbf{a_2}$, and unit cell containing two different kind of atoms A and B and, on the right, Brillouin zone in the reciprocal lattice (Fourier space), unit vectors $\mathbf{b_1}$ and $\mathbf{b_2}$ and high symmetry points Γ, M and K. Bottom panel contains graphene band structure in the tight-binding approximation, high symmetry points are also depicted. A linear relation close to K points is shown. Reprinted from [126].

from rolling. In order to study the mechanical properties of graphene without the interactions with a substrate, the graphene sheet is usually placed on a substrate with holes. In this way, the suspended regions show interesting features as rippling or buckling, which are discussed in section 1.1.3.

An enlightening approach to find out the effect of thermal fluctuations in graphene is that of a momentum shell renormalization group (RG) procedure, for more details see [7, 79]. It is easy to imagine that for *high enough* temperature elastic equations (and its static solutions) are no longer valid. Our system, instead of being at a stationary configuration, following for example Föppl-von Kármán equations in the case of a thin shell, will be fluctuating around this configuration (the one that minimizes its elastic energy). These fluctuations will follow the typical Boltzmann factor for the probability of configurations at thermal equilibrium,

$$\mathcal{P} \propto e^{-\frac{F}{k_B T}}, \tag{1.1}$$

where F is the elastic energy of the system and k_B and T stand for the Boltzmann constant and temperature, respectively. An intuitive picture of the RG approach can be thought as one way to keep using the same expressions for the elastic (stationary) equations, once thermal fluctuations are taken into account. Specifically, short-range deformations of our membrane (more susceptible to thermal fluctuations) are integrated out of the elastic energy F giving rise to a new effective elastic energy that conserves the same form (thus conserving the elastic equations through a variational principle). To accomplish that, the elastic constants are redefined (renormalized) to new effective values. These new values of the elastic constants could be measured in experiments for large enough systems or at high enough temperature. The thermal length scale at which this renormalization process start to be important it is the inverse of the characteristic wave vector [121],

$$q_c = \sqrt{\frac{3k_B TY}{8\pi\kappa}}, \tag{1.2}$$

which for graphene is ~ 0.24 Å. That means that thermal fluctuations will always be important in suspended graphene. Estimates using the results of [10, 103] predict a stiffening of thermalized membranes, which would behave (at high temperature/large systems) as having an effective bending rigidity much bigger than the microscopic, "bare", value.

Recent measurements of graphene bending rigidity account for values much greater than the microscopic bending rigidity $\kappa \approx 1$ eV, see figure 1.4. Blees *et al.* [17] postulate that this effect can be produced by a combination

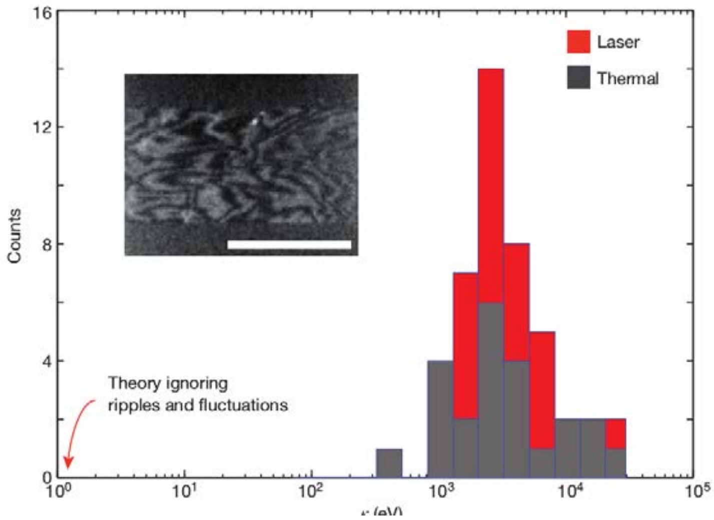

Figure 1.4: Stacked histogram of bending stiffness using two different techniques. The graphene monolayer had two gold pads to which a force could be applied using a laser beam. Alternatively, κ could be determined measuring the thermal fluctuations of one of the pads. Inset: Interference micrograph showing the structure of static ripples. Scale bar is 10 μm. Interference images were averaged over 180 frames at 90 frames per second. The red arrow points to the value of the microscopic bending rigidity. Reprinted from [17].

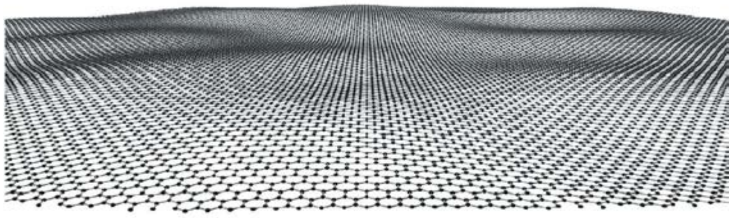

Figure 1.5: Perspective view of corrugated graphene. The roughness shown imitates quantitatively the roughness found experimentally. Reprinted from [99].

of the effect of thermal fluctuations and stable ripples, however their results are not conclusive in this aspect.

The use of a renormalization group approach is appealing and could explain the effective behavior at large scales compared with the system size (once short-range effects have been integrated out). Notwithstanding, there are some features that make it necessary to consider other complementary approaches: for example, out-of-equilibrium dynamics and the presence of stationary ripples, which could be explained by taking into account the coupling of internal degrees of freedom with the membrane strain tensor. These features are two of the motivations for chapters 3, 4 and 5.

1.1.3 Ripples and Buckling

As stated in previous sections, ripples are ubiquitous in suspended graphene monolayers. Their cause is not yet completely clear but there are experimental evidences of nanometric [99] and atomic size [97, 141] rippling. As we discussed in section 1.1.2, a completely flat crystalline membrane would be thermodinamically unstable, which makes rippling a possible explanation of how graphene avoids this instability. In other words, it is a $2D$ material embedded in a $3D$ space, see figure 1.5. Ripples in graphene may stem from the coupling between carrier density fluctuations and membrane deformations. Electron-holes puddles of nanometric size have also been observed, which could support this theory, [98]. .

A relation between charge carriers and deformations in graphene is even more clear after studying buckling experiments of suspended graphene with scanning tunneling microscopy (STM) techniques. In these experiments, a nanometric tip (ideally its sharp end would be an atom) is placed very close to the sample, but not touching it. A voltage bias between the tip and the sample induces a tunneling current, which greatly depends on their distance,

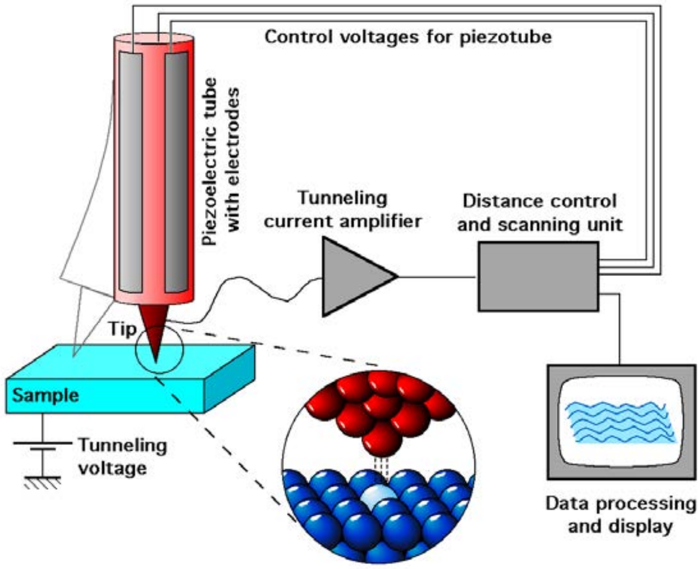

Figure 1.6: Simplified picture of the Scanning Tunneling Microscopy (STM) process. A tunneling current flows between the sample and the tip, it is extremely dependent on the sample-tip distance, giving a high sensitivity to the process. Different operational modes are possible, most common ones maintain a constant voltage bias while measuring the height or the current (leaving the other one constant too). Figure author: Michael Schmid, TU Wien.

see figure 1.6.

To study buckling of graphene monolayers, one proceeds as follows the process is the following: The tip is at a fixed x-y position over the suspended graphene sheet. The current between tip and sample is kept constant, whereas voltage is swept. To achieve these conditions, the microscope adjust its height so that the current is kept constant, [102, 130].

For suspended graphene sheets, the sample is not rigid and "follows" the movement of the microscope tip when it tries to adjust its height to maintain the current constant. In figure 1.7, the grid used as substrate for the graphene sheet, a simplified drawing of the process, and the experimental results are showed. If the current is below a certain critical value, which for this configuration is around 1 nA, suspended graphene will bend following the tip as voltage is increased and it will reversibly come back to its original position when voltage is decreased, without buckling, see figure 1.7 reprinted from [144]. However, once the current surpasses the critical value permanent buckling occurs, depicted in figure 1.8.

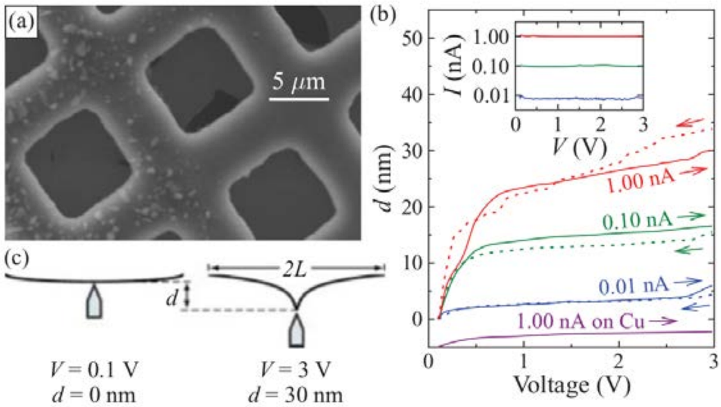

Figure 1.7: Figures showing reversible bending of graphene sheets controlled by a STM operating at constant current mode. (a) SEM image of 2000-mesh copper grid with transferred graphene. (b) Constant-current scanning tunneling spectroscopy (CC-STS) data showing the vertical movement (d) of the STM tip vs applied bias voltage for three different set-point currents. The bottom trace is graphene on copper data that has been offset for clarity. The inset shows the measured current as a function of applied bias voltage. (c) Schematic of the large-scale location of the STM tip below the freestanding graphene membrane with a low (left) and a high voltage (right). Reprinted from [144].

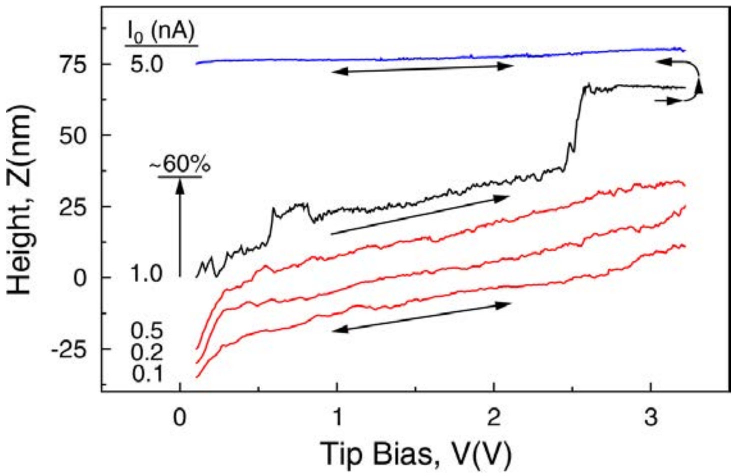

Figure 1.8: Figure showing permanent buckling of a graphene suspended sheet induced by STM. The experimental procedure is analogous to the one described in figure 1.7. In this case, red curves indicate the flexible state which is reversible (similar to the ones shown in figure 1.7). For working intensity equal or bigger than 1 nA, a permanent jump occurred, as shown by the black curve. Once the system is permanently buckled, the blue curve indicates its irreversibility. Curves are slightly offset from each other for clarity. Reprinted from [130].

Finally, recent experiments on suspended graphene using scanning tunneling microscopy working at constant-current mode, show how increasing the current between the tip and the sample induces a tunable rippling on the membrane, [63]. The used currents are in the pA range, three orders of magnitude smaller than the ones used in [102, 130]. The ripples length scale is reduced when increasing the tunneling current. Even if a clear explanation to this effect is not available at the moment, it seems clear that strengthens the idea of a coupling between charge density fluctuations and corrugations in graphene.

1.2 Dynamics and chaos in semiconductor superlattices

1.2.1 Weakly coupled semiconductor superlattices

A semiconductor superlattice (SL) is a periodic succession of different layers of semiconductor materials, whose conduction bands form an alternation of potential wells and barriers. In the most simple case, which is studied in this dissertation, only two different semiconductor materials are used.

Semiconductor superlattices can be roughly separated in two groups: Weakly and strongly coupled. This distinction is based on the barrier width. It is a weakly coupled SL when this width is much larger than the typical electron wavelength inside the barrier and a description of the electronic properties can be based on the subband structure of the corresponding isolated quantum wells together with resonant tunnelling across the barrier of two adjacent wells, see figure 1.9. In contrast, strongly coupled SLs contain thin barriers between wells so that the electronic properties should be described in terms of extended states such as Bloch functions, see [27].

Doped electrons inside these heterostructures will be immerse in the conduction band of both semiconductor materials. However, the difference in the bottom of this band produces the effective wells and barriers already discussed, translating in new subbands due to the confinement inside the potential wells. Typically, electrons will decay to the bottom subband at every well at a much faster rate than tunneling process occurs. Figure 1.9 shows how *resonant* tunneling between subbands can involve two bottom subbands at both sides of the barrier or transport from the first to the second subband and subsequent decay to the bottom one; these two situations promote a low and high electric field domain. Charge is accumulated in the transition between these two domains, corresponding with the change in electric field

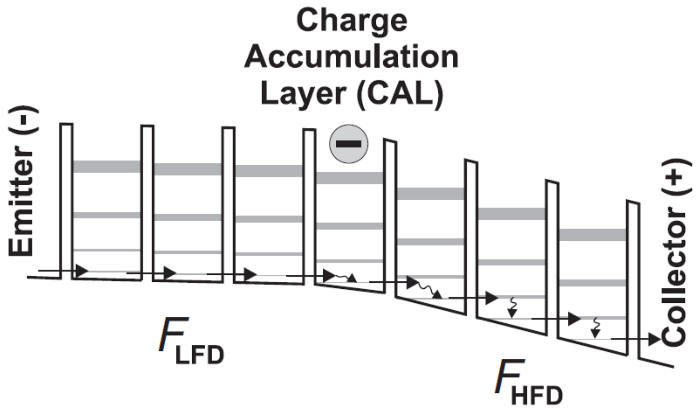

Figure 1.9: Simplified plot of a weakly coupled SL. Potential wells and barriers are depicted, arrows stand for resonant tunneling processes and grey regions represent subbands (due to quantization coming from the potential confinement) with scattering broadening. Low and high electric field (F) domains are also shown. Reprinted from [27].

magnitude.

In experimental measurements, the SL will be subject to a external voltage (DC or AC). This voltage works as an external constraint to the SL, equal to the total potential drop along the SL at every moment. However, even for a constant external voltage, there are infinitely many potential "shapes" (electric field distributions) that fulfill this condition. This situation translates to the fact that for constant external voltages there will be regimes of stationary potential distributions or regimes where periodic, quasi-periodic or even chaotic oscillations can be found.

Most common weakly coupled semiconductor superlattices were built using GaAs for wells and AlAs for barriers. However, they had to operate at low temperatures since electrons would leak through barriers using the X valley of AlAs, see figures 1.10 and 1.11.. Recent studies proposed to move from AlAs to $Al_{0.45}Ga_{0.55}As$ for the barriers, avoiding thermal carrier leakage through the X valley and enabling the use of weakly coupled semiconductor superlattices at room temperature, [75]. This experimental work found spontaneous chaotic current oscillations even at room temperature, the frequency spectrum of which was ranged from DC to 4 GHz, which can be used as ultra-wide-band noise sources with a bandwidth of several GHz. The theoretical study of this behavior is addressed in the second part of this dissertation.

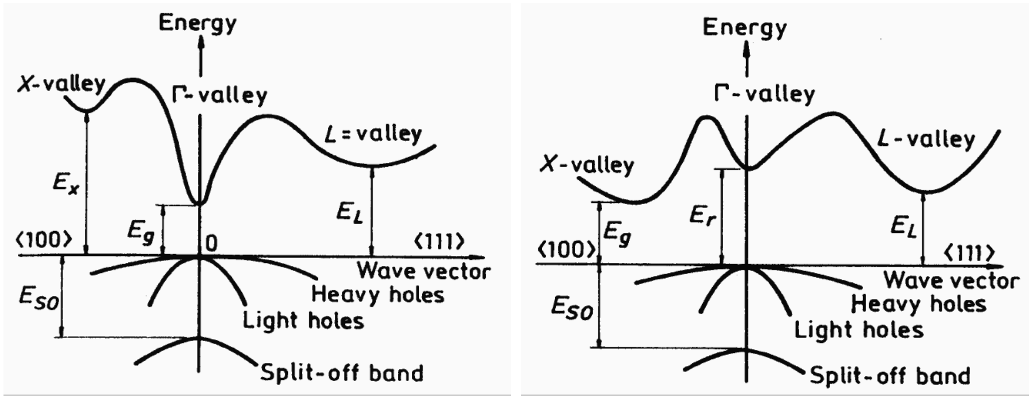

Figure 1.10: Band structure of $Al_xGa_{1-x}As$ for $x < 0.45$ (left panel) and $x > 0.45$ (right panel). Note how the X valley is above the Γ valley for $x < 0.45$ and below for $x > 0.45$. Reprinted from [1].

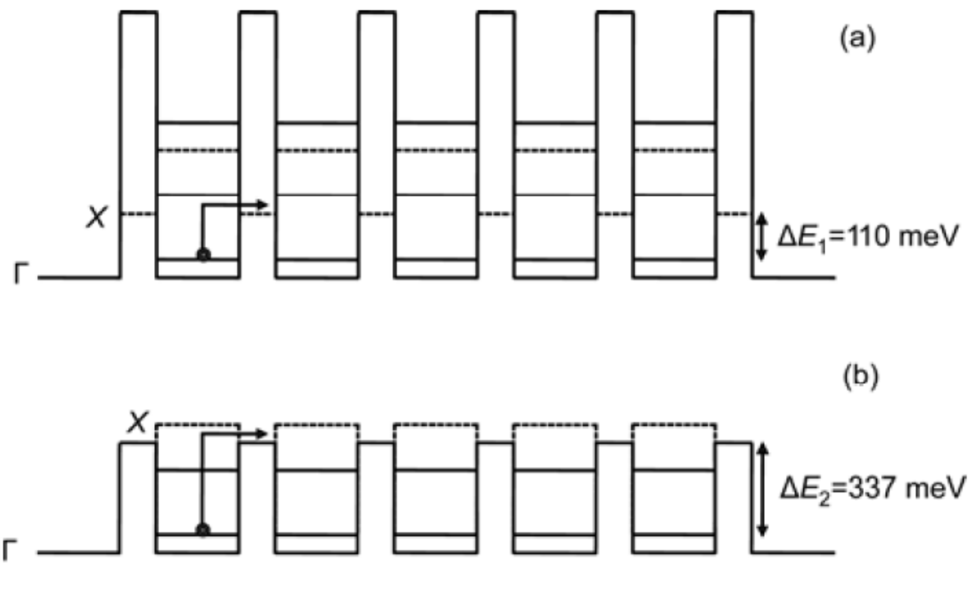

Figure 1.11: Magnitude of potential wells and barriers for AsAs/AlAs (a) and $AsAs/Al_{0.45}Ga_{0.55}As$ (b). Subbands are also depicted, arrows stand for thermal carrier leakage through X valley, which is less probable in the (b) case, enabling the use of weakly coupled SL at room temperature. Reprinted from [75].

1.2.2 Random number generation

Security of current technology and telecommunications dramatically depends on the generation of random numbers. Online gambling, computer telecommunications, finance and online commerce, to mention some, use these random numbers in their encryption systems. Usually, one actually uses pseudorandom numbers, which are generated by numerical algorithms that produce seemingly unpredictable number sequences given an initial seed. This approach is cheap and fast, and it can also be useful when doing stochastic modelling or Monte Carlo simulations, since reproducibility is a desired feature.

To avoid vulnerability of secure communications or online commerce, new sources of real random numbers are highly sought. Physical processes where deterministic chaos or quantum uncertainty are present are possible candidates, and the generation rate will be the determinant factor to enable their use as true random numbers generators (TRNG). To name two examples, TRNs are currently generated using atmospheric noise [2], or detection of photons by photodiodes [45]. In the latter case, rates of random bit generation up to 4.01 Mbit/s were reached without any postprocessing procedure.

TRN generation rates were highly increased by the appearance of chaotic semiconductor lasers [137]. However, their complex optical and electronic components, depicted in figure 1.12, require specific conditions and make it difficult their scalability and reduction of production costs. On the other hand, semiconductor superlattices are all electronic submicron devices that could be integrated in more complex circuits. They have reliably produced truly random sequences of numbers at fast rates in laboratory experiments, [92]. If they show to be scalable, these devices could generate fast and cheaply large quantities of random numbers.

1.2.3 Some tools to study chaotic systems

From the broad field of dynamics, where systems that evolve in time are studied, we will pick some tools that enable us to better understand and characterize the chaotic behavior of semiconductor superlattices. In a few words, a deterministic system is chaotic when it exhibits aperiodic behavior that depends sensitively on the initial conditions. In that case, long-term predictions become impossible due to the unavoidable uncertainty on measurements.

A systematic approach to chaos is out of the scope of this introduction, and only some concepts, useful for the next chapters, are covered. Introductory texts to the topic are [87, 135], whereas specific techniques applied to

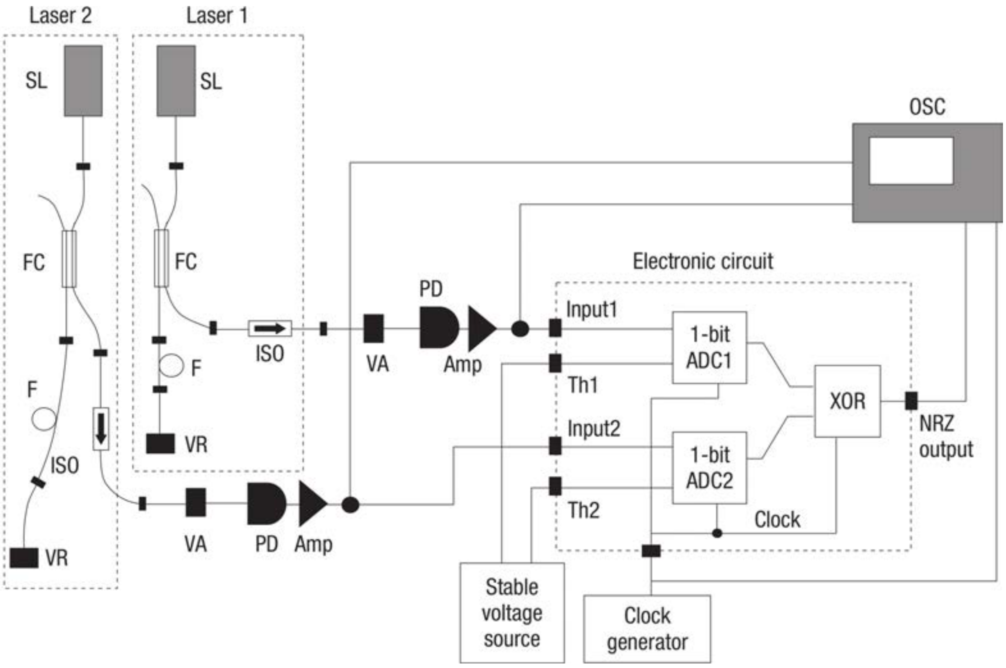

Figure 1.12: Experimental setup of random bit sequence generator using two chaotic lasers. The intensity of the laser light output is converted to an electrical signal by a photodetector (12 GHz bandwidth) with a.c. coupling to remove the d.c. component. The signal is then amplified by an electronic amplifier (18 dB gain, 20 GHz bandwidth) and then converted to a binary digital signal. Amp, electronic amplifier; F, optical fibre; FC, fibre coupler; ISO, fibre isolator; OSC, digital oscilloscope; PD, photodetector; SL, semiconductor laser; Th1,2, threshold voltages; VA, variable fibre attenuator; VR, variable fibre reflector; XOR, exclusive OR. Reprinted from [137].

the study of charge transport can be found in [31].

Semiconductor superlattices can be modelled as a set of coupled differential equations where quantum uncertainty (at the tunneling process, scattering, etc.) can be included through some noise terms. The phase space comprises all the variables defining the system configuration at time t whereas the one-dimensional curve representing the solution of the system equations in the phase space is called a trajectory.

The high number of dimensions of phase space makes it impossible to visualize. However, projections of this space, called phase portraits, enable us to represent part of the behavior of the system and to characterize its main features.

Depending on a control parameter, the trajectory of the system in the phase space may move from a fixed point (stationary solution) to a periodic or quasi-periodic orbit up to a chaotic behavior. To condense all this information in one plot, it is useful to turn to Poincaré sections. Using the intersections of the system trajectory with a chosen hyper-surface, the dynamical behavior can be characterized, see figure 1.13.

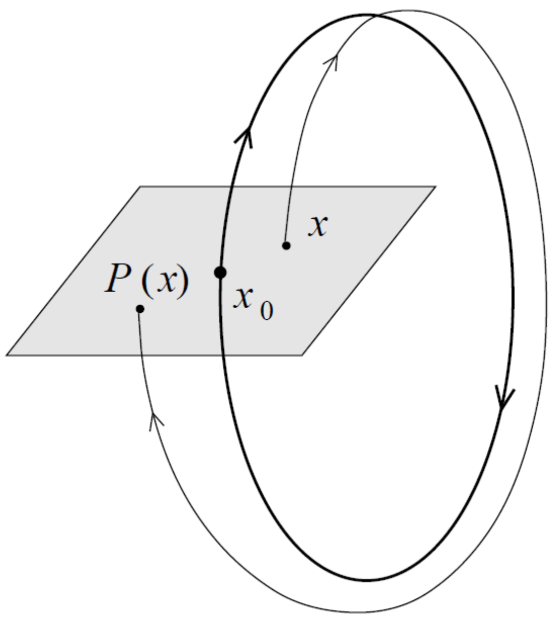

Figure 1.13: Simplified image of a Poincaré map. For the cycle represented with the darker line, x_0 maps onto itself. Reproduced from [87].

In the case that a 2D phase portrait is taken, the corresponding Poincaré section is 1D, and it can be plotted versus the controlled parameter. This bifurcation diagram can be very useful to visualize different dynamical behaviors depending on the controlled parameter value. Different bifurcations can be observed using bifurcation diagrams. One well known route to chaos is the period doubling cascade. It is characterized by doubling the number of points in the Poincaré section at every bifurcation. The controlled parameter values where these bifurcations happen follow the property,

$$\frac{\mu_i - mu_{i-1}}{\mu_{i+1} - \mu_i} \rightarrow 4.6692016\ldots \tag{1.3}$$

bifurcations are more and more close until the system reaches a chaotic state, [53, 54].

Part I

Statistical approaches to mechanics of graphene

Motivation

The discovery of graphene has spawned one of the most fertile scientific fields of today. Its unique electrical and mechanical properties [89, 105, 108, 109] promise to revolutionize current technology, which makes it important to characterize the properties of graphene in order to design and optimize new devices. Among its mechanical properties, the presence of ripples in suspended graphene [12, 99], which modify the electronic band structure [69] and are expected to be relevant in the understanding of electronic transport [81], has triggered a great theoretical effort. Different works have focused on their explanation from either first principles [3, 30, 50, 60, 66, 70, 83, 127] or by using simple statistical mechanics models [22, 23, 25, 123, 130].

Thermal and external stresses have been used to create large ripples (wrinkles) in a layer of graphene which is suspended over trenches [13]. These ripples have been explained using classical elasticity [13] and seem to be qualitatively different from the nanometer sized ripples observed in [84, 94, 99], which tend to be considered inherent to suspended graphene. Even when ripples in graphene are not fully understood, one of the most promising approaches to ripple formation is the quantum mechanical study of the membrane and the phonon-electron interaction as a mechanism for rippling [60, 127]. Since the graphene Debye temperature is $T_D \sim 1000$ K, the quantum treatment of graphene seems justified at room temperature. Perturbation treatments point to the vanishing of the renormalized bending energy of the membrane as a possible mechanism for ripple formation [66, 127]. The destabilizing effects of quantum fluctuations on the bending rigidity of crystalline membranes (without electron-phonon interaction) have been considered in [80]. Within equilibrium theory and without phonon-electron interaction, the effect of (Matsubara) frequency-dependent renormalization of the anharmonic coupling after elimination of in-plane phonons has been considered in [9].

Recent experimental works emphasize buckling in suspended graphene monolayers, as buckling is more easily characterized than ripple formation and can strongly affect the design of new graphene-based devices. Long-range buckling of the graphene sheet is pronounced near defects and dislocations [24, 40, 86, 90, 120, 132]. In [93], buckled bilayer and monolayer graphene are fully clamped to circular holes in an electrode. Buckling is induced by the fabrication process so that the sheets are buckled at zero applied electric field. In the experiment, an external electric field pressures the membrane and induces a sudden change in the buckling direction (a “snap-through” effect). A relation between the critical pressure and the bending rigidity of bilayer graphene provides a measure of the latter. Even when the graphene layer is not buckled initially, a strong enough electrostatic force can produce irreversible buckling [136]. A spontaneous buckling effect ("mirror buckling") is also found by Xu *et al.* in [143]. This effect is systematically studied in [130], in a complementary approach to that in [93]. In [130], the authors study a suspended graphene monolayer using scanning tunnelling microscopy (STM). The microscope tip is located on the centre of an initially non-buckled layer. The STM keeps a constant current and a variable potential between the tip and the sample. Once the current is fixed at a sufficiently high value, the sample buckles when the potential increases, similarly to the experiments in [93, 136]. Molecular Dynamics (MD) simulations have also been carried out and compared with experiments in [4, 102]

These experimental efforts have their theoretical counterpart through different approaches to the buckling of two dimensional (2D) layers such as graphene. A broad overview of the effects of strain in graphene and its relation with its electrical properties can be found in [8]. Moreover, the study of spontaneous buckling in graphene due to doping is carried out in [60]. Finally, in polymerized membranes, buckling occurs below a critical temperature [71].

Chapter 2

Bifurcation analysis and phase diagram of a spin-string model with buckled states

2.1 Introduction

Simple models are often used in statistical physics as a first step for describing complex behaviours, because their simplicity helps us identify the main mechanisms underlying the observed phenomenology. One prototypical example is the Ising model, which has been used in many different contexts. In the realm of equilibrium statistical physics, a milestone is Onsager's work on its phase transition in the $2d$ case [111], which triggered an extensive body of work in critical phenomena [88, 145]. Within non-equilibrium statistical mechanics, Glauber's work on the approach of the Ising model to equilibrium was a crucial contribution to its early development [64]. More recently, the Ising model has been also used to describe glassy behaviour, such as non-exponential relaxation [33, 133], residual properties in cooling processes [34, 85], aging [32, 114, 117] or the so-called Kovacs hump [14, 15, 35, 65, 115, 125].

Mechanical systems coupled to spins have been used to describe structural phase transitions [29, 52, 77, 112, 113, 115, 118, 119, 129]. In most cases, the effective system obtained after integrating the mechanical variables has been investigated. Therein, the phase transition is often associated to the emergence of a long-ranged interaction among the spins, which makes the magnetisation be non-zero below a critical temperature. Very recently, rippling and buckling in graphene [22, 23, 30, 50, 60, 66, 127, 130] has been addressed by using simple spin-string (in $1d$) [25] or spin-membrane (in $2d$) [23, 123, 124] models. These models comprise elastic degrees of freedom on a lattice, modelled by coupled harmonic oscillators, which interact with some internal degrees of freedom, modelled by pseudo-spins. Therein, the complementary approach has been considered: the integration over the pseudo-spin variables leads to an effective free energy for the elastic system, in which its curvature is controlled by the local magnetisation. Then, buckled profiles are associated to pseudo-spins configurations with, at least partial, ferromagnetic order.

In the spin-string or the spin-membrane models, the perpendicular to the lattice displacement is modelled by a continuous variable u_i, which is connected to its nearest neighbours by harmonic springs and is also linearly coupled to the pseudo-spin at the same site σ_i. To be concrete, we are using the notation for the $1d$ case, in the $2d$ system (u_i, σ_i) must be replaced by (u_{ij}, σ_{ij}). As shown in [25], this coupling brings about a second-order transition from the flat configuration to a buckled state below a certain critical temperature. The curvature of this buckled state is controlled by the pseudo-spin local magnetisation; the flat-to-buckled transition in the string or membrane is associated to a paramagnetic-to-ferromagnetic transition for the pseudo-spins. Moreover, if short-ranged antiferromagnetic interactions between the pseudo-spins are added [123, 124], the competition between these interactions make it appear different phases and transitions between them, depending on the values of the parameters characterising the interactions. The simplicity of the model makes it possible to determine the role played by the different interactions in the emergence of the different phases.

In this chapter, we take advantage of the simplicity of the $1d$ spin-string model to build its phase diagram as a function of the temperature θ and the parameter characterising the strength of the antiferromagnetic interaction κ. Specifically, we are able to derive analytically the bifurcation line from which the stable buckled solution stem continuously at high enough temperatures and also the lines characterising the first-order transition that appears in the model for lower temperatures. This change in the order of the transition takes place at a certain point (κ_c, θ_c) in the (κ, θ) plane, which is a tricritical point [68, 88]. This is crucial: what makes it possible metastability for low enough temperatures is the emergence of a first-order transition. Interestingly, we show that the physical picture that emanates from this phase diagram is completely compatible with the one obtained in the $2d$ spin-membrane model and improves our understanding of the behaviour observed there, which was obtained numerically. In particular, the STM-like transition upon a quasistatic increase of the temperature can be understood as the system crossing the bifurcation line, below which the flat string is metastable but above which the only stable solution is buckled.

The chapter is organised as follows. In Sec. 2.2, we define the model and introduce the free energy density controlling its equilibrium behaviour, together with the corresponding Euler-Lagrange equation governing the equilibrium profiles. Section 2.3 is devoted to the study of some exact solutions of the Euler-Lagrange equation, specifically the flat profile for all temperatures and the linear-parabolic profiles appearing in the low temperature limit. We analyse the bifurcation from the flat solution in Sec. 2.4 and the emergence of a (tri)critical point, at which the transition changes from second-order to first-order. Also, the stability of the different phases is investigated, including the possible existence of metastable states. The phase diagram of the system is thoroughly discussed in Sec. 2.5, using both the analytical results in the previous sections and numerical results. We present the main conclusions of our work in Sec. 2.6. The appendices deal with some technical details and calculations that are omitted in the main text.

2.2 Free energy density of the string. Euler-Lagrange equation for the profiles

Our starting point is the recently proposed $1d$ lattice model in Refs. [25, 123]. The elastic degrees of freedom are modelled by purely transversal displacements u_j at each lattice site j, $j = 1, \ldots, N$, and the rest of the "internal" degrees of freedom at each site are included in Ising pseudo-spin variables $\sigma_j = \pm 1$. The Hamiltonian of the system is

$$\mathcal{H}(\boldsymbol{u}, \boldsymbol{p}, \boldsymbol{\sigma}) = \sum_{j=0}^{N} \left[\frac{p_j^2}{2m} + \frac{k}{2}(u_{j+1} - u_j)^2 - f u_j \sigma_j + J \sigma_{j+1} \sigma_j \right], \tag{2.1}$$

where p_j stands for u_j's conjugate momentum. Therefore, we have (i) a nearest-neighbour harmonic interaction between the elastic variables, $k(u_{j+1} - u_j)^2$, (ii) an on-site interaction between the elastic and the internal variables, $-f u_j \sigma_j$, which can be understood to arise from the internal forces that push each atom along the vertical direction, and (iii) a nearest-neighbour interaction between the internal degrees of freedom, $J \sigma_{j+1} \sigma_j$. The boundary conditions correspond to a clamped situation, $u_0 = p_0 = \sigma_0 = u_{N+1} = p_{N+1} = \sigma_{N+1} = 0$.

This simple mesoscopic model allows us to compute the out-of-equilibrium evolution of the system, which could be much more complicated for first-principles approaches. The dynamics of the model is as follows: (i) the oscillators' equations of motion,

$$m\,\ddot{u}_j - k\,(u_{j+1} + u_{j-1} - 2u_j) = f\sigma_j, \tag{2.2}$$

are the usual ones, whereas the spins evolve according to Glauber dynamics [64]. The transition rate from the configuration $(\boldsymbol{u}, \boldsymbol{p}, \boldsymbol{\sigma})$ to $(\boldsymbol{u}, \boldsymbol{p}, R_j\boldsymbol{\sigma})$ (obtained from $\boldsymbol{\sigma}$ by flipping the j-th spin) is

$$W_j(\boldsymbol{\sigma}|\boldsymbol{u}, \boldsymbol{p}) = \frac{\alpha}{2}(1 - \beta_j\sigma_j), \tag{2.3}$$

$$\beta_j = \tanh\left[\frac{f}{T}u_j - \frac{J}{T}(\sigma_{j-1} + \sigma_{j+1})\right], \tag{2.4}$$

in which α is the characteristic attempt rate for the spin flips. The Glauber transition rates ensure that the system satisfies detailed balance, and therefore the system reaches equilibrium for long enough times. In equilibrium, the probability of a certain configuration $(\boldsymbol{u}, \boldsymbol{p}, \boldsymbol{\sigma})$ is proportional to $e^{-\mathcal{H}/T}/Z$, where we measure the temperature T in units of energy.

As explained in [25], for $J = 0$ rippling appears provided the temperature is less than

$$T_0 = \frac{f^2 K_N^2}{k}, \quad K_N \sim \frac{N}{\pi}, \tag{2.5}$$

as $N \to \infty$. To guarantee that the diffusive term in (2.2) remains finite in the continuum limit, it is convenient to nondimensionalize the equations of motion as follows:

$$u_j^* = \frac{ku_j}{fK_N^2}, \quad t^* = \frac{t}{K_N}\sqrt{\frac{k}{m}}, \tag{2.6}$$

$$\kappa = \frac{J}{T_0}, \quad \delta = \frac{\alpha K_N\sqrt{m}}{\sqrt{k}}, \quad \theta = \frac{T}{T_0} = T\frac{k}{f^2K_N^2}. \tag{2.7}$$

Then the transition rates and the equations of motion become

$$W_j^*(\boldsymbol{\sigma}|\boldsymbol{u}^*, \boldsymbol{p}) = \frac{\delta}{2}(1 - \beta_j\sigma_j),$$
$$\beta_j = \tanh\left[\frac{u_j^*}{\theta} - \frac{\kappa}{\theta}(\sigma_{j-1} + \sigma_{j+1})\right],$$
$$\frac{d^2u_j^*}{dt^{*\,2}} - K_N^2(u_{j+1}^* + u_{j-1}^* - 2u_j^*) = \sigma_j. \tag{2.8}$$

We will omit the asterisks in nondimensional equations from now on. In order to obtain the scaling of the critical temperature, we need to know the scaling of the model parameters with the system size. In principle, this could be done by deriving our model from a fundamental microscopic one, but this is outside the scope of this paper. Nevertheless, we discuss some possible scalings in the following. If both the elastic constant k and the antiferromagnetic coupling constant J are considered to be independent of the system size, the only remaining parameter is f, the coupling between the elastic and internal (spin) degrees of freedom. If f is also independent of the system size, the critical temperature T_0 diverges as N^2. In this case, rippling would be observed at all temperatures. On the other hand, a finite value of T_0 in the large system size limit is obtained when $f \propto N^{-1}$. Then, rippling would be observed only for $T < T_0$. In principle, both situations are compatible with current experiments, in which rippling is observed over a wide temperature range.

Let us consider now the equilibrium situation. Equation (2.8) can be averaged, with the result

$$\frac{1}{\pi^2}\frac{d^2}{dx^2}\langle u\rangle = -\langle\sigma\rangle, \tag{2.9}$$

in which $\langle u\rangle$ and $\langle\sigma\rangle$ are the equilibrium average height and spin at position $x = i/N$; the system has unit size in the continuous space variable $x = i/N$, $0 \le x \le 1$. Therefore, the average curvature of the ripples is directly linked to the average spin. This idea has been used to develop a phenomenological Ising model to study rippling in graphene in scanning tunneling microscopy experiments, in which each spin represents a whole ripple and the spin sign gives its corresponding convexity [130].

We can derive an effective free energy for the string, by integrating the canonical distribution over the momenta $\boldsymbol{p}$ and the spins $\boldsymbol{\sigma}$: the resulting probability $\mathcal{P}$ becomes a functional of the string profile $u(x)$, which in dimensionless variables reads,

$$\mathcal{P}[u] \propto \exp\left(-\frac{\mathcal{F}}{\theta}\right), \quad \mathcal{F}[u] = N\int_0^1 dx\, \underbrace{\left[\frac{1}{2\pi^2}\left(\frac{\partial u}{\partial x}\right)^2 - \theta\ln\zeta\left(\frac{u}{\theta},\frac{\kappa}{\theta}\right)\right]}_{f(u,\frac{du}{dx})}, \tag{2.10a}$$

$$\zeta\left(\frac{u}{\theta},\frac{\kappa}{\theta}\right) = \exp\left(-\frac{\kappa}{\theta}\right)\cosh\left(\frac{u}{\theta}\right) + \exp\left(\frac{\kappa}{\theta}\right)\sqrt{1+\exp\left(-\frac{4\kappa}{\theta}\right)\sinh^2\left(\frac{u}{\theta}\right)}. \tag{2.10b}$$

The quantity $\ln\zeta$ is the logarithm of the spins partition function per site, which depends on the "field" $fu_j/T \to u/\theta$ and the coupling $J/T \to \kappa/\theta$.

The particularization of this free energy to the $J = 0$ case was obtained in Ref. [25]. For $J \neq 0$, in order to calculate $\ln \zeta$, the system is divided into a set of nearly independent subsystems with $N_s \gg 1$ sites each, but such that $N_s \ll N$ and the "field" u can be considered almost constant within each subsystem. Therefore, we can use the partition function for Ising spins under a constant external field, equation 2.10b [55].

For the considered values of the parameters (θ, κ), $F[u; \theta, \kappa]$ is the total free energy corresponding to the string profile $u(x)$, $f(u, u'; \theta, \kappa)$ is the (local) free energy density per unit length, and $\ln \zeta(u; \theta, \kappa)$ is the logarithm of the pseudo-spins partition function per site.

2.2.1 Euler-Lagrange equation for the equilibrium profiles

The equilibrium profiles $u_{\text{eq}}(x)$ are those which minimise the free energy functional $F[u; \theta, \kappa]$, with clamped boundary conditions, i.e. $u(0) = u(1) = 0$. They solve the Euler-Lagrange equation, that is,

$$\frac{1}{\pi^2} u''_{\text{eq}} = -\mu(u_{\text{eq}}; \theta, \kappa), \qquad u_{\text{eq}}(0) = u_{\text{eq}}(1) = 0, \tag{2.11}$$

in which

$$\mu(u; \theta; \kappa) \equiv -\frac{\partial f(u; \theta, \kappa)}{\partial u} = \frac{e^{-\frac{2\kappa}{\theta}} \sinh\left(\frac{u}{\theta}\right)}{\sqrt{e^{-\frac{4\kappa}{\theta}} \sinh^2\left(\frac{u}{\theta}\right) + 1}}, \tag{2.12}$$

is the local value of the magnetisation. Therefore, it is the local value of the pseudo-spin variable (magnetisation) that the local value of the string curvature stems from. We can introduce an order parameter to discriminate non-flat from flat profiles, specifically

$$M(\theta; \kappa) = \left| \int_0^1 dx\, \mu(u_{\text{eq}}; \theta, \kappa) \right|, \tag{2.13}$$

which is the absolute value of the total magnetisation in the system We focus on the simplest non-flat solutions with no internal nodes, so that M cannot be zero for non-flat states. Further information is given by the parameter

$$\mathcal{DL}(\theta; \kappa) = \frac{1}{2} \left(1 - \theta \int_0^1 dx\, \left. \frac{\partial \ln \zeta}{\partial \kappa} \right|_{u=u_{\text{eq}}} \right), \tag{2.14}$$

more specifically about the antiferromagnetic ordering of the pseudo-spins: the nearest-neighbour pseudo-spin correlations is given by $C = -\theta\, \partial_\kappa \ln \zeta$

[123]. Then, for perfect antiferromagnetic ordering we have $\mathcal{DL} = 0$, $\mathcal{DL} = 1/2$ for random pseudo-spins and $\mathcal{DL} = 1$ for perfect ferromagnetic ordering.

The set of sufficient conditions for the free energy functional $F[u]$ to have a relative (or weak) minimum for the curve $u = u_{\text{eq}}(x)$ is:

1. the curve $u_{\text{eq}}(x)$ must satisfy the Euler-Lagrange equation (2.11).
2. If we linearise the Euler-Lagrange equation around $u_{\text{eq}}(x)$, i.e. we write $u(x) = u_{\text{eq}}(x) + \delta u(x)$ and retain only linear terms in $\delta u(x)$, the linearised equation
$$\delta u'' = -\pi^2 \left(\frac{\partial \mu}{\partial u}\right)_{u=u_{\text{eq}}} \delta u, \quad \delta u(0) = \delta u(a) = 0, \tag{2.15}$$
must have only the trivial solution $\delta u(x) \equiv 0$, $\forall x$, for any $a \leq 1$.

Note that the two conditions above, considered separately, are both necessary conditions for having a weak minimum (with the nuance $a < 1$ instead of $a \leq 1$ in the second one) [62].

2.3 Some exact solutions of the Euler-Lagrange equation

2.3.1 The flat profile

The flat profile $u_{\text{L}}(x) \equiv 0$, $\forall x$, is always a solution of the Euler-Lagrange equation, which we call phase L [1]. Moreover, it is a (locally) stable equilibrium profile if it corresponds to a minimum of the free energy functional. Therefore, we consider the particularisation of Eq. (2.15) for deviations from the flat string, i.e.
$$\delta u'' = -\pi^2 \theta^{-1} \exp(-2\kappa/\theta)\, \delta u, \qquad u(0) = u(a) = 0, \tag{2.16}$$
for any $a \leq 1$. Aside from the trivial solution $\delta u(x) \equiv 0$, we may have solutions of the type
$$\delta u(x) = A \sin\left[\pi \theta^{-1/2} \exp(-\kappa/\theta) x\right], \tag{2.17}$$
where A is an arbitrary constant, provided that one can choose a such that
$$\theta^{-1/2} \exp(-\kappa/\theta) a = n, \qquad n \in \mathbb{N},\ a \leq 1. \tag{2.18}$$

[1]We use L (from level) instead of F, in order to avoid confusion in sentences such as "the free energy F of the phase F"

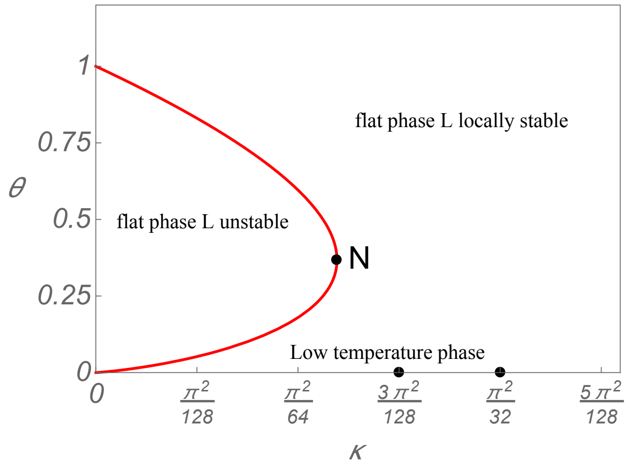

Figure 2.1: Bifurcation line in the (κ, θ) plane. The point N at the nose of the bifurcation curve, with coordinates $(\kappa_{\rm n}, \theta_{\rm n})$, is explicitly marked. The flat solution is locally stable (the free energy functional has a relative minimum) outside the bifurcation line, whereas it becomes unstable (the free energy is no longer a minimum) inside. In addition, the values of κ controlling the low temperature behaviour, $\kappa_t^{(0)} = 3\pi^2/128$ and $\kappa_M^{(0)} = \pi^2/32$, are shown with points.

The above analysis shows, on the one hand, that the flat solution gives a relative minimum of the free energy in the region of the (κ, θ) plane defined by the inequality $\theta^{-1/2}\exp(-\kappa/\theta) < 1$, where the only solution of Eq. (2.16) is the trivial one. On the other hand, in the region $\theta^{-1/2}\exp(-\kappa/\theta) > 1$, the flat profile ceases to be stable: we have at least a non-trivial solution of Eq. (2.16) by choosing $a = \theta^{1/2}\exp(\kappa/\theta) < 1$. Thus, the necessary conditions for $F[u]$ to have a minimum for the flat solution do not hold any more.

The picture described in the above paragraph means that the curve $\theta^{1/2}\exp(\kappa/\theta) = 1$ is a bifurcation line in the (κ, θ) plane, at which other non-flat possible equilibrium profiles may bifurcate. We plot this bifurcation line in Fig. 2.1. We use the notation κ_b and θ_b to mark that a point (κ_b, θ_b) belongs to the bifurcation line, i.e.

$$\theta_b \exp(2\kappa_b/\theta_b) = 1, \;\; \text{or} \;\; \kappa_b = -\frac{1}{2}\theta_b \ln \theta_b. \tag{2.19}$$

The "nose" of the bifurcation line corresponds to the maximum of κ_b as a function of θ_b, i.e. to the point $N \equiv (\kappa_{\rm n} = (2e)^{-1}, \theta_{\rm n} = e^{-1})$. For $\kappa > \kappa_{\rm n}$, the flat solution always gives a local minimum of the free energy, regardless of the temperature value. For $\kappa < \kappa_{\rm n}$, there are two temperature regions inside which the flat solution is locally stable: for high enough temperatures $\theta > \theta_1(\kappa)$ and for low enough temperatures $\theta < \theta_2(\kappa)$, see Fig. 2.1. Note that $\theta_1 > 2\kappa$ whereas $\theta_2 < 2\kappa$ ($\theta_\mathrm{n} = 2\kappa_\mathrm{n}$). The tangent to the bifurcation line at each point (κ_b, θ_b) can be written as

$$2\,\delta\kappa_b + (1 + \ln\theta_b)\delta\theta_b = 0, \tag{2.20}$$

in which $\delta\theta_b$ and $\delta\kappa_b$ are the (small) deviations from (κ_b, θ_b) over the tangent.

2.3.2 Low temperature profiles

The flat profile is the only possible solution of the Euler-Lagrange equation and it is stable for very high temperatures, for which $\theta \gg |u|$ and its linearisation around $u = 0$ stems naturally. Moreover, at very low temperatures, the flat solution is also (locally) stable, since it corresponds to a minimum of the free energy because $\exp(-2\kappa/\theta)/\theta < 1$, see Fig. 2.1. Interestingly, other non-flat solutions of the Euler-Lagrange equation can also be exactly found in the low temperature region.

For $\theta \ll |u|$, the local magnetisation μ (2.12) reduces to

$$\mu(u; \kappa, \theta = 0^+) = \mathrm{sgn}(u)\eta(|u| - 2\kappa), \tag{2.21}$$

where $\eta(x)$ is the Heaviside step function. Substitution of Eq. (2.21) into the Euler-Lagrange equation (2.11) shows that those regions with $|u| < u_0 = 2\kappa$ have a linear profile, $u'' = 0$, whereas those with $|u| > 2\kappa$ have a parabolic shape, $u'' = \pm\pi^2$. For the sake of simplicity, we restrict ourselves to profiles with only one maximum and no internal nodes. Due to the clamped boundary conditions, the linear profile is found close to the boundaries, $x \in (0, x_0)$ or $x \in (1-x_0, 1)$, and the parabolic profile is observed in the bulk of the system, $x \in (x_0, 1 - x_0)$. Continuity of both u and u' determines x_0, $\pi^2 x_0(1 - 2x_0) = 2u_0$. If $\kappa < \kappa_M^{(0)} = \pi^2/32$, there are two solutions $x_{0,1}$ and $x_{0,2}$,

$$x_{0,1} = \frac{1}{4}\left(1 - \sqrt{1 - \frac{\kappa}{\kappa_M^{(0)}}}\right), \; x_{0,2} = \frac{1}{4}\left(1 + \sqrt{1 - \frac{\kappa}{\kappa_M^{(0)}}}\right), \tag{2.22}$$

such that $x_{0,1} < 1/4$, $x_{0,2} > 1/4$, $x_{0,1} + x_{0,2} = 1/2$. If $\kappa > \kappa_M^{(0)}$, these rippled low-temperature profiles are not possible and we only have the solution $u = 0$. In Fig. 2.2, we depict an example of these typical profiles for a specific value of κ. Below we show, analysing the low temperature states from the pseudo-spins point of view, that these profiles correspond to pseudo-spins

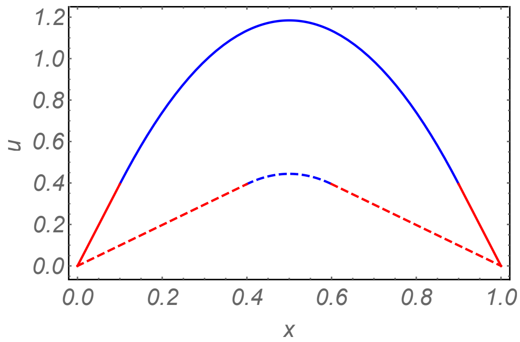

Figure 2.2: Low temperature non-flat string profiles. They comprise two linear zones of width x_0 near the endpoints of the chain (in red) and a parabolic zone in the middle of the system of width $1 - 2x_0$ (in blue). In the linear zones, the pseudo-spins are antiferromagnetically ordered, whereas their order is ferromagnetic in the central parabolic zone, see Fig. 2.3. Specifically, the plot corresponds to a $\kappa = \pi^2/50 < \kappa_t^{(0)}$, which gives two possible values of x_0: $x_{0,1} = 1/10$ (solid line) and $x_{0,2} = 2/5$ (dashed line). The buckled profile corresponding to the larger value $x_{0,2}$ is always unstable. The string profile corresponding to the smaller value gives the absolute minimum of the free energy, since $x_{0,1} < 1/8$, whereas the flat string is metastable.

antiferromagnetically ordered close to the boundaries and ferromagnetically ordered in the bulk.

The linearisation of the Euler-Lagrange equation around these non-flat profiles, see Appendix A.1, proves that the profile corresponds to a relative minimum of the free energy and is thus stable if $x_0 < 1/4$, whereas it is unstable (not a minimum of F) for $x_0 > 1/4$. Then, we have two stable configurations for the string, given by the flat profile and the buckled profile with $x_{0,1} < 1/4$, separated by an unstable configuration, given by the buckled profile with $x_{0,2} > 1/4$ [2]. By direct integration, it is easily shown that the absolute minimum of the free energy corresponds to the buckled configuration with $x_{0,1}$ if $0 < \kappa < \kappa_t^{(0)} = 3\pi^2/128$ ($0 < x_{0,1} < x_t = 1/8$), where the flat profile is thus metastable. The situation is reversed for stronger antiferromagnetic interaction: for $\kappa_t^{(0)} < \kappa < \kappa_M^{(0)}$ ($x_t < x_{0,1} < 1/4$), the flat string is the most stable profile and the configuration corresponding to $x_{0,1}$ is metastable. The existence of metastable states is the signature of a first-order phase transition: in fact, the stable and unstable buckled profiles

[2] In [123], it was incorrectly stated that this configuration was metastable, but this does not affect reference [123] results and conclusions. The instability of the configuration for $x_{0,2}$ can also be shown from the pseudo-spins point of view, see discussion below.

coalesce at $\kappa = \kappa_M^{(0)}$ ($x_{0,1} = x_{0,2} = 1/4$), where they disappear. Consistently, the first-order derivatives of the free energy change discontinuously at coexistence ($\kappa = \kappa_t^{(0)}$): for instance, the order parameters M and $\mathcal{DL}$ jump from $M = 3/4$ and $\mathcal{DL} = 3/4$ over the, most stable, buckled with $x_{0,1}$ phase for $\kappa = \kappa_t^{(0)^-}$ to $M = 0$ and $\mathcal{DL} = 1/2$ over the, most stable, flat phase for $\kappa = \kappa_t^{(0)^+}$.

It is enlightening to look into the low temperature profiles from the perspective of the pseudo-spins. The Euler-Lagrange equation tells us that the string state can be visualised by analysing the pseudo-spins configuration: buckling appears in those regions with non-zero average pseudo-spin. Moreover, this analysis will help us identify the physical mechanism by which there is a phase transition in a one-dimensional system with short-ranged interactions. In a nutshell, the question is that the spin-string coupling entails a long-ranged interaction among the pseudo-spins, similarly to the situation found in other spin-oscillator models [25, 29, 113].

We start by deriving the pseudo-spins' marginal probability $\mathcal{P}(\boldsymbol{\sigma})$, integrating the canonical distribution $\exp(-\mathcal{H}/T)$ over the string degrees of freedom. The result is

$$\mathcal{P}(\boldsymbol{\sigma}) \propto e^{-\mathcal{H}_{\text{eff}}(\boldsymbol{\sigma})/\theta}, \quad \mathcal{H}_{\text{eff}}(\boldsymbol{\sigma}) = \kappa \boldsymbol{\sigma}^{\boldsymbol{T}} \boldsymbol{J} \boldsymbol{\sigma} - \frac{\pi^2}{2N^2} \boldsymbol{\sigma}^{\boldsymbol{T}} \boldsymbol{\Lambda} \boldsymbol{\sigma}, \tag{2.23}$$

in which the matrix $\boldsymbol{J}$ is the matrix restricting the antiferromagnetic interaction to the nearest neigbours,

$$\boldsymbol{J}_{ij} = \frac{1}{2} \left(\delta_{i,j+1} + \delta_{i,j-1} \right) \tag{2.24}$$

and $\boldsymbol{\Lambda}$ has elements

$$\boldsymbol{\Lambda}_{ij} = \frac{1}{N+1} j(N - i + 1) > 0, \quad \forall i \geq j, \quad \boldsymbol{\Lambda}_{ij} = \boldsymbol{\Lambda}_{ji}, \tag{2.25}$$

see Appendix A.2 for details on the derivation. Thus, $\mathcal{H}_{\text{eff}}(\boldsymbol{\sigma})$ can be interpreted as an effective Hamiltonian for the pseudo-spins, which contains a short-ranged antiferromagnetic interaction, given by $\boldsymbol{J}$, and a long-ranged ferromagnetic interaction, given by $\boldsymbol{\Lambda}$.

We focus on the low temperature limit as $\theta \to 0^+$: therein, the equilibrium probability concentrates in the pseudo-spin configuration that corresponds to the absolute minimum of H_{eff}. Therefore, we characterise the H_{eff} landscape: the closer to the centre of the system, the stronger the long-ranged ferromagnetic interaction among the pseudo-spins given by the matrix $\boldsymbol{\Lambda}$. Then, as the intensity of the antiferromagnetic interaction, measured by κ, increases,

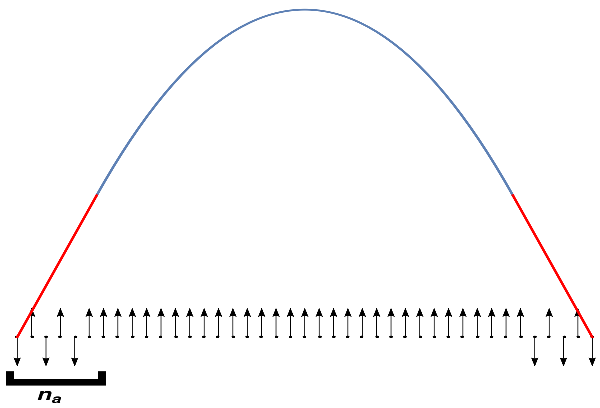

Figure 2.3: Qualitative graph for the typical low-temperature configurations for the pseudo-spins and the string. In the antiferromagnetic regions close to the boundaries, there is no net magnetisation and thus the string has a linear profile ($u'' = 0$, red). In the ferromagnetic region in the bulk, the string takes a parabolic shape ($u'' = -1$, blue). We are plotting a system with $N = 41$ pseudo-spins and $n_a = 5$, which is the number of antiferromagnetic links at either boundary.

we expect the absolute minimum of H_{eff} move from the completely ferromagnetic configuration to one that is antiferromagnetic at the boundaries and ferromagnetic in the bulk of the system.

In light of the previous discussion, we restrict ourselves to states that are antiferromagnetic at the boundaries and ferromagnetic in the centre, in which the completely antiferromagnetic and ferromagnetic states are included. In this projection of space, we label the states by the number n_a of antiferromagnetic links at either side of the system, which can take the values $1, 3, 5, \ldots, N/2$, see Fig. 2.3. Moreover, we denote by $\mathcal{H}_{\text{eff}}(n_a)$ the effective potential for such a configuration. We have that

$$\mathcal{H}_{\text{eff}}(n_a) - \mathcal{H}_{\text{eff}}(n_a - 2) = \frac{2\pi^2}{N^2}\big[-1 + (1 + N - 2n_a)\, n_a\big] - 8\kappa, \tag{2.26}$$

which is derived in Appendix A.3 and can be iterated to obtain

$$\mathcal{H}_{\text{eff}}(n_a) = (n_a - 1)\left\{\frac{\pi^2}{6N^2}[N(3 + n_a)3 - 21 - 13n_a - 4n_a^2] - 4\kappa\right\}. \tag{2.27}$$

The origin of energy has been taken to be such that $\mathcal{H}_{\text{eff}}(n_a = 1) = 0$.

Depending on the value of κ, $\mathcal{H}_{\text{eff}}(n_a)$ has one or two minima, as seen in Fig. 2.4. For $\kappa = 0$, the completely ferromagnetic configuration gives the minimum of H_{eff}, as expected on physical grounds. On the other hand, as κ increases, there appear several relevant values of κ, namely

$$\kappa_0 = \frac{\pi^2}{4}\frac{N-1}{N(N+1)}, \tag{2.28a}$$

$$\kappa_1 = \frac{\pi^2}{384}\frac{9N^2+6N-47}{N^2}, \tag{2.28b}$$

$$\kappa_2 = \frac{\pi^2}{96}\frac{3N^2+6N-5}{N^2}, \tag{2.28c}$$

the physical meaning of which are discussed below. First, for $\kappa = \kappa_0$, the configurations with $n_a = 1$ and $n_a = 0$ share the same value of $\mathcal{H}_{\text{eff}}$. This marks the onset of the antiferromagnetic ordering at the boundaries, although for a large system this ordering is only relevant when n_a/N becomes of the order of unity. In fact, κ_0 is proportional to N^{-1} for large N, whereas both κ_1 and κ_2 become independent of N. Second, at κ_1, the relative minimum of $\mathcal{H}_{\text{eff}}$ has the same value as the completely antiferromagnetic configuration. Finally, at κ_2, this relative minimum disappears and the only stable configuration is that of the absolute minimum for $n_a = N/2$, that is, the completely antiferromagnetic configuration.

The situation described above is illustrated in Fig. 2.4, in which we plot $\mathcal{H}_{\text{eff}}$ as a function of n_a, for different values of κ. For $\kappa < \kappa_1$, the absolute minimum of H_{eff} corresponds to the configuration that is antiferromagnetic at the borders and ferromagnetic in the centre and the flat string is a metastable state, whereas for $\kappa_1 < \kappa < \kappa_2$ the situation is reversed. Of course, in the large N limit, the values of κ at which there are changes in the stability of the solution are in perfect agreement with those obtained from the analysis of the solution of the Euler-Lagrange equation (2.11) for the string profile: κ_1 and κ_2 tend to $\kappa_t^{(0)}$ and $\kappa_M^{(0)}$, respectively. The completely antiferromagnetic configuration leads to an almost flat, wrinkled, string whereas the completely ferromagnetic distribution corresponds to a buckled configuration, with a definite sign of the curvature. Accordingly, the low temperature phase, comprising antiferromagnetic boundaries and a ferromagnetic bulk yields a buckled string with linear (u" $= 0$) boundaries, as depicted in Figs. 2.2 and 2.3.

2.4 Bifurcation from the flat solution. Critical point.

In this section, we investigate in detail the emergence of non-flat solutions that takes place in the vicinity of the bifurcation line (2.19). Therein, we

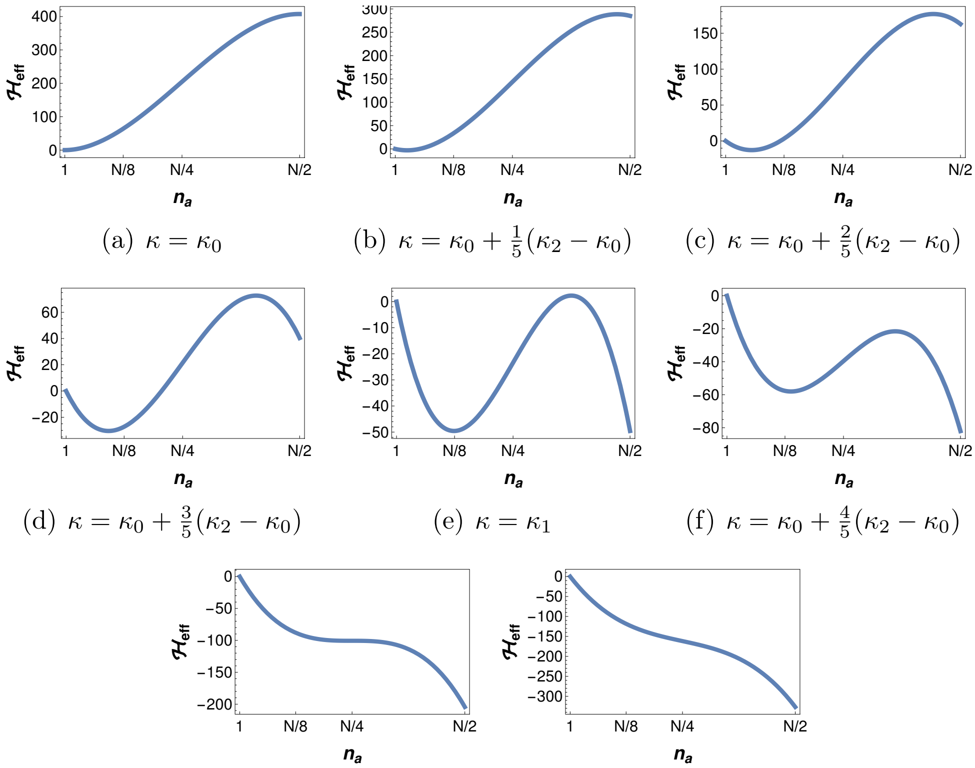

(a) $\kappa = \kappa_0$ (b) $\kappa = \kappa_0 + \frac{1}{5}(\kappa_2 - \kappa_0)$ (c) $\kappa = \kappa_0 + \frac{2}{5}(\kappa_2 - \kappa_0)$

(d) $\kappa = \kappa_0 + \frac{3}{5}(\kappa_2 - \kappa_0)$ (e) $\kappa = \kappa_1$ (f) $\kappa = \kappa_0 + \frac{4}{5}(\kappa_2 - \kappa_0)$

(g) $\kappa = \kappa_2$ (h) $\kappa = \kappa_0 + \frac{6}{5}(\kappa_2 - \kappa_0)$

Figure 2.4: $\mathcal{H}_{\rm eff}$ as a function of the number of antiferro links n_a, for different values of κ. In the limit as $\theta \to 0^+$, the probability concentrates in the *absolute* minimum of $H_{\rm eff}$. (a): $\kappa = \kappa_0$, the absolute minimum corresponds to $n_a = 1$. (b)-(d): $\kappa_0 < \kappa < \kappa_1$: the absolute minimum (here also the relative one) shifts to greater values of n_a. (e): $\kappa = \kappa_1$, the relative minimum has the same value of $\mathcal{H}_{\rm eff}$ as the configuration with $n_a = N/2$, that is, the completely antiferromagnetic state. (f): $\kappa_1 < \kappa < \kappa_2$, the absolute minimum corresponds to the completely antiferromagnetic configuration, since its value of $H_{\rm eff}$ is lower than that at the relative minimum. (g): $\kappa = \kappa_2$, the relative minimum disappears and the only equilibrium state is the completely antiferromagnetic one.

expect the possible non-flat (or buckled) solutions to be "small", in the sense that the free energy density, the local magnetisation, etc. can be expanded in powers of u.

We start by expanding the free energy around the flat solution,

$$f(u,u';\kappa,\theta) - f_{\rm L}(\kappa,\theta) = \frac{1}{2\pi^2}(u')^2 + \frac{1}{2!}f_2(\kappa,\theta)u^2 + \frac{1}{4!}f_4(\kappa,\theta)u^4 + \frac{1}{6!}f_6(\kappa,\theta)u^6 + O(u^8), \tag{2.29}$$

in which

$$f_{\rm L}(\kappa,\theta) = f(u=0,u'=0;\kappa,\theta) = -\theta\ln\left(2\cosh\frac{\kappa}{\theta}\right), \tag{2.30}$$

is the free energy density for the flat profile, and

$$f_n(\kappa,\theta) \equiv \left.\frac{\partial^n f(u,u';\kappa,\theta)}{\partial u^n}\right|_{u=0} = -\left.\frac{\partial^{n-1}\mu(u;\kappa,\theta)}{\partial u^{n-1}}\right|_{u=0}. \tag{2.31}$$

Taking into account Eq. (2.12), we have that

$$f_2(\kappa,\theta) = -\frac{e^{-2\kappa/\theta}}{\theta}, \tag{2.32a}$$

$$f_4(\kappa,\theta) = \frac{e^{-6\kappa/\theta}}{\theta^3}\left(3-e^{4\kappa/\theta}\right), \tag{2.32b}$$

$$f_6(\kappa,\theta) = -\frac{e^{-10\kappa/\theta}}{\theta^5}\left(45-30e^{4\kappa/\theta}+e^{8\kappa/\theta}\right). \tag{2.32c}$$

The bifurcation line is expressed thus as

$$f_{2,b} \equiv f_2(\kappa_b,\theta_b) = -1, \tag{2.33}$$

at which a sinusoidal, non-vanishing, solution arises. We consider a point (κ,θ) close to the bifurcation line,

$$\delta\kappa = \kappa-\kappa_b = \epsilon\eta_\kappa, \quad \delta\theta = \theta-\theta_b = \epsilon\eta_\theta, \quad 0<\epsilon\ll 1, \tag{2.34a}$$

so that the small parameter ϵ measures the separation from the bifurcation line. The sign of $(\eta_\kappa,\eta_\theta)$ determines the sign of $(\delta\kappa,\delta\theta)$, respectively. Consistently, we evaluate f_2 up to linear order in the deviations, by defining $\delta f_{2,b}$ as

$$\delta f_{2,b} \equiv f_2(\kappa,\theta) - f_{2,b} = f_{2,b}^{(\theta)}\delta\theta + f_{2,b}^{(\kappa)}\delta\kappa, \tag{2.35}$$

where we have introduced the notation

$$f_{2,b}^{(\theta)} = \frac{1+\ln\theta_b}{\theta_b}, \quad f_{2,b}^{(\kappa)} = \frac{2}{\theta_b}. \tag{2.36}$$

It is convenient to define

$$\varphi_{2,b} \equiv \frac{\delta f_{2,b}}{\epsilon} = f_{2,b}^{(\theta)} \eta_\theta + f_{2,b}^{(\kappa)} \eta_\kappa, \quad \varphi_{2,b} = O(1). \tag{2.37}$$

Therefore, ϵ can be considered as a measure of the order of magnitude of the (small) value of $|\delta f_{2,b}|$. It is clear that $\delta f_{2,b}$ (or $\varphi_{2,b}$) vanishes over the bifurcation line, see Eq. (2.20). Then, it is the sign of $\delta f_{2,b}$ or $\varphi_{2,b}$ that tells us at which side of the bifurcation line the point (κ, θ) lies. Specifically,

$$\delta f_{2,b} \text{ or } \varphi_{2,b} < 0 \Rightarrow (\kappa, \theta) \text{ is inside the bifurcation line,} \tag{2.38a}$$

$$\delta f_{2,b} \text{ or } \varphi_{2,b} > 0 \Rightarrow (\kappa, \theta) \text{ is outside the bifurcation line.} \tag{2.38b}$$

It suffices to obtain the values of f_4 and f_6 over the bifurcation line, which we denote by $f_{4,b}$ and $f_{6,b}$, respectively:

$$f_{4,b} = \frac{3\theta_b^2 - 1}{\theta_b^2}, \quad f_{6,b} = \frac{-45\theta_b^4 + 30\theta_b^2 - 1}{\theta_b^4}. \tag{2.39}$$

Note that, since the "coefficients" $\varphi_{2,b}$, $f_{2,b}^{\theta}$, $f_{2,b}^{\kappa}$, $f_{4,b}$ anf $f_{6,b}$ are evaluated over the bifurcation line, they depend only on θ_b. Also, we expand $u(x)$ close to the bifurcation line by assuming that

$$u(x) = \epsilon^\alpha \sum_{j=0}^{\infty} \epsilon^{\beta j}\, U_j(x), \qquad U_j(0) = U_j(1) = 0,\ \forall j, \tag{2.40}$$

where α and β are determined by seeking a consistent distinguished limit in the expansion of the Euler-Lagrange equation in powers of ϵ, that is,

$$\frac{1}{\pi^2} u'' + u = \delta f_{2,b}\, u + \frac{1}{3!} f_4\, u^3 + \frac{1}{5!} f_6\, u^5 + O(u^7). \tag{2.41}$$

We have that $U_0(x)$ is controlled by the lowest order terms, proportional to ϵ^α on the lhs of Eq. (2.41), which yield

$$\frac{1}{\pi^2} U_0''(x) + U_0(x) = 0 \implies U_0(x) = A \sin \pi x. \tag{2.42}$$

Note that A remains arbitrary to the lowest order: in fact, it is determined by the next order equation. Therein, the terms on the lhs of Eq. (2.41) containing $U_1(x)$, which are proportional to $\epsilon^{\alpha+\beta}$, must balance with the dominant terms on the rhs, which are (i) $\delta f_{2,b} u \sim \epsilon^{1+\alpha} \varphi_{2,b} U_0$ and

(ii) $f_4 u^3/3! \sim \epsilon^{3\alpha} f_{4,b} U_0^3/3!$. The fifth-order term in subdominant with respect to the third-order one if $f_{4,b} = O(1)$, the case $f_{4,b} \ll 1$ will be studied afterwards. Therefore, $\alpha + \beta = 1 + \alpha = 3\alpha$, which gives $\alpha = 1/2$ and $\beta = 1$, and the equation for $U_1(x)$ is

$$\frac{1}{\pi^2} U_1''(x) + U_1(x) = \varphi_{2,b} U_0(x) + \frac{1}{3!} f_{4,b} U_0^3(x). \tag{2.43}$$

Now, the constant A in $U_0(x)$ is fixed by the rhs of Eq. (2.43) being orthogonal to $U_0(x)$, which entails

$$\varphi_{2,b} A + f_{4,b} \frac{A^3}{8} = 0. \tag{2.44}$$

The above equation has the solutions $A = 0$ (flat solution) and

$$A^2 = -8 \frac{\varphi_{2,b}}{f_{4,b}}, \tag{2.45}$$

which correspond to sinusoidal buckled solutions.

The sign of $f_{4,b}$ controls the side of the bifurcation line at which the buckled solutions appear. Note that $f_{4,b}$ vanishes at $\theta_b = \theta_c = 1/\sqrt{3}$, $f_{4,b} > 0$ for $\theta_b > \theta_c$ and $f_{4,b} < 0$ for $\theta_b < \theta_c$. Thus, there are two different situations

1. $f_{4,b} > 0$ or $\theta_b > \theta_c$, that is, we are to the left of θ_c, moving over the upper branch of the bifurcation line in Fig. 2.1. Therein,

$$\varphi_{2,b} < 0 \text{ or } \delta f_{2,b} < 0 \tag{2.46}$$

to ensure that $A^2 > 0$. Therefore, the buckled solution arises inside the bifurcation line, where the flat solution has become unstable, and we have a supercritical bifurcation.

2. $f_{4,b} < 0$ or $\theta_b < \theta_c$, that is, we are to the right of θ_c, moving over the upper branch of the bifurcation line, or at any point over the lower branch thereof in Fig. 2.1. Here,

$$\varphi_{2,b} > 0 \text{ or } \delta f_{2,b} > 0 \tag{2.47}$$

and the bifurcation becomes subcritical: the buckled solution emerges outside the bifurcation line, where the flat solution is (locally) stable.

In this way, the point over the upper branch of the bifurcation line at which $f_{4,b}$ vanishes is a critical point: at $K \equiv (\kappa_c, \theta_c)$, the bifurcation changes from supercritical to subcritical. To the left of K, the bifurcation line corresponds to a second-order (continuous) transition line: (i) outside the bifurcation line, the flat solution is the stable profile, and the buckled solution does not exist and (ii) inside the bifurcation line, the flat solution still exists but is unstable, whereas the new buckled solution emerge continuously from the bifurcation line and is stable. To the right of K, the change to a subcritical bifurcation is the signature of the arising of a new first-order transition line and the situation is more complex [68, 88, 128, 145]. Moreover, f_{4b} tends to zero in the vicinity of the critical point, Eq. (2.45) ceases to be valid, and a different approach is needed.

2.4.1 A closer look into the vicinity of the critical point

Since $f_{4,b}$ vanishes at $\theta_b = \theta_c$, let as assume that $f_{4,b} = O(\epsilon^{2\alpha})$, so that the dominant terms in Eq. (2.41) that are proportional to u^3 and u^5 are of the same order, specifically $\epsilon^{5\alpha}$. The new dominant balance gives $\alpha = 1/4$ and $\beta = 1$.

The new scaling is relevant when $|\theta_b - \theta_c| = O(\sqrt{\epsilon})$ and we can thus write

$$\theta_b = \theta_c + \sqrt{\epsilon}\,\chi, \tag{2.48a}$$

$$f_{4,b} \sim f_{4,c}^{(1)} \equiv \left.\frac{df_{4,b}}{d\theta_b}\right|_{\theta_c} (\theta_b - \theta_c) = \sqrt{\epsilon}\frac{6\chi}{\theta_c} + O(\epsilon). \tag{2.48b}$$

The parameter $\chi = O(1)$ carries with it the sign of $\theta_b - \theta_c$ (or $f_{4,b}$). Taking into account Eq. (2.45), the amplitude A of the sinusoidal profile far from the critical point scales as

$$A^2 \sim -\frac{1}{\sqrt{\epsilon}}\frac{4\theta_c}{3}\varphi_{2,c}\chi^{-1}. \tag{2.49}$$

Note that this is consistent with the new dominant balance, if $A^2 = O(\epsilon^{-1/2})$, we have that $u(x) \sim \epsilon^{1/2} A \sin(\pi x) = O(\epsilon^{1/4})$. We have used the notation $\varphi_{2,c}$ for the value of $\varphi_{2,b}$ at the critical point, that is, $\varphi_{2,c} \equiv \varphi_{2,b}|_{\theta_b=\theta_c}$.

The equation for $U_0(x)$ is the same as before, then we have

$$U_0(x) = \tilde{A}\sin(\pi x), \quad u(x) \sim \epsilon^{1/4} U_0(x), \tag{2.50}$$

in which we denote the amplitude of the sinusoidal profile in this region by $\tilde{A}$. The equation for $U_1(x)$ is now

$$\frac{1}{\pi^2}U_1'' + U_1 = \varphi_{2,c}\,U_0 + \frac{1}{3!}\frac{6\chi}{\theta_c}U_0^3 + \frac{1}{5!}f_{6,c}U_0^5, \tag{2.51}$$

with

$$f_{6,c} = \frac{12}{\theta_c^2} \tag{2.52}$$

being the value of $f_{6,b}$ at the critical point. By imposing again that the rhs must be orthogonal to $\sin(\pi x)$, we obtain the equation for the amplitude $\tilde{A}$ (aside from $\tilde{A} = 0$, of course),

$$\frac{1}{2}\tilde{A}^4 + 6\theta_c \chi \tilde{A}^2 + 8\theta_c^2 \varphi_{2,c} = 0. \tag{2.53}$$

Solving for $\tilde{A}$,

$$\tilde{A}_\pm^2 = 6\theta_c \left(-\chi \pm \sqrt{\chi^2 - \frac{4}{9}\varphi_{2,c}} \right). \tag{2.54}$$

Now, we look separately into the cases $\chi > 0$ and $\chi < 0$, which correspond to $\theta > \theta_c$ and $\theta < \theta_c$, respectively.

Above the critical point K, $\chi > 0$ or $\theta > \theta_c$. In Eq. (2.54), only the plus sign makes sense and we have

$$\tilde{A}_+^2 = 6\theta_c \left(-\chi + \sqrt{\chi^2 - \frac{4}{9}\varphi_{2,c}} \right), \tag{2.55}$$

provided that $\varphi_{2,c} < 0$. Then, the non-flat solution still stems from the line $\varphi_{2,c} = 0$, at which we have that $\tilde{A}_+^2 = 0$, that is, the transition is second-order to the left of the critical point. Moreover, it smoothly matches with the *outer solution* that we derived before, which is valid far enough from it. It is straightforward to show that

$$\tilde{A}_+^2 \sim -\frac{4\theta_c}{3}\varphi_{2,c}\chi^{-1}, \quad \chi^2 \gg \frac{4}{9}|\varphi_{2,c}|, \tag{2.56}$$

consistently with Eq. (2.49).

We call this buckled phase, which is described by Eqs. (2.45) and (2.46) far from the critical point and by Eq. (2.55) close to it, B+ (Buckled phase with the plus sign in the amplitude).

Below the critical point K, $\chi < 0$ or $\theta < \theta_c$. Now, both the plus and minus signs in Eq. (2.54) make sense. First, we take a look at the solution with the plus sign, which continuously propagates the phase B+ to the right of K. However, now $\tilde{A}_+$ exists only if the argument of the square root is non-negative, that is,

$$\varphi_{2,c} \le \frac{9}{4}\chi^2, \quad \chi < 0 \text{ or } \theta < \theta_c. \tag{2.57}$$

This means that this solution dies at the above line, which marks the limit of existence of the phase B+. Moreover, at that line $\tilde{A}_+^2 = -6\theta_c\chi \neq 0$, making it clear that a new first-order-transition line arises to the right of the critical point. For a fixed value of θ, Eq. (2.57) is equivalent to

$$\kappa(\theta) \leq \kappa_M(\theta) = \kappa_b(\theta) + \frac{9}{4f_{2,c}^{(\kappa)}}(\theta - \theta_c)^2, \quad \theta < \theta_c, \tag{2.58}$$

where $f_{2,c}^{(\kappa)}$ stands for the value of $f_{2,b}^{(\kappa)}$, defined in Eq. (2.35), at the critical point, that is, $f_{2,c}^{(\kappa)} = 2/\theta_c$. Then, $\kappa_M(\theta)$ describes the first-order-transition line in the vicinity of the critical point, $|\theta - \theta_c| \ll 1$. Note also that, over the bifurcation line ($\varphi_{2,c} = 0$) $\tilde{A}_+^2 = -12\theta_c\chi > 0$ and this solution extends itself inside the bifurcation line.

Now, we turn our attention to the solution with the minus sign, which introduces a new phase that exists only to the right of the critical point. We call this new phase B-, and its corresponding amplitude is given by

$$\tilde{A}_-^2 = -6\theta_c\chi - 6\theta_c\sqrt{\chi^2 - \frac{4}{9}\varphi_{2,c}}\,. \tag{2.59}$$

In order to have $\tilde{A}_-^2 \geq 0$, we have to impose that the argument of the square root be non-negative, as before, and moreover that $\varphi_{2,c} \geq 0$. Proceeding along the same lines as above, this is equivalent to

$$0 \leq \varphi_{2,c} \leq \frac{9}{4}\chi^2, \tag{2.60}$$

or, for a fixed value of θ,

$$\kappa_b(\theta) \leq \kappa(\theta) \leq \kappa_M(\theta). \tag{2.61}$$

Therefore, the phase B- only exists between the bifurcation line and the first-order transition line. In fact, $\tilde{A}_-$ vanishes at the bifurcation line $\kappa_b(\theta)$ (over which $\varphi_{2,c} = 0$) and merges with $\tilde{A}_+$ at the first-order-transition line $\kappa_M(\theta)$ (over which the argument of the square root vanishes). Far enough from the critical point, that is, for $\varphi_{2,c} \ll 9\chi^2/4$, $\tilde{A}_-$ smoothly matches the *outer solution* given by Eqs. (2.45) and (2.47) to the right of the critical point. Therein, along the same lines as in the derivation of Eq. (2.49), it is found that $\tilde{A}_-^2 \sim -\frac{4}{3}\theta_c\varphi_{2,c}\chi^{-1}$.

In the literature, a critical point K like the one described above, at which three phases coalesce, is sometimes called a tricritical point [128, 145]. Here, the three phases are the flat phase L and the two buckled phases $B\pm$. The stability thereof is discussed in the next section.

2.4.2 Stability of the phases

In order to elucidate the stability of the different phases, we have to calculate the total free energy that corresponds to each of the string profiles that solves the Euler-Lagrange equation. First, we have the phase L, corresponding to the flat profile $u_{\mathrm{L}}(x) \equiv 0$. Second, we also have the buckled phases $B\pm$, which correspond to the sinusoidal buckled string profiles just obtained by a perturbative expansion close to the bifurcation line. Here, we denote these sinusoidal string profiles by $u_S(x)$,

$$u_S(x; C) = C \sin(\pi x), \tag{2.62}$$

We could make use of the values of the amplitude obtained before, when solving perturbatively the Euler-Lagrange equation. Notwithstanding, we follow here a different approach, which gives the same results but provides additional, physically relevant, information. The difference of free energies between the sinusoidal and the flat profiles is given by

$$\Delta F(C; \kappa, \theta) \equiv \int_0^1 dx \left[f(u_S, u_S'; \kappa, \theta) - f_{\mathrm{L}}(\kappa, \theta) \right]. \tag{2.63}$$

Note that ΔF is no longer a functional but a function of the (unknown) amplitude C. Within the same level of approximation as we have been working throughout, we have

$$\Delta F(C; \kappa, \theta) \sim \int_0^1 dx \left(\frac{1}{2} \delta f_{2,b} u_S^2 + \frac{1}{4!} f_{4b} u_S^4 + \frac{1}{6!} f_{6b} u_S^6 \right). \tag{2.64}$$

The idea is to find the extrema of ΔF as a function of C, see below.

Far from the critical point, consistently with the procedure for solving perturbatively the Euler-Lagrange equation, the term proportional to u^6 can be neglected and by substituting Eq. (2.62) into (2.64), it is readily obtained that

$$\Delta F(C) \sim \frac{1}{4} \delta f_{2,b} C^2 + \frac{1}{64} f_{4b} C^4. \tag{2.65}$$

To simplify our notation, we omit the dependence on (κ, θ) of ΔF hereafter. The equilibrium values of C, which we denote by C_{eq}, can be found by seeking the extrema of $\Delta F(C)$. Then, they obey

$$\frac{1}{2} \delta f_{2,b} C_{\mathrm{eq}} + \frac{1}{16} f_{4b} C_{\mathrm{eq}}^3 = 0, \tag{2.66}$$

which entails

$$C_{\mathrm{eq}}^2 = -\frac{8 \delta f_{2,b}}{f_{4b}} \Rightarrow C_{\mathrm{eq}} = \sqrt{\epsilon} A, \tag{2.67}$$

by comparing these equations with Eqs. (2.44) and (2.45). Taking into account Eq. (2.67), we have that

$$\Delta F_{\text{eq}} \sim -\frac{\delta f_{2,b}^2}{f_{4,b}}. \tag{2.68}$$

which shows that the sign of ΔF_{eq} is controlled by the sign of $f_{4,b}$.

The stability of the phases can be further elucidated by looking at the sign of the second derivative of ΔF with respect to C. Since

$$\frac{\partial^2 \Delta F}{\partial C^2} = \frac{\delta f_{2,b}}{2} + \frac{3}{16} f_{4b} C^2, \tag{2.69}$$

we have that

$$\left.\frac{\partial^2 \Delta F}{\partial C^2}\right|_{\text{eq}} = -\delta f_{2,b}. \tag{2.70}$$

Therefore, the stability is controlled by the sign of $\delta f_{2,b}$: to the left of the critical point, the phase B+ exists inside the bifurcation line, where the flat phase L becomes unstable, and is thus stable: $\delta f_{2,b} < 0$ and $\left.\frac{\partial^2 F(C)}{\partial C^2}\right|_{B+} > 0$ (consistently, $\Delta F_{\text{eq}}|_{B+} < 0$). To the right of the critical point, the phase B- emerges outside the bifurcation line, where the flat phase is stable, and is unstable: $\delta f_{2,b} > 0$ and $\left.\frac{\partial^2 F(C)}{\partial C^2}\right|_{B-} < 0$ (consistently, $\Delta F_{\text{eq}}|_{B-} > 0$). The phase B- is indeed unstable but it does not correspond to a (local) maximum of the free energy functional, but to some kind of “saddle point” extremum that is neither a minimum nor a maximum [3].

In the vicinity of the tricritical point K, we have to keep the u^6 term, and substitute the coefficients of the quadratic and quartic terms by their leading behaviours. With the same notation as in the previous section,

$$\Delta F(C) \sim \frac{1}{4}\delta f_{2,c} C^2 + \frac{1}{64} f_{4,c}^{(1)} C^4 + \frac{1}{2304} f_{6,c} C^6. \tag{2.71}$$

Again, C_{eq} can be found by looking for the extrema of ΔF,

$$\frac{1}{2}\delta f_{2,c} C_{\text{eq}} + \frac{1}{16} f_{4,c}^{(1)} C_{\text{eq}}^3 + \frac{1}{384} f_{6,c} C_{\text{eq}}^5 = 0. \tag{2.72}$$

By taking into account the values of $f_{4,c}^{(1)}$ and $f_{6,c}$, as given by Eqs. (2.48) and (2.52), respectively, and $\delta f_{2,c} = \epsilon \varphi_{2,c}$, it is shown that

$$C_{\text{eq}} = \epsilon^{1/4} \tilde{A}. \tag{2.73}$$

[3]Note that the phase B+ cannot be produced by an expansion around the flat solution to the right of the critical point, because its amplitude does not vanish at the bifurcation line. This is the reason why the solution obtained to the right of the critical point corresponds to the phase B-.

Again, the local stability of the phases is given by the second derivative of ΔF at equilibrium. After a little algebra, we get the result

$$\left.\frac{\partial^2 \Delta F}{\partial C^2}\right|_{B\pm} = \pm\epsilon \frac{3}{4\theta_c}\tilde{A}_{\pm}^2 \sqrt{\chi^2 - \frac{4}{9}\varphi_{2,c}}. \tag{2.74}$$

The above equation tells us that the phase B+ is locally stable whereas the phase B- is unstable. Of course, this is so for their respective domains of existence to the right of the critical point, recall that the phase B+ exists below the first-order line, $\kappa < \kappa_M(\theta)$, whereas the phase B- only exists between the bifurcation line and the first-order line, $\kappa_b(\theta) < \kappa < \kappa_M(\theta)$. Over the first-order-line, at which the phases $B\pm$ merge and disappear, the argument of the square root becomes equal to zero and $\partial^2\Delta F/\partial C^2|_{B\pm} = 0$. To the left of the critical point, only the plus sign is possible and Eq. (2.74) smoothly matches with Eq. (2.70), after taking into account Eq. (2.56).

Further analysis is necessary to find out which of the two locally stable phases, the flat L phase and the buckled B+ phase, gives the absolute minimum of the free energy and then it corresponds to the *true* equilibrium configuration, whereas the other phase is metastable. Then, we calculate ΔF at equilibrium,

$$\Delta F|_{\text{eq}} = \epsilon^{3/2}\frac{f_{6,c}}{2304}\tilde{A}^2\left(\tilde{A}^4 + 18\theta_c\chi\tilde{A}^2 + 48\theta_c^2\varphi_{2,c}\right). \tag{2.75}$$

Substitution of $\tilde{A}$ into the above equation gives, for the $B\pm$ phases,

$$\Delta F_{B\pm} = \epsilon^{3/2}\frac{f_{6,c}}{576}\tilde{A}_{\pm}^2\theta_c^2\left[-9\chi^2 + 8\varphi_{2,c} \pm 3\chi\sqrt{9\chi^2 - 4\varphi_{2,c}}\right] \tag{2.76}$$

To the left of the critical point, $\chi > 0$, only the upper sign is possible and $\Delta F_{B+} = 0$ over the bifurcation line $\varphi_{2,c} = 0$. Inside it, we have $\varphi_{2,c} < 0$ and consistently $\Delta F_{B+} < 0$: the only relative minimum, and thus the absolute one, is attained for the buckled B+ phase. To the right of the critical point, $\chi < 0$, and both signs are possible. On the one hand, consistently with its unstable character, $\Delta F_{B-} \geq 0$, it varies from $\Delta F_{B-} = 0$ over the bifurcation line $\kappa_b(\theta)$, at which A_- vanishes, to the positive value

$$\Delta F_B^{\max} = \epsilon^{3/2}\frac{f_{6,c}}{64}\tilde{A}^2\theta_c^2\chi^2 > 0 \tag{2.77}$$

at the first-order line $\kappa_M(\theta)$. On the other hand, $\Delta F_{B+} < 0$ at the bifurcation line (note that $\sqrt{9\chi^2} = -3\chi$ for $\chi < 0$), whereas $\Delta F_{B+} = \Delta F_B^{\max} > 0$ at the first order line because the phases $B\pm$ merge. Thus, there must be a line at which ΔF_{B+} changes sign when moving from the bifurcation line to the first-order line. Making use of Eq. (2.76), this line is determined by the condition $\varphi_{2,c} = 27\chi^2/16$ or

$$\kappa_t(\theta) = \kappa_b(\theta) + \frac{27}{16 f_{2,c}^{(\kappa)}}(\theta - \theta_c)^2, \quad \theta < \theta_c, \ |\theta - \theta_c| \ll 1 \tag{2.78}$$

The above equation gives the coexistence line in the vicinity of the critical point, at which the free energy minima for the phases B+ and L are equally deep and both phases are equiprobable. For $\kappa_b(\theta) < \kappa < \kappa_t(\theta)$, the most stable phase is B+, whereas the flat phase L is metastable; the situation is just reversed in the region $\kappa_t(\theta) < \kappa < \kappa_M(\theta)$.

2.5 Phase diagram in the plane (κ, θ)

We start by summarising the different phases found in the analysis carried out throughout the previous sections. Above the critical point K $(\theta > \theta_c)$, there is only one buckled phase B+ that exists and is stable inside the bifurcation line, that is, for $\kappa < \kappa_b(\theta)$. In this region, the flat phase L is unstable. At the bifurcation line, the phase B+ changes continuously to the phase L: in fact, outside the bifurcation line, $\kappa > \kappa_b(\theta)$, the only equilibrium string profile is flat. Below the critical point $(\theta < \theta_c)$, still we have only the buckled phase B+ to be stable inside the bifurcation line, where the flat solution continues to be unstable. At the bifurcation line, the phase B+ does not merge any longer with the flat phase, the amplitude of the sinusoidal profile does not vanish and the buckled phase B+ has a lower free energy than the flat phase, $\Delta F_{B+} < 0$. Moreover, a new buckled phase B-, which is unstable, emerges continuously from the flat solution at the bifurcation line. Both buckled solutions are present for $\kappa_b(\theta) < \kappa < \kappa_M(\theta)$, in which $\kappa_M(\theta)$ is a new first-order-transition line at which both phases $B\pm$ coincide and disappear abruptly (the amplitude of the sinusoidal profile is different from zero at $\kappa = \kappa_M(\theta)$). In the region $\kappa_b(\theta) < \kappa < \kappa_M(\theta)$, both the phase L and the phase B+ are locally stable, since they correspond to relative minima of the free energy. There appears a coexistence line $\kappa_t(\theta)$, at which both minima are equally deep. For $\kappa_b(\theta) < \kappa < \kappa_t(\theta)$, the absolute minimum of the free energy is that of the phase B+ and the flat phase L is metastable; for $\kappa_t(\theta) < \kappa < \kappa_M(\theta)$ the situation is reversed. A qualitative picture of this phase diagram is provided in Fig. 2.5.

In the low temperature region, we have found that (i) the flat phase L is always locally stable, since $\lim_{\theta\to 0^+} \kappa_b(\theta) = 0$, and (ii) there appear

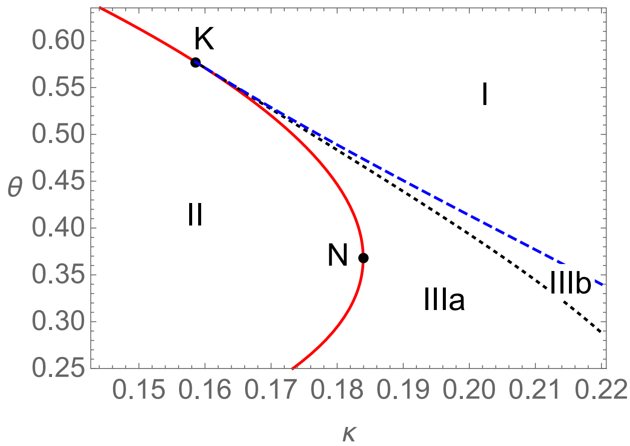

Figure 2.5: Zoom of the phase diagram in a region close to the critical point K including the nose N of the bifurcation curve. The solid line represents the bifurcation line $\kappa_b(\theta)$, and the dotted and dashed lines correspond to the coexistence line $\kappa_t(\theta)$ and the first-order line $\kappa_M(\theta)$, $\kappa_b(\theta) < \kappa_t(\theta) < \kappa_M(\theta)$, respectively. These three lines delimit different zones of the phase diagram: in zone I ($\kappa > \kappa_M(\theta)$), there is only one phase, the flat phase L, whereas in zone II ($\kappa < \kappa_b(\theta)$) there are two possible phases: the flat phase is unstable and the buckled B+ is stable. In zone III ($\kappa_b(\theta) < \kappa < \kappa_M(\theta)$), the situation is more complex, the three phases L, B+ and B- exist but the latter is always unstable. The relative stability of the locally stable phases therein, B+ and L, changes when one moves from zone IIIa ($\kappa_b(\theta) < \kappa < \kappa_t(\theta)$) to IIIb ($\kappa_t(\theta) < \kappa < \kappa_M(\theta)$). In zone IIIa, it is the phase B+ that gives the absolute minimum of the free energy and the flat phase L is metastable, while the relative stability of these phases is reversed in zone IIIb.

two buckled phases, with linear profiles (antiferromagnetic ordering of the pseudo-spins) in the edges of the system and parabolic profiles (ferromagnetic ordering) in the system bulk for $\kappa < \kappa_M^{(0)} = \pi^2/32$. The two phases differ in the length x_0 of the antiferromagnetic regions at the edges, $x_{0,1} < 1/4 < x_{0,2}$. The phase with the larger value $x_{0,2}$ is unstable, whereas that with the smaller value $x_{0,1}$ corresponds to a relative minimum of the free energy. Interestingly, the buckled phase with $x_{0,1}$ is the most stable one for small enough κ, specifically $\kappa < \kappa_t^{(0)} = 3\pi^2/128$, where the flat phase is thus metastable. Conversely, for $\kappa_t^{(0)} < \kappa < \kappa_M^{(0)}$, the buckled phase with $x_{0,1}$ is metastable and the flat phase is the most stable one.

The situation described in the two previous paragraphs is completely compatible with the following physical picture: there are three phases in our system, which we call B+, B- and L, extending the nomenclature used in the vicinity of the critical point to the whole temperature range. For $\theta < \theta_c$, the existence and properties of these phases are qualitatively similar to those described in the first paragraph. The existence and properties of the phases are controlled by the bifurcation line $\kappa_b(\theta)$, the coexistence line $\kappa_t(\theta)$ and the first-order-line $\kappa_M(\theta)$, for which we have obtained approximate expressions when $|\theta - \theta_c| \ll 1$. We expect that the coexistence and first-order lines propagate to low temperatures with the properties $\lim_{\theta\to 0^+} \kappa_t(\theta) = \kappa_t^{(0)}$ and $\lim_{\theta\to 0^+} \kappa_M(\theta) = \kappa_M^{(0)}$, respectively.

In region II, that is, inside the bifurcation line, $\kappa < \kappa_b(\theta)$, the phase B+ is the only stable phase whereas the flat phase L is unstable. In region III, between the bifurcation and the first-order lines, $\kappa_b(\theta) < \kappa < \kappa_M(\theta)$, this phase B+ continues to exist and is locally stable throughout, changing from the sinusoidal profile with amplitude $\tilde{A}_+$ to the linear-parabolic phase with $x_{0,1} < 1/4$ as the temperature is decreased from $\theta \to \theta_c^-$ to $\theta \to 0^+$. In this region, both B+ and the flat phase L are locally stable, with their relative stability changing at the coexistence line $\kappa_t(\theta)$. In addition, there appears an unstable phase B- that continuously changes from the sinusoidal profile with amplitude $\tilde{A}_-$ close to θ_c to the linear-parabolic phase with $x_{0,2} > 1/4$ for very low temperatures. In region I, $\kappa > \kappa_M(\theta)$, the antiferromagnetic interaction is too strong and no longer do buckled phases appear: the only possible equilibrium profile for the string is flat.

In order to complete and check the physical picture depicted above, we have integrated numerically the Euler-Lagrange equation to find the equilibrium profiles over a representative grid of points in the (κ, θ) plane. Specifically, we have considered a grid of 200×200 points in the rectangle $[0, 0.5] \times [0, 1]$. The numerical integration has been done in the half interval $x \in [0, 1/2]$, with the boundary conditions $u(0) = 0$, $u'(1/2) = 0$, because

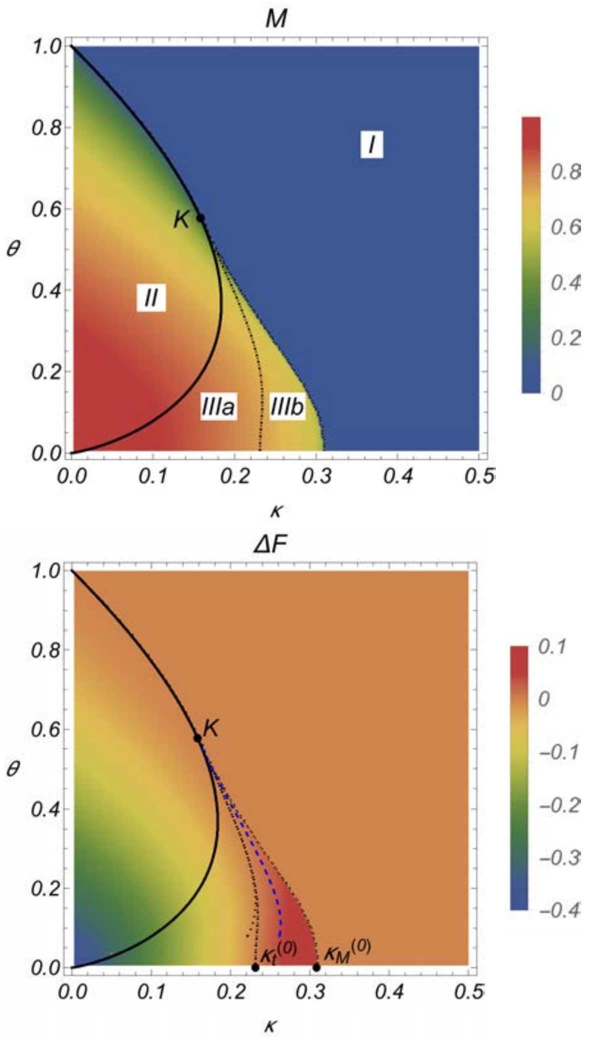

Figure 2.6: Density plot of the magnetisation M and the free energy difference ΔF over the numerical solution of the Euler-Lagrange equation for the phase B+. The magnetisation M and the free energy difference ΔF are shown in the top and bottom panels, respectively. In both panels, also plotted are the bifurcation line (solid) $\kappa_b(\theta)$ and the first order transition lines (dotted): at the coexistence line $\kappa_t(\theta)$, $\Delta F = 0$, whereas the buckled solution disappears at the limit line $\kappa_M(\theta)$, beyond which only the flat phase exists (both $\Delta F = 0$ and $M = 0$). For the sake of clarity, we provide some additional information, but different in each panel. In the magnetisation panel, we have also marked the critical point K and labelled the different phases. In the free energy panel, we plot the analytical expressions close to the critical point for the first-order transition lines $\kappa_t(\theta)$ and $\kappa_M(\theta)$, as given by Eqs. (2.78) and (2.58), respectively, but extended up to low temperatures, namely for $\theta \geq 0.08$.

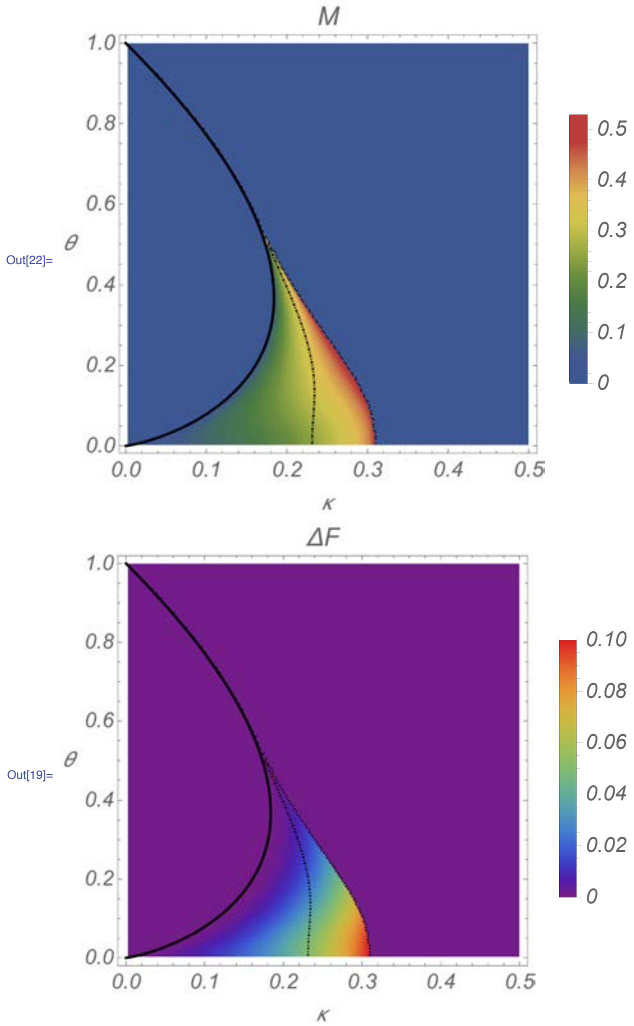

Figure 2.7: Density plot of the magnetisation M and the free energy difference ΔF over the numerical solution of the Euler-Lagrange equation for the phase B-. Again, the magnetisation M and the free energy difference ΔF are shown in the top and bottom panels, respectively.

we are interested in string profiles $u(x)$ with no internal nodes. We have employed a shooting method to solve the boundary-value problem, in particular its built-in implementation in Wolfram Mathematica®.

First, we have allowed Mathematica® to choose automatically the shooting parameter $u'(0)$ (of course, $u(0) = 0$). In this way, the buckled phase B+ is found in its domain of existence, $\kappa \leq \kappa_M(\theta)$ (regions II and III). For $\kappa \geq \kappa_M(\theta)$ (region I), the found solution is, logically, the flat one.

In Fig. 2.6, we present density plots for the numerical estimates for the magnetisation order parameter M (top panel) and the free energy difference ΔF (bottom panel) as functions of (κ, θ). Therein, we also show the numerical results for the coexistence line $\kappa_t(\theta)$, obtained by imposing that $|\Delta F| \leq 10^{-10}$, and the limit line $\kappa_M(\theta)$, beyond which only the flat solution exists. It is observed that these lines tend to the analytical values $\kappa_t^{(0)}$ and $\kappa_M^{(0)}$, marked with points, which we obtained in the low temperature limit in Sec. 2.3.2. This is consistent with the qualitative picture that we put forward before for the phase diagram; we have labelled the different zones of the density plot for the magnetisation with (I,II,IIIa,IIIb), analogously to what was done in Fig. 2.5. On the one hand, note that in zone II we have that $\Delta F < 0$, since it is the phase B+ is the only stable solution. On the other hand, in zone III we have that $\Delta F < 0$ between the bifurcation line and the coexistence line, that is, in region IIIa where the phase B+ gives the absolute minimum of the free energy, whereas $\Delta F < 0$ in region IIIb where the phase B+ is only metastable.

Second, we consider the buckled phase B-, which is always unstable and only exists in region III, that is, $\kappa_b(\theta) \leq \kappa \leq \kappa_M(\theta)$. This phase is found in region III by choosing an initial value of the shooting slope $u'(0)$ equal to that over the low temperature solution for the considered value of κ. In regions I and II, this initial slope leads to the flat solution.

Analogously to what was done in Fig. 2.6 for the stable phase B+, we present density plots for the numerical estimates for the magnetisation order parameter M (top panel) and the free energy difference ΔF (bottom panel) as functions of (κ, θ) for the unstable phase B- in Fig. 2.7. We have that $\Delta F > 0$ everywhere in zone III, consistently with the phase B- being always unstable.

In Fig. 2.8, 3-dimensional plots of the magnetisation vs (θ,κ) together with sections for different values of θ are displayed. The magnetisation surface comprises two sheets: (i) the upper sheet, with larger values of M, which corresponds to the stable phase B+, whereas (ii) the lower sheet, with smaller values of M, which corresponds to the unstable phase B-. Both sheets coalesce at the first-order line $\kappa_M(\theta)$, beyond which $M = 0$ (flat phase L) is

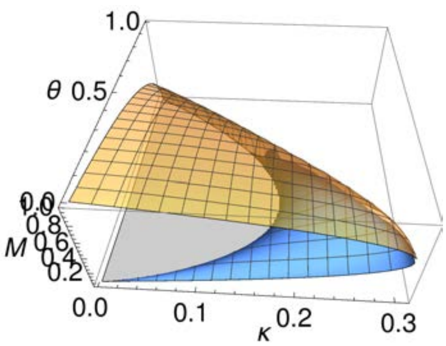

(a)

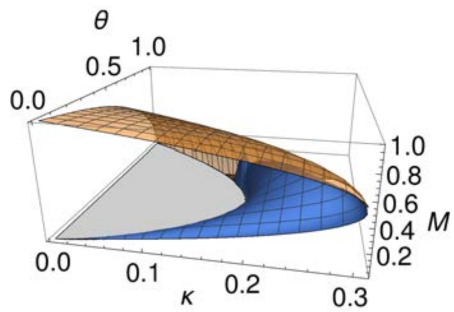

(b)

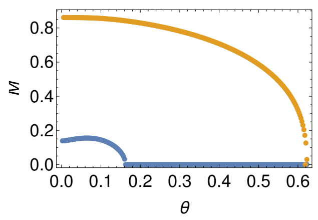

(c) $\kappa = 0.15$

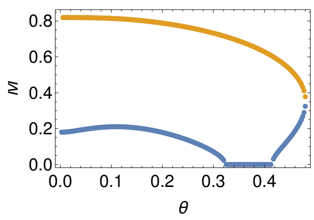

(d) $\kappa = 0.18$

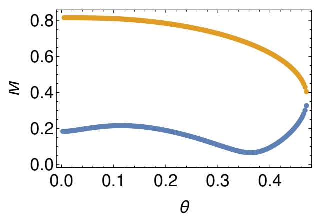

(e) $\kappa = 0.185$

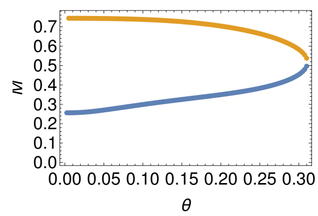

(f) $\kappa = 0.24$

Figure 2.8: Plots depicting the phase diagram of the system, numerically computed from eq. (2.11). Figures 2.8(a) and 2.8(b) show two different views of a 3D plot where the total magnetization of the buckled solutions are plotted versus κ and θ. The upper orange (lower blue) surface stands for the stable (unstable) solution, two different profiles of such solutions at low temperatures can be found in figure 2.2. Different sections for constant κ can be found in figures (c)-(f), where subcritical and supercritical bifurcations are present. Figure (c) shows a subcritical (suprecritical) bifurcation for low (high) temperatures. In figure (d), $\kappa > \kappa_c \sim 0.16$, the lower unstable solution (B-) starts to bifurcate from θ_2, creating the subcritical bifurcation depicted in blue at high temperatures. For $\kappa > \kappa_n$ (figure (e)) an isola stems from the $M = 0$ plane, B- is no longer bifurcating from the flat solution for $\kappa > \kappa_n \sim 0.184$. The isola disappears for $\kappa \sim 0.3$, see figures (a) and (b)

the only solution. It is clearly observed how the lower sheet continuously stems from $M = 0$ at the bifurcation line where it exists, that is, for temperatures smaller than θ_c, whereas the upper sheet only stems from $M = 0$ for temperatures larger than θ_c. Sections for different values of θ show in more detail how the stable (orange) and unstable (blue) solutions separate from the plane $M = 0$ for several values of κ. They produce an isola that disappears for $\kappa > \kappa_M$, leaving only the flat solution for bigger κ.

2.6 Conclusions

Despite its simplicity, the 1d string model contains the key ingredients that lead to the emergence of wrinkled and buckled phases in graphene. The transversal displacements u_i are coupled to some internal degrees of freedom, modelled in the simplest way by pseudo-spin variables σ_i that have two competing interactions: (i) first, an on-site interaction with its corresponding displacement and (ii) an antiferromagnetic interaction between nearest neighbour pseudo-spins, the strength of which is measured by κ. On the one hand, the interaction between the pseudo-spins and the elastic degrees of freedom entails that the string curvature is controlled by the local magnetisation. As the temperature θ is lowered for not too large values of κ, this brings about the existence of non-flat (buckled) profiles with non-zero global magnetisation. On the other hand, for low enough temperatures, the frustration arising from the short-ranged antiferromagnetic interaction (i) modifies the buckled phase, introducing an antiferromagnetic region close to the boundaries and (ii) makes the flat string become metastable.

A key element in the observed behaviour is the existence of a tricritical point K, at which all the observed phases coalesce. From it, three lines emanate that control the different phases: the bifurcation line $\kappa_b(\theta)$, the coexistence line $\kappa_t(\theta)$ and the first-order line $\kappa_M(\theta)$, $\kappa_b(\theta) < \kappa_t(\theta) < \kappa_M(\theta)$, as shown in Figs. 2.5 and 2.6. We have obtained the exact expression for $\kappa_b(\theta)$ and approximate analytical expressions for both $\kappa_t(\theta)$ and $\kappa_M(\theta)$ in the vicinity of the critical point. The extension of these expressions far from the critical point gives a better account of the coexistence line $\kappa_t(\theta)$ than of the first-order-line $\kappa_M(\theta)$, as seen in Fig. 2.6. This is quite logical, since they are calculated by using a Landau-like expansion of the free energy around the flat solution.

Beyond the first-order line (region I), $\kappa > \kappa_M(\theta)$, only the flat phase L is stable. Inside the bifurcation line $\kappa < \kappa_b(\theta)$ (region II), there only stable phase is the buckled one B+. The situation is more complex and thus interesting in the intermediate region III, $\kappa_b(\theta) < \kappa < \kappa_M(\theta)$. We may understand this region as the zone, for each value of the temperature θ, in which there is an actual competition between the ferromagnetic interaction that induces global buckling and the antiferromagnetic interaction that favours the flat phase.

There are three phases in region III: two buckled phases B+ and B-, with the maximum value of $u(x)$ being larger in the locally stable phase B+ than in the unstable phase B-, and the also locally stable flat phase L. The two locally stable phases B+ and L coexist at the line $\kappa_t(\theta)$, over which their respective free energy minima are equally deep. The buckled phase B+ is the most stable state (absolute minimum of the free energy) and the flat phase L is metastable for $\kappa_b(\theta) < \kappa < \kappa_t(\theta)$, that is, when the antiferromagnetic interaction is strong enough to stabilise the flat phase but not too strong. The situation is inverted for $\kappa_t(\theta) < \kappa < \kappa_M(\theta)$, that is, when the antiferromagnetic interaction is capable of further favouring the flat phase with respect to the buckled phase B+. In the spirit of Kramers theory [72], the unstable phase B- can be seen as providing a free energy barrier that the system has to overcome to move from one free energy minimum to the other.

The above phase diagram is qualitatively similar to that found numerically in a $2d$ version of the model, built on a hexagonal lattice to mimic buckling and rippling in graphene [124]. It is the qualitative shape of this phase diagram that explains the emergence of the rippled to buckled transition when the system is heated, recently observed in STM experiments [130]. The key point is the existence of a region of values of the antiferromagnetic parameter κ, inside which the flat phase is locally stable for low enough temperatures but becomes unstable and is *replaced* by a buckled phase when the temperature is increased. This is the region to the left of the turning point (nose) of the bifurcation line, that is, $\kappa < \kappa_{\mathrm{n}}$. For a low enough initial value of the temperature, the string may be prepared in a rippled, flat, profile because it is a metastable equilibrium state at low temperatures. Then, as the temperature is slowly increased, the string suddenly jumps to a buckled state just as the temperature crosses the bifurcation line, and remains buckled.

In light of the above discussion, it is tempting to conjecture that the actual phase diagram of graphene is similar to the one found here. The crux is the existence of some internal degrees of freedom, for which (i) the direct short-ranged interaction among themselves, whose intensity is measured by a parameter κ, favours rippling but (ii) their coupling with the elastic modes give rise to a long-ranged interaction that favours buckling. It is this competition that leads to a phase diagram like ours, in which there appears a bifurcation line $\kappa_b(\theta)$ below some value of the temperature. The unit of temperature is chosen as the transition temperature when there is no antiferromagnetic coupling, that is, $\kappa_b(\theta = 1) = 0$. If the competition between the direct short-ranged and the induced long-ranged interaction leads to $\kappa_b(\theta = 0^+) \to 0$ for low temperatures, a maximum or nose in the curve $\kappa_b(\theta)$ would emerge, leading to the STM-like rippled to buckled transition described in the previous paragraph.

Chapter 3

Rippling in a spin-membrane model on a hexagonal lattice

3.1 Introduction

There have been many studies of graphene ripples. The earliest studies using Monte Carlo [50] or molecular dynamics simulations [3] have shown that ripples may be connected to variable length σ bonds of carbon atoms and may be caused by thermal fluctuations. Other studies have explored the connection between rippling and electron-phonon coupling [59, 83]. In particular, it has been suggested that, at zero temperature, the electron-phonon coupling may drive the graphene sheet into a quantum critical point characterized by the vanishing of the bending rigidity of the membrane [127]. The continuation of this work by J. Gonzalez [66] discusses the nonzero expectation value of the mean curvature (the Laplacian of the flexural phonon field) once the bending rigidity of the membrane vanishes, and its role as order parameter. Alternatively, assuming that the graphene membrane is fluctuating in $2 + d$ dimensions (with $d \gg 1$), Guinea *et al.* have calculated the dressed two-particle propagators of the elastic and electron interactions. They have found a collective mode which becomes unstable at a nonzero wave vector and causes the appearance of Gaussian curvature [70]. Amorim et al. [9] estimate the crossover temperature between quantum and classical descriptions to be 70-90 K. Thus a quantum description of ripples is not necessary at room temperature. All these studies investigate and characterize rippling as equilibrium phenomena.

We are interested in rippling dynamics and stability of static corrugations under disturbances. In experiments to visualize ripples using a transmission electron microscope (TEM), the suspended graphene sheet is hit by a low-intensity electron beam that may push atoms out-of-plane upward or downward in a random fashion. An alternative technique to visualize ripples is using a scanning tunneling microscope (STM)[147]. In this case, the graphene sheet is pushed and locally heated in the region close to the tip. Depending on the tunneling current and the voltage between tip and sheet, the latter may undergo a phase transition from a flexible (rippled) to a rigid (buckled) state [130].

In Ref. [110], the authors simplify the distortion of the 2d crystal by modeling it with two-state spin-like variables ($+1$ upward, -1 downward). There are antiferromagnetic interactions among these spins, because the out-of-plane shift of the atoms in opposite directions stabilize the strictly 2d system while keeping the gapless band structure of graphene [110]. A rich phase diagram is found, including paramagnetic, ordered and glassy phases, depending on the temperature and the values of the nearest-neighbor and next-nearest-neighbor couplings. In this way, they describe the formation and origin of the atomic scale rippling found in Ref. [97]. On the other hand, there are also models that investigate rippling by considering at each lattice site a continuous variable u describing the out-of-plane displacement of the carbon atom coupled to a spin variable ($\sigma = \pm 1$) representing an internal degree of freedom [23, 25]. This may be understood as a mechanical system coupled to a spin system. The spin at each lattice site represents the non-saturated fourth bond that, by a physical mechanism similar to the one discussed in [110], tries to pull the corresponding atom upward ($u > 0$) or downward ($u < 0$) from the flat sheet configuration. Mathematically, this is done by introducing a linear coupling term in the system energy, proportional to $-u\sigma$ for each lattice site. In these simple models, the mechanical system is either a chain of oscillators [25] or a discrete elasticity model of the hexagonal graphene lattice [23], while the spins are in contact with a thermal bath and flip randomly according to Glauber dynamics at the temperature T of the thermal bath. In both models, the system forms metastable but long-lived ripples assuming slow spin relaxation [23, 25].

It is worth investigating a combination of the two approaches described in the previous paragraph. Firstly, it seems sensible to model the out-of-plane displacement at each lattice site by a continuous variable as in Refs. [23, 25], which is driven by the internal degree of freedom represented by the spin. Secondly, these spins certainly interact among themselves, by the mechanism proposed in [110]. Thus, in this paper we discuss the formation and dynamics of ripples in graphene through a system of atoms connected by harmonic springs and coupled to interacting Ising spins. We start from the spin-oscillator chain model [23, 25, 113] and add interactions among spins that produce stable rippling states. There appear different phases and transitions between them depending on parameter values.

The plan of this chapter is as follows. Section 3.2 is devoted to the expansion of the model to 2 dimensions on a hexagonal lattice, with first and second-neighbors interactions between spins. Besides, we carry out a systematic analysis of the system modifying the parameters and studying the stationary configuration after the transitory, using a phase diagram in Section 3.2.1, and describing the different phenomenology of each phase in Section 3.2.2. The main conclusions are presented in Sec. 3.4. Relevant information that is not covered in the main text is presented in the Appendices: some geometrical expressions for the hexagonal lattice are discussed in B.1, while images of the different phases are collected in 3.3.

3.2 The two-dimensional model

Here, we extend the one-dimensional model from chapter 2 to dimension $d = 2$, in the hope that this will make it possible to find more complex behaviors. This extension is almost direct and, as we are interested in applying the model to mimic a graphene sheet, we consider a hexagonal lattice. Due to the symmetry, it is important to write the hamiltonian carefully. First, each atom is indexed: i will be the row index and j the column index, with the peculiarity that each row comprises atoms with two different heights in a zigzag distribution, see Figure 3.1. It is important to note that the form of the equations will be qualitatively different for atoms for which $|i - j|$ is an even number *(e-atoms)*, which have one nearest neighbor above and two below, and those for which $|i - j|$ is an odd number *(o-atoms)*, which have one nearest neighbor below and two above, that is, the opposite situation. It is quite obvious that if the plane is rotated by an angle of π, the two types of atoms are interchanged.

Taking into account the notation described in chapter 2, we can write down the extension of the $1d$ Hamiltonian to $d = 2$. Moreover, we introduce

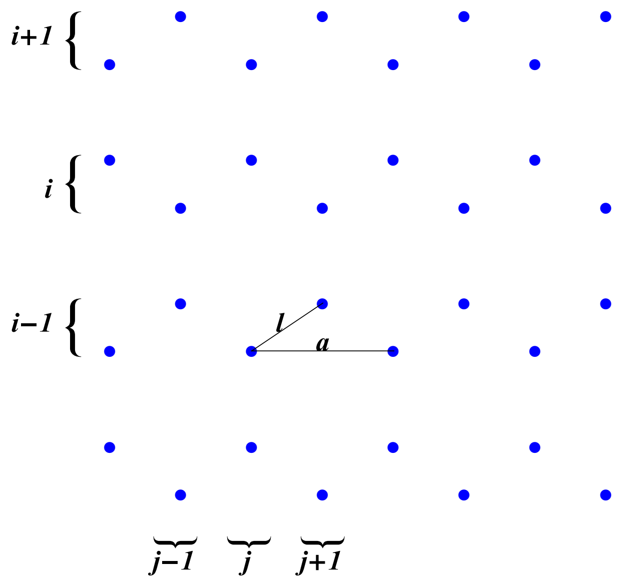

Figure 3.1: Figure summarizing the atoms indexes and the parameters of the unit cell of the hexagonal lattice.

next-nearest-neighbor interactions,

$$\begin{aligned}\mathcal{H} &= \sum_{ij}\left[\frac{p_{ij}^2}{2m} - f u_{ij}\sigma_{ij} + J'\sigma_{ij}(\sigma_{i-1,j-1} + \sigma_{i,j-2} + \sigma_{i+1,j-1})\right] \\ &+ \sum_{|i-j|=\text{even}}\left\{\frac{k}{2}\left[(u_{ij}-u_{i+1,j})^2 + (u_{ij}-u_{i,j-1})^2 + (u_{ij}-u_{i,j+1})^2\right]\right. \\ &\qquad\left. + J\sigma_{ij}(\sigma_{i+1,j} + \sigma_{i,j-1} + \sigma_{i,j+1})\right\}, \end{aligned} \tag{3.1}$$

where i and j take values $1 \to i_{\max}$ and $1 \to j_{\max}$, respectively. Following the same steps as in the previous section, the nondimensional equation of motion for each atom and the expressions for the transition rate become

$$\ddot{u}_{ij} - K_N^2(u_{i+1,j} + u_{i,j-1} + u_{i,j+1} - 3u_{ij}) = \sigma_{ij}, \tag{3.2}$$

$$\omega_{ij}(\boldsymbol{\sigma}|\boldsymbol{u}) = \frac{\delta}{2}(1 - \gamma_{ij}\sigma_{ij}), \tag{3.3}$$

$$\gamma_{ij} = \tanh[\frac{u_{ij}}{\theta} - \frac{\kappa}{\theta}(\sigma_{i+1,j} + \sigma_{i,j+1} + \sigma_{i,j-1}) - \frac{\lambda}{\theta}(\sigma_{i,j-2} + \sigma_{i,j+2} + \sigma_{i-1,j-1} + \sigma_{i-1,j+1} + \sigma_{i+1,j-1} + \sigma_{i+1,j+1})], \tag{3.4}$$

where K_N is a large scale parameter to be calculated later. As we said before, the difference between e-atoms with o-atoms follows from the rotation by π of the plane. For that reason, only equations for e-atoms have been written. In the latter equations, the height variable u and time are dimensionless. In the nondimensionalization, the same parameters as in equations (2.6) and (2.7) appear, with the addition of $\lambda = J'/T_0$, which corresponds to the new next-nearest-neighbor interaction.

The length of each side of the finite hexagonal lattice is $\tilde{L} = [3(n-1)+1]\tilde{l}/2$, where $\tilde{l}$ is the side of a unit hexagonal cell and n is the maximum value of the row index i in Fig. 3.1. Let us measure all lengths in units of $\tilde{L}$, so that $l = \tilde{l}/\tilde{L}$ tends to zero as the hexagonal lattice fills the plane. Then the expression within parenthesis in (3.2) has the limit [22, 25, 39]

$$u_{i+1,j} + u_{i,j-1} + u_{i,j+1} - 3u_{ij} \to \frac{a^2}{4}(\partial_x^2 u + \partial_y^2 u), \tag{3.5}$$

as $a = \sqrt{3}l \to 0$. Therefore, we take K_N proportional to a^{-1}, namely

$$K_N = \frac{\sqrt{2}}{\pi}a^{-1} = \frac{3n-2}{\sqrt{6}\pi} \propto n, \tag{3.6}$$

to guarantee that the diffusive term in (3.2) remains finite as $l \to 0$ (continuum limit). Note that the increments of the continuous variables are $\Delta x(i \to i+1) = 3l/2$ and $\Delta y(j \to j+1) = a/2 = \sqrt{3}l/2$, as seen in Fig. 3.1, so that the hexagonal lattice goes to the unit square $0 \leq x, y \leq 1$ in the continuum limit. For details, see B.1.

Once the system reaches the stationary state, equation (3.2) can be averaged ignoring thermal fluctuations. Thus, using equation (3.5) for $n \gg 1$ we get

$$\frac{1}{2\pi^2}\nabla^2\langle u\rangle = -\langle\sigma\rangle, \tag{3.7}$$

where $\langle u\rangle$ and $\langle\sigma\rangle$ are the average height and spin at the point (x, y) of the unit square. This equation is completely equivalent to its 1-D counterpart, equation (2.9). For $\kappa = \lambda = 0$, we have that $\langle\sigma\rangle = \tanh(u/\theta)$ and the flat configuration $\langle u\rangle = 0$ becomes unstable at $\theta = 1$, similarly to the situation in the 1d case. This kind of rigidly buckled configurations have been observed in graphene in recent STM experiments [130]. Equation (3.7) tells us that there is a correspondence between lattice patterns given by the average height profile and the spin configuration. Specifically, the curvature of the rippling is directly proportional to the average spin. Therefore, in the following section we will mainly characterize the phases by the spin configuration.

3.2.1 Phase diagram

As it has already been said, the stable steady state is a rigidly buckled configuration below the critical temperature ($\theta < 1$), provided there is no interaction between spins. We expect that the introduction of the nearest neighbour interaction among the spins should introduce new phases. By analogy with the 1d system, an antiferromagnetic nearest neighbour interaction should make antiferromagnetic ordered phases to appear for low enough temperatures. Looking for a more complex phenomenology, we introduce a next-nearest-neighbor interaction, as in Ref. [110]. This term appears in (3.1) through J' and in (3.4) through its dimensionless counterpart λ.

It is important to note that both J (κ) and J' (λ) may take positive or negative values, corresponding to antiferromagnetic and ferromagnetic interactions, respectively. However, only positive values of λ will be considered, since a next-nearest-neighbor ferromagnetic interaction just strengthens the nearest-neighbor one [1]. For positive values of κ and λ the qualitative behavior is quite different. The nearest-neighbor interaction provides a defined minimum energy distribution in which each spin and its nearest-neighbors point in opposite directions. However, the next-nearest-neighbor interaction does not yield a defined minimum energy distribution. In fact, the second-neighbors of each atom are second-neighbors to each other, and therefore the next-nearest-neighbor interaction causes the system to be frustrated [110]. An enlightening discussion about frustration is given in the introduction of [100]. In principle, it is tempting to exclude negative values of κ from the analysis. On intuitive grounds, one may conclude that the nearest-neighbour ferromagnetic coupling with $\kappa < 0$ should only strengthen the already long-ranged ferromagnetic interaction among the spins induced by the spin-lattice coupling term $-f u_{ij}\sigma_{ij}$ [25]. Nevertheless, the situation is a little bit more complex, as discussed below.

We plot a phase diagram to show in only one graph all the different behaviors, see Figure 3.2. In our simulations, we have chosen a nondimensional temperature $\theta = 0.01$, which is far below critical for $\kappa = \lambda = 0$. A key

[1] For both ferromagnetic and antiferromagnetic ordering, the next-nearest-neighbors of a given spin are parallel to it.

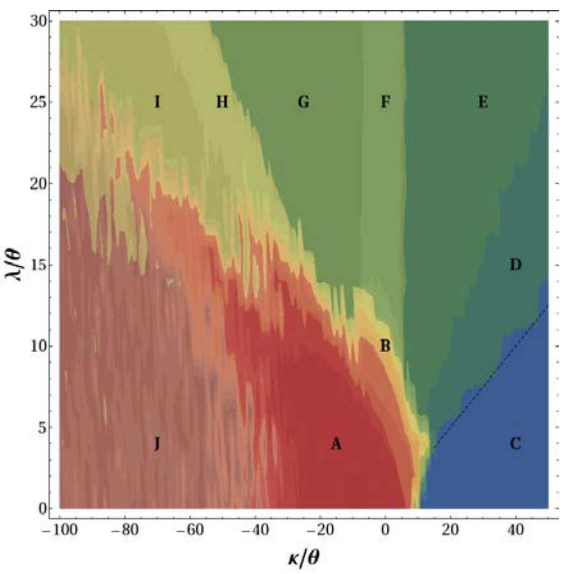

Figure 3.2: Phase diagram for a hexagonal lattice coupled to Ising spins. Different regions have been delimited using the domain-wall parameter, the magnetization and the specific heat. Once the equilibrium state is reached, each region has a different behavior, which is explained in the text. Also plotted is the line $\kappa/\lambda = 4$, which is a good estimate for the transition line between zones C and D. This agrees with the line separating phases Ordered 1 and 2 in Ref. [110].

parameter is

$$\mathcal{DL} = \frac{1}{N} \sum_{|i-j|=even} [3 + \sigma_{ij}(\sigma_{i+1,j} + \sigma_{i,j-1} + \sigma_{i,j+1})], \tag{3.8}$$

where N denotes the number of atoms in the lattice. This parameter estimates the domain-wall length [110], and it is equal to 3 (resp. 0) for completely ferromagnetic (resp. antiferromagnetic) behavior. Analogous to the 1-D version, equation (2.14). In addition, to delimit the regions on the diagram, we have used the absolute value of the usual magnetization

$$M = \left| \frac{1}{N} \sum_{ij} \sigma_{ij} \right|, \tag{3.9}$$

and energy fluctuations (proportional to the specific heat),

$$F = \sqrt{\langle (\Delta^* e)^2 \rangle}. \tag{3.10}$$

Here e is the system energy and $\Delta^* e = (e - \langle e \rangle)$, where the angular brackets stands for the mean value that is calculated once the stationary state has been reached.

3.2.2 Region characterization

The different regions in the phase diagram have been characterized using the three parameters $\mathcal{DL}$, M and F. Figure 3.2 is the superposition of the projections of M and $\mathcal{DL}$ on the plane $\lambda/\theta - \kappa/\theta$. Each region of the plane correspond to different combinations of M and $\mathcal{DL}$ values. Once the regions have been delimited using the magnitudes described above, the system is allowed to evolve with κ and λ in one of the regions. Next, we verify that the system reaches the equilibrium state and we obtain the basic structures in the spin domains. Moreover, to check that we have actually reached the equilibrium state, another simulation is carried out with this distribution as the initial condition: if, aside from thermal fluctuations, no evolution is found, equilibrium has been reached.

- Region A. $\mathcal{DL} \sim 3$, $M \sim 1$. The plane is completely curved, and the spins are all pointing in the same direction. This situation corresponds to small values of κ and λ, for which the interaction that dominates is the one between the surface and the spins, in agreement with the simple picture already present in the $1d$ model, see chapter 2.

- Region B. It is the zone surrounding A, on which $\mathcal{DL}$ and M decrease from the A values to those on the other regions. Here, the system displays a behavior that is analogous to the one described in chapter 2 (in $1d$). The interaction between the surface and the spins is an effective ferromagnetic interaction with an intensity that decreases from the center to the border. Thus, the plane is buckled but the spins close to the border are antiferromagnetically arranged.

- Region C. $\mathcal{DL} \sim 0.5$, $M \sim 0$. The predominant interaction is the antiferromagnetic first-neighbor one. The equilibrium state (starting from a random initial spin distribution) is composed of antiferromagnetic domains.

- Region D. $\mathcal{DL}$ increases from 0.5 to 1.2, $M \sim 0$. The states in this region are metastable. Taking the distribution corresponding to the equilibrium state of C or E as the initial condition, the system does not evolve to the other state, at least in a simulation time much greater than the relaxation time from random initial conditions.

- Region E. $\mathcal{DL} \sim 1.2$, $M \sim 0$. In this case, the spins are distributed in rows of two atoms in the lowest energy configuration. Beginning with random initial conditions, these two-atoms domains were created, with the rows in any of the three symmetrical directions.

- Region F. $\mathcal{DL} \sim 1.5$, $M \sim 0.2$. The interaction between the plane and the spins is relevant again, since the antiferromagnetic next-nearest-neighbor interaction (with $\kappa \sim 0$) has no defined minimum energy distribution. The plane is curved, leading to a non-zero magnetization.

- Region G. $\mathcal{DL} \sim 1.8$, $M \sim 0$. The typical equilibrium configurations are long serpentine lines, with zero magnetization. Taking as initial conditions the spins arranged in rows, the system remains static.

- Regions H and I. In them, the system evolves from the characteristic configurations of G to the ferromagnetic configurations of J, with the difference that in H the magnetization is different from zero whereas in I it is not. I is a ferromagnetic first-neighbor state, but with domains smaller than in J ($\mathcal{DL}$ smaller than in J).

- Region J. $\mathcal{DL} \sim 2.5$, $M \sim 0.1$. In this case the system behaves as a completely ferromagnetic first-neighbor system. Starting from random initial conditions, ferromagnetic domains grow until reaching a stationary state. In this case M is close to zero since spins are pointing to different directions in adjoining domains.

The plots of the typical equilibrium configurations for each region are in section 3.3.

It should be noted that our phase diagram does not contain a paramagnetic state because the chosen temperature, $\theta = 0.01$, is far below the critical temperature for $\kappa = 0$ and $\lambda = 0$ (unity in our dimensionless variables). Each point of the phase diagram corresponds to the energy minimum to which the system evolves for the considered parameters. Once it is in the neighborhood of this minimum, the energy barriers are so high that ergodicity is no longer valid, and the system remains *frozen* [138]. This causes an Edwards-Anderson order parameter [46],

$$q_{EA} \equiv \frac{1}{N} \sum_{ij} \mu_{ij}^2, \quad \mu_{ij} \equiv \langle \sigma_{ij} \rangle, \tag{3.11}$$

to be different from zero at every point of the plotted phase diagram. On the other hand, close to $\kappa = \lambda = 0$, the order parameter q_{EA} will vanish as $\theta \to \infty$, once ergodicity is recovered. In Eq. (3.11) the average should be understood as a time average or an extended Gibbs average in a phase space composed of disjoint ergodic components [138].

3.3 Phase diagram images

In our simulations, we have used a lattice of 2,150 atoms and a temperature $\theta = 0.01$. We need to impose initial and boundary conditions for the membrane and the spins. Initially, the spins are in a completely random configuration, whereas the membrane is flat and at rest. The membrane is clamped (zero displacement) at the boundaries. As nearest and next-nearest neighbors determine the dynamics of a given spin, see eq. (3.4), a spin located next to the boundary condition needs data from nearby spins located at the boundaries and also outside the lattice. The simplest possibility is that the spins of clamped boundary atoms and their nearest neighbors outside the lattice do not interact with the others, which can be achieved by formally assigning spin zero to them.

3.4 Conclusions

We have studied a system of atoms connected by harmonic springs and coupled to Glauber spins. The spins are in contact with a thermal bath and interact with their neighbors. The $1d$ system forms one ripple and becomes antiferromagnetic at the boundaries as ρ increases, until it becomes completely antiferromagnetic. When the system is on a $2d$ hexagonal lattice, each spin interacts with its nearest-neighbors and next-nearest-neighbors, aside from the coupling with the out-of-plane displacement. This situation generates different phases which are included in a phase diagram.

The range of parameters in our phase diagram includes negative values for the nearest neighbor coupling constant κ and is thus wider than the one used in [110], in which only antiferromagnetic interactions were considered. The change in the sign of the spin-spin interaction can be produced by the scattering of the conduction electrons at the spins, see [16, 122]. We are interested in zero magnetization phases since they correspond to no overall bending. Our model provides different phases obeying this constraint: I and J are long wave length phases, similar to those observed in [12, 99], whereas C, E and G are phases with atomic wave length. G is a stripy phase (see Figure 3.3), which could be associated with patterns seen in [97]. The atomic wave length phases C and E correspond with phases Ordered 1 and 2, respectively, from Ref. [110]. Therein, the line between these two phases is (in our variables) $\kappa/\lambda = 4$, which agrees with the limit of true stability of C here. Interestingly, neither the metastable phase D or the other phases (including the long wavelength phases I and J) were found in Ref. [110]. In that reference, (i) only positive values of κ were considered, and (ii) there was no spin-atom coupling.

The buckling phase A is surrounded by rippled phases C, E, and G with no overall bending. Starting from a point of the phase diagram belonging to region C (rippled phase), if we increase the temperature while keeping κ and λ (supposed temperature independent) fixed, we move along a straight line of slope λ/κ in Figure 3.2 from phase C to the buckled phase A. In experiments with STM at fixed current, the temperature is locally increased at the tip region and this triggers a transition from a rippled flexible phase to a rigid buckled phase [130]. Thus our model seems to contain the rippled-to-buckled transition observed in experiments, which is studied in more detail in chapter 4.

To conclude, our model is based in a few parameters controlling simple interactions which generate complex collective behaviors. This allows us to identify the interactions responsible for each pattern. In addition, the elastic feature of the model makes it possible to visualize and quantify the magnitude of the rippling, which could be compared with experiments once height measurements had been improved.

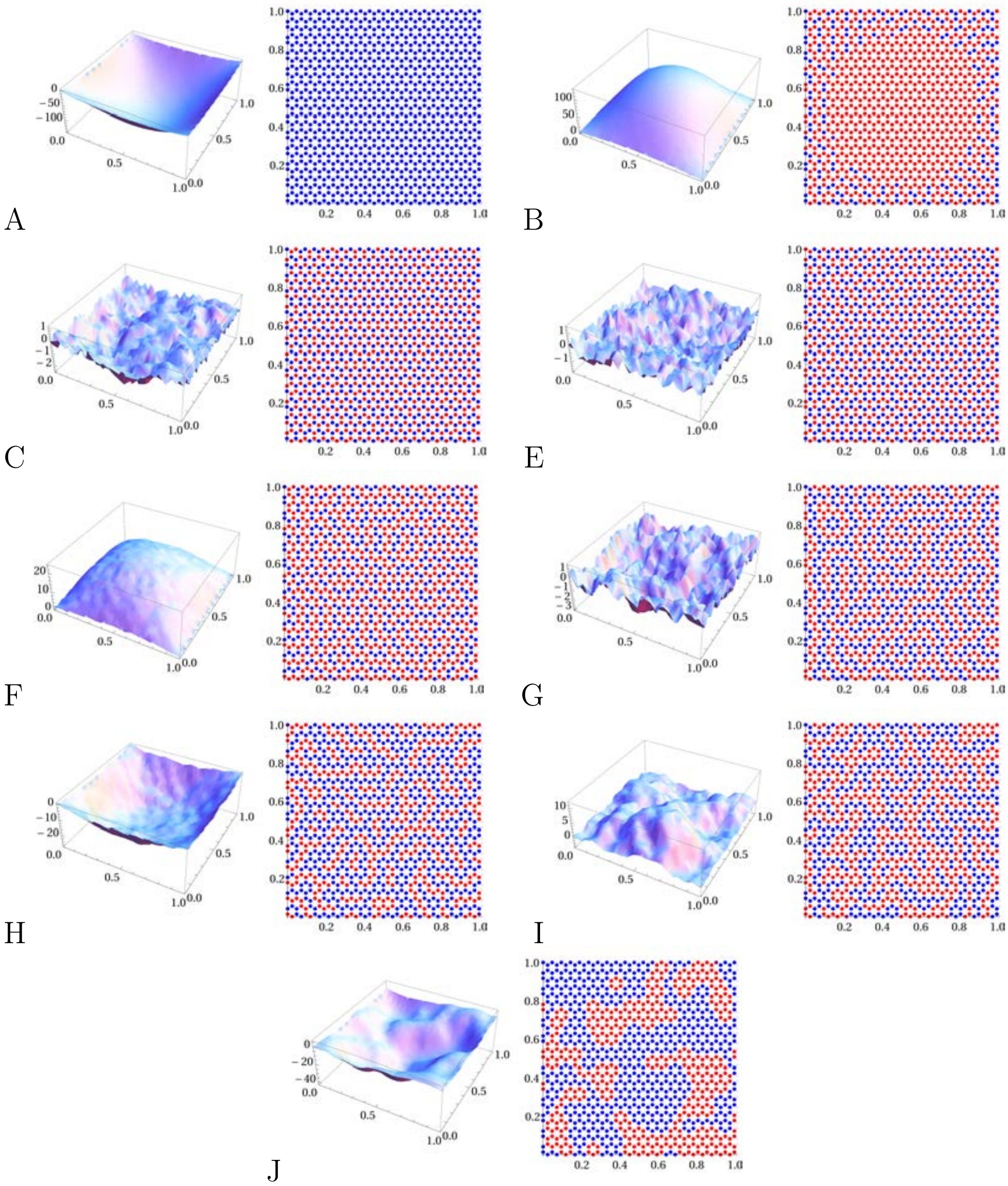

Figure 3.3: Final configuration of the plane and the spins (red for spin up and blue for spin down) for different values of κ and λ, corresponding to different regions of the phase diagram in Fig. 3.2. From top to bottom and left to right: Region A, $\kappa/\theta = -10$ and $\lambda/\theta = 2$, Region B, $\kappa/\theta = 0$ and $\lambda/\theta = 10$, Region C, $\kappa/\theta = 40$ and $\lambda/\theta = 3$, Region E, $\kappa/\theta = 40$ and $\lambda/\theta = 27$, Region F, $\kappa/\theta = 0$ and $\lambda/\theta = 24$, Region G, $\kappa/\theta = -25$ and $\lambda/\theta = 24$, Region H, $\kappa/\theta = -60$ and $\lambda/\theta = 30$, Region I, $\kappa/\theta = -73$ and $\lambda/\theta = 27$, Region J, $\kappa/\theta = -91$ and $\lambda/\theta = 3$.

Chapter 4

STM driven transition from rippled to buckled graphene in a spin-membrane model

4.1 Introduction

Buckling upon heating a graphene sample has been systematically investigated in ref. [130] by using scanning tunneling microscopy (STM). Specifically, the tip of the microscope is centered on a suspended sample that is initially flat on average although it is surely covered with ripples [99]. Application of a voltage bias V between the STM tip and the membrane has a twofold effect: (i) it induces a tunneling current that locally heats the sample, and (ii) it produces an electrostatic interaction between the tip and the sample. Experiments show that the suspended graphene sheet experiences a transition from "floppy" rippled-flat to "rigid" buckled state. The membrane height Z is plotted in Fig. 4.1 as a function of the voltage bias V for several values of the tunneling intensity I. On the one hand, for "small" values of I, the height $Z = Z(V)$ is a monotone increasing and continuous function of V. The membrane is rippled and its behavior is reversible: the same curve $Z(V)$ is observed whether the voltage bias increases from 0 to a certain value $V_{\max}$ or decreases from $V_{\max}$ to 0. On the other hand, once the current is kept constant at a high enough value, increasing the bias causes the sample to buckle irreversibly: once a sufficiently large value $V_{\max}$ is reached, the sample remains buckled as the bias is decreased back from $V_{\max}$ to zero.

Schoelz *et al* proposed a phenomenological Ising model to explain their experimental results [130]. In their model, each local spin σ_{ij} represents one ripple composed of $\sim$ 1000 carbon atoms and the value of the spin

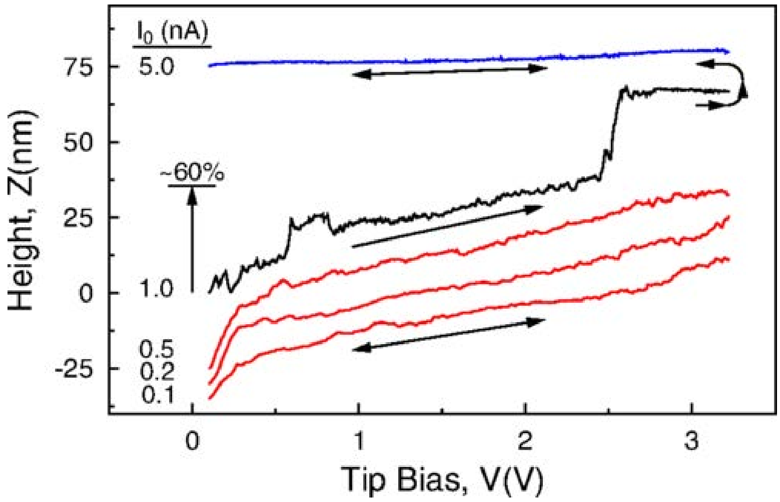

Figure 4.1: Height of the STM tip on the graphene sheet versus applied voltage for different values of the tunneling current. Curves are slightly offset from each other for clarity. From ref. [130].

indicates the curvature of the ripple. The energy of this Ising system has two contributions. Firstly, a nearest neighbor spin-spin interaction, with a coupling constant J that depends on the total magnetization $M = \sum_{ij} \sigma_{ij}$. The second contribution to the energy is an interaction of the spins with an external field $h = h_0 e^{-r/\xi}$, where h_0 is assimilated to the voltage bias in the experiment and r is the distance to the center of the sample, located just "below" the STM tip. The spin-spin interaction is antiferromagnetic ($J = -1$) for $0 < M < M_0$ and ferromagnetic ($J = 2$) for $M > M_0$, M_0 is 60%–70% of the maximum possible value of the magnetization. The correlation length ξ may also change discontinuously and, counterintuitively, the temperature decreases as the tunneling current increases [130]. The M versus h curve of this model is as follows [130]. At zero field, $M = 0$ and thus $J = -1$. As h_0 increases to $h_0^{\max} = 3$, the spin-spin interaction reverses suddenly to ferromagnetic ($J = 2$) at a field $h_0 \simeq 2.5$ for which M has reached M_0. This discontinuous increase in J at $h_0 = 2.5$ causes a sudden increase of the magnetization. Afterwards, when the external field is decreased back to 0, the coupling constant is left unchanged at $J = 2$ and therefore the spins never go back to the initial state. To further mimic experimental results, a smaller jump in the magnetization for $h_0 < 2.5$ is induced by an increase in the correlation length ξ; see Figure 3 in ref. [130].

In this chapter, we qualitatively explain Schoelz *et al*'s experimental findings [130] by using a spin-membrane model that exhibits ripples on a flat membrane, buckling and a dynamical transition from floppy to rigid states. Thus we do not need to: (i) interpret spins as many-atom ripples, (ii) introduce jumps in J and ξ with M, and (iii) decrease the temperature with increasing tunneling current, as done in ref. [130]. Our model includes coupling between out-of-plane elastic displacements of atoms and local pseudo-spins that pull atoms off plane. The pseudo-spins are coupled by nearest neighbor interactions. In chapter 3, we have analyzed a similar model under constant, low, temperature conditions, see also [123].

STM experiments occur under varying temperature conditions because of Joule heating due to the tunneling current. Increasing the temperature is akin to driving the system through a first-order phase transition, which is the essence of our explanation of Schoelz et al's experiments. Thus in the present work we include: (a) an external field that represents the STM voltage and, most importantly, (b) the (non-homogeneous) time-dependent temperature profile brought about by the STM heating of the sample. For different values of control parameters, first and second order phase transitions between a rippled-flat membrane state and a buckled state appear. In the parameter region where these phases coexist, it is possible to drive the system in conditions that mimic those in the experiment: inhomogeneous sample heating due to the tunneling current and electrostatic tip-sample interaction [130]. We then show that the wrinkled to buckled transition appears naturally in our model, without having to invoke ad-hoc jumps in the model parameters. Moreover, the spin-membrane model reproduces all the key experimental observations in the STM experiment, while providing a reasonable physical picture of the real system.

The plan of the chapter is as follows. The spin-membrane model in a hexagonal lattice is introduced in section 4.2. The different equilibrium phases are numerically characterized in section 4.3, in which we show that there is a first order phase transition between a flat but rippled membrane and a buckled one. In section 4.4, we drive the system through the first order phase transition in conditions similar to those in the experiments. A discussion of our results is presented in section 4.5.

4.2 The model on a hexagonal lattice

Here, we briefly recall our 2d model and its governing equations, which were more carefully presented in chapters 2 and 3.

Carbon atoms are placed on a hexagonal lattice as shown in Fig. 3.1. Let $(\sigma_{ij}, u_{ij}, p_{ij})$ be the values of the atom pseudo-spin, height and momentum, respectively, at site (i,j). The Hamiltonian is

$$\mathcal{H} = \sum_{ij}\left(\frac{p_{ij}^2}{2m} - f u_{ij}\sigma_{ij}\right) + \sum_{|i-j|=\text{even}}\left\{\frac{k}{2}\left[(u_{ij}-u_{i+1,j})^2 + (u_{ij}-u_{i,j-1})^2\right.\right.$$
$$\left.\left. + (u_{ij}-u_{i,j+1})^2\right] + J\sigma_{ij}(\sigma_{i+1,j}+\sigma_{i,j-1}+\sigma_{i,j+1})\right\}. \tag{4.1}$$

This is a particular case of the Hamiltonian introduced in equation (3.1) that had an additional next-nearest-neighbor interaction among spins.

The dynamics of the system consists of (i) Hamilton's equations of motion for (u_{ij}, p_{ij}), and (ii) Glauber dynamics [64] at temperature T for σ_{ij}:

$$\ddot{u}_{ij} - K_N^2(u_{i+1,j}+u_{i,j-1}+u_{i,j+1}-3u_{ij}) = \sigma_{ij}, \tag{4.2}$$
$$\omega_{ij}(\boldsymbol{\sigma}|\boldsymbol{u}) = \frac{\delta}{2}(1-\gamma_{ij}\sigma_{ij}), \tag{4.3}$$
$$\gamma_{ij} = \tanh\left[\frac{u_{ij}}{\theta} - \frac{\kappa}{\theta}(\sigma_{i+1,j}+\sigma_{i,j+1}+\sigma_{i,j-1})\right]. \tag{4.4}$$

Here ω_{ij} is the rate at which the pseudo-spin at site (i,j) flips and δ is a parameter setting the characteristic time-scale for the pseudo-spin flips. In the long time limit, the system reaches thermodynamic equilibrium and its probability distribution has the canonical form $\mathcal{P} \propto \exp(-\mathcal{H}/T)$. It is convenient to introduce the following parameters,

$$T_0 = \frac{f^2K_N^2}{k}, \quad K_N = \frac{3n-2}{\sqrt{6}\pi}, \tag{4.5}$$

where n is the total number of rows in the lattice. The temperature T_0 is the transition temperature from a (high temperature) flat to a buckled string configuration for $J=0$ [123]. Then, we define dimensionless displacements and time,

$$u_{ij}^* = \frac{k u_{ij}}{f K_N^2}, \qquad t^* = \frac{t}{K_N}\sqrt{\frac{k}{m}}, \tag{4.6}$$

and also dimensionless spin-spin coupling constant and temperature,

$$\kappa = \frac{J}{T_0}, \quad \theta = \frac{T}{T_0} = \frac{kT}{f^2K_N^2}. \tag{4.7}$$

Thus we measure energy in units of the transition temperature T_0.

In the equilibrium state, the average dimensionless displacements obey the discrete Poisson equation

$$-K_N^2(u_{i+1,j}+u_{i,j-1}+u_{i,j+1}-3u_{ij}) = \mu_{ij}, \tag{4.8}$$

in which μ_{ij} stands for the average magnetization at site (i,j). The asterisks have been omitted so as not to clutter the formulae. In the continuum limit, Eq. (4.8) becomes

$$\frac{1}{2\pi^2}\nabla^2 u(x,y) = \mu(x,y). \tag{4.9}$$

Here $0 \leq x, y \leq 1$, and the sample becomes the unit square in the continuum limit with our choice of dimensionless variables, see chapter 3 or [123] for more details. Therefore, the average magnetization gives the curvature of the membrane. Thus we can deduce the state of the membrane by looking at either the atoms displacements $u(x,y)$ or the pseudo-spins local value $\mu(x,y)$.

4.3 Equilibrium Phase Diagrams

Except for $J = 0$ that can be exactly solved, the equilibrium phase diagrams have to be calculated numerically. At $J = 0$, the flat solution bifurcates at $T = T_0$ to a buckled state, which is thermodynamically stable for $T < T_0$ [123]. This can be appreciated in Fig. 4.2, which has been drawn by down-sweeping the dimensionless temperature from a given $\theta > 1$ at each fixed value of κ. At the largest value of θ, the initial configuration is random and the simulation reaches equilibrium after a certain time. Then, the magnetization M and the domain length parameter $\mathcal{DL}$ of ref. [110],

$$M = \left| \frac{1}{N} \sum_{ij} \sigma_{ij} \right|, \tag{4.10}$$

$$\mathcal{DL} = \frac{1}{3N} \sum_{|i-j|=\text{even}} \left[3 + \sigma_{ij}\left(\sigma_{i+1,j} + \sigma_{i,j-1} + \sigma_{i,j+1}\right)\right], \tag{4.11}$$

are registered. For the next simulation, θ is slightly lowered and the equilibrium configuration reached at the previous temperature is used as the initial condition. This procedure is continued until the phase diagram is completed. Note that the parameter $\mathcal{DL}$ has an additional factor $1/3$, as compared to the one in chapter 3, so that $\mathcal{DL} = 1/2$ for random pseudo-spins and $\mathcal{DL} = 0$ for antiferromagnetic ordering. For ferromagnetic ordering, it is $M = \mathcal{DL} = 1$. Note that the magnetization (4.10) does not discriminate between the two possible signs of the curvature in Eq. (4.9).

The method we have just described produces the correct phase diagram provided the phase transitions are second order, which is the case for high critical temperatures ($\theta > 0.5$ as seen in Fig. 4.2). For first order phase transitions, down-sweeping yields only one part of the hysteresis loops associated

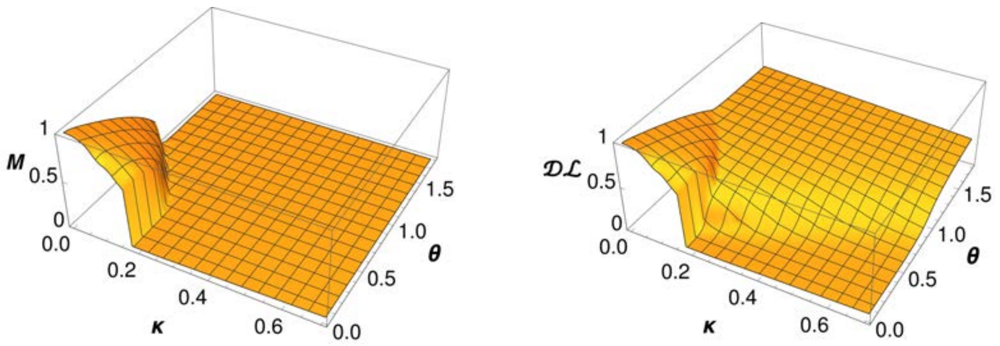

(a) Magnetization

(b) Domain Length

Figure 4.2: (a) Magnetization and (b) domain length parameter as functions of θ and κ obtained by temperature downsweeping as explained in the text.

with first order phase transitions, specifically that corresponding to the stable phase at the higher temperatures. To visualize the thermodynamically stable phase at first order phase transitions that occur for low critical temperatures, $\theta < 0.5$, we have redrawn the diagram always starting simulations from a random configuration and waiting for the system to equilibrate. This produces Fig. 4.3. On the one hand, we observe that there is a region of zero magnetization at low temperatures (approximately, $0.07 < \kappa < 0.2$) that was absent in Fig. 4.2. In this region, the membrane is rippled as shown by its partial antiferromagnetic ordering, $0 \leq \mathcal{DL} \leq 0.1$. On the other hand, the membrane ends up in low temperatures states that are similar to those in Fig. 4.2 both for $\kappa \lesssim 0.07$ (buckled membrane) and $\kappa \gtrsim 0.2$ (rippled flat membrane). These results are qualitatively equivalent to the phase diagram for the 1-d model described in chapter 2.

4.4 Driving graphene across the rippled to buckled phase transition

In Schoelz *et al*'s experiments [130], the floppy rippled membrane undergoes a transition to a rigid buckled state when heated by the STM current. In our model, this may correspond to driving the system across the low temperature first order phase transition seen in Fig. 4.3 for small values of κ and θ. To illustrate this, we set $\kappa = 0.1$ and $\theta = 0.01$ for all lattice points in our numerical simulations and start with an initially flat membrane and randomly oriented pseudo-spins. We consider $n = 35$ rows in a 2d hexagonal lattice, with $N = 2100$ atoms. The system reaches a stationary state, which is

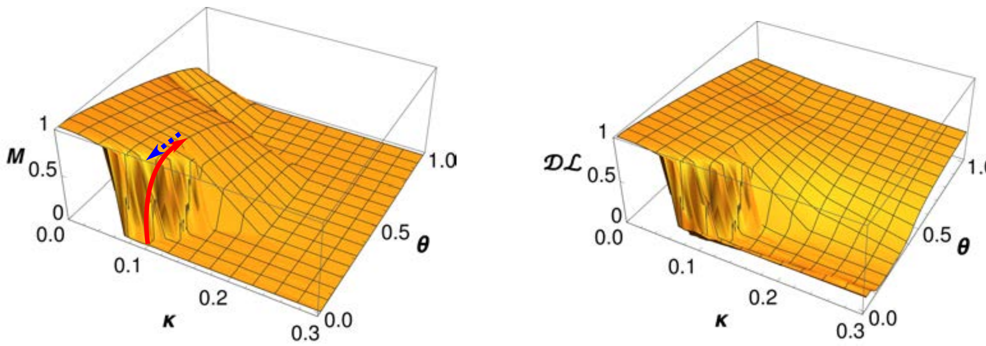

(a) Magnetization (b) Domain Length

Figure 4.3: (a) Magnetization and (b) domain length parameter as functions of θ and κ. The initial configuration for all the simulations consists of a flat membrane and randomly oriented pseudo-spins. In (a), we show a heating cycle corresponding to the interaction with a STM tip, see Sec. 4.4. The continuous red arrow represents the part of the cycle where the temperature is increased and the wrinkled to buckled phase transition occurs, whereas the dashed blue arrow marks the cooling part of the cycle where no transition is found since the system remains buckled.

typically rippled, $M = 0$ and $\mathcal{DL} \simeq 0.1 < 1/2$.

First, for the sake of simplicity and to understand the basic physical mechanism under the first order transition, we analyze *homogeneous heating* of the membrane. Second, in order to have a situation closer to the experiments and discuss some more specific details thereof, we consider the case of *inhomogeneous heating*.

4.4.1 Homogeneous heating

Assume that the heat bath temperature felt by the pseudo-spins is the same at all lattice points and varied at a constant rate. The pseudo-spins flip according to the Glauber dynamics given in (4.3) with the instantaneous and externally controlled value of the temperature $\theta(t)$.

Upon heating, the membrane remains rippled with zero magnetization for $\theta \lesssim 0.15$. At about $\theta_2 = 0.15$, the magnetization and the height of the central atom suddenly increase, as shown in Fig. 4.4. This effect strongly resembles the STM experiments in ref. [130], where the increase in dissipated power (modeled here with an increase of the temperature of the heat bath to which the system is coupled) promotes a discrete increase in height, that is, a buckling transition.

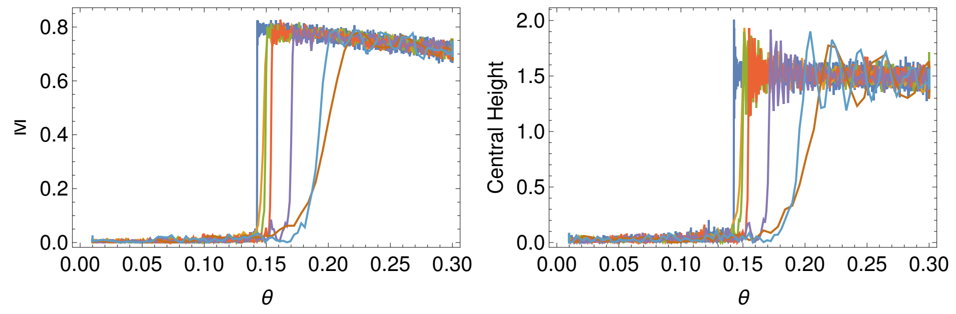

(a) Magnetization (b) Central Atom Height

Figure 4.4: Magnetization and height of the central atom as a function of temperature, upon heating of the system. Different lines correspond to different heating rates. Both the magnetization and the central atom height jump around $\theta_2 = 0.15$, revealing a first-order phase transition in the system. The slower the system is heated, the lower the temperature of the jump. In these simulations the initial and final temperatures are $\theta_0 = 0.01$ and $\theta_f = 0.3$, respectively. The system is heated with a constant rate, $\theta(t) = \theta_0 + rt$, and the different lines correspond to rates (from left to right): 3×10^{-5}, 3×10^{-4}, 4×10^{-4}, 6×10^{-4}, 10^{-3}, 3×10^{-3}, 6×10^{-3}.

The temperature at which the transition occurs depends on the heating rate. For the slowest rates, the jump is almost vertical and takes place at $\theta \simeq 0.15$. For faster rates, the transition is softer and happens for a slightly higher temperature, up to $\theta \simeq 0.20$ for the values considered in Fig. 4.4. The physical image is the following: a very slow, almost quasi-static, process leads to a sharp transition at the temperature at which the flat membrane becomes unstable. If heating is faster, the system remains in the unstable flat configuration for a certain time and is hindered from finding the "path" to the true thermodynamic equilibrium.

Finally, in Fig. 4.5, we present simulations in which the temperature is first increased, until the membrane buckles, and the system is subsequently cooled down to the initial low temperature. Interestingly, we observe that the system remains buckled when the temperature is lowered. This hysteretic behavior is a numerical proof of the metastability of the initial wrinkled configuration for low temperatures and thus is consistent with Fig. 4.2. The final state resembles the "rigid" states that are reached in STM experiments for large enough currents [130].

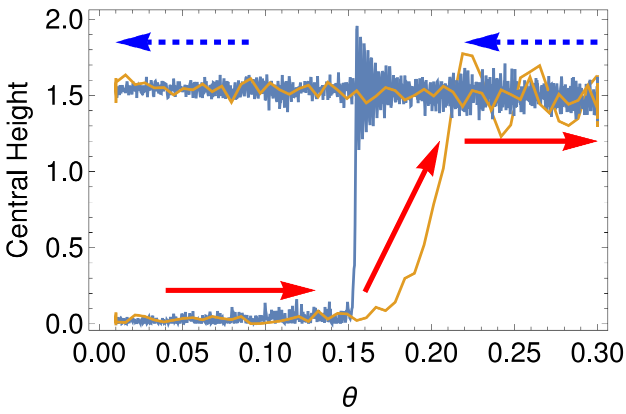

Figure 4.5: Height of the central atom as a function of the temperature for two heating/cooling cycles, the leftmost and rightmost lines correspond with the slowest and fastest rates of temperature variation in Fig. 4.4, respectively. The solid arrows and the dashed ones mark the heating and cooling part of the cycle respectively, analogously to the arrows present in Fig. 4.3. When cooled, the system remains buckled for $\theta < 0.15$, which shows that the flat rippled membrane configuration in the low temperature region is metastable.

4.4.2 Inhomogeneous heating

In STM experiments, the graphene sample is *locally* heated. We model this by an inhomogeneous temperature profile of a circular membrane of radius $R = 1/2$ (clamped at the boundary) inscribed in the unit square. Throughout this section, $\boldsymbol{r}$ stands for any point in the circle, $0 \le r \le R$, with $r = |\boldsymbol{r}|$. Energy is injected at the membrane center and the temperature is initially homogeneous throughout the sample, $\theta(\boldsymbol{r}, t = 0) = \theta_0$. At $t = 0$, the heating process starts, and the border of the sample is always kept at room temperature θ_0, $\theta(\boldsymbol{r}, t)|_{r=1/2} = \theta_0$.

The space and time temperature profile obeys the heat equation with a source term,

$$\partial_t \theta - \alpha \nabla^2 \theta = q(\boldsymbol{r}), \quad q(\boldsymbol{r}) = Q_0\, e^{-r^2/a^2}, \tag{4.12}$$

Note that we are using dimensionless variables, so that the thermal diffusivity α and the energy source from the STM tip q are measured in the units introduced in the previous sections (the dimensions of α and q are length^2/time and energy/time, respectively). The source term has radial symmetry and exhibits a Gaussian decay from its maximum value Q_0 over a characteristic length a (in dimensional units, a is a few angstroms [42]). Note that, for fixed values of a and α, the total injected power is proportional to Q_0. Therefore, we can consider that $Q_0 \propto IV$ in the STM experiments, where

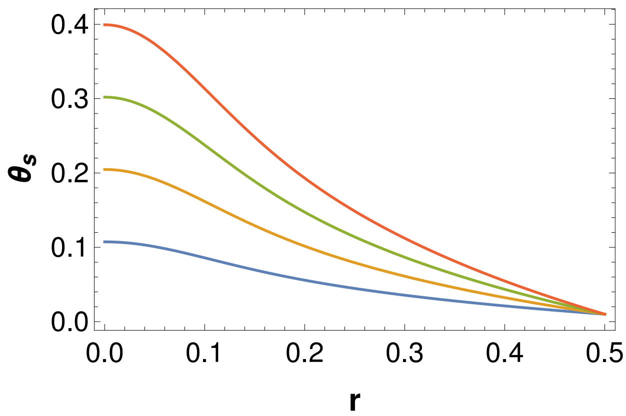

Figure 4.6: From bottom to top, steady temperature profiles for $\Delta\theta = 0.1$, 0.2, 0.3, 0.4.

I is the tunneling current and V the voltage bias between the tip and the sample. Interestingly, the same lateral decay of the injected power has been used in other experimental situations, see for instance ref. [51] for the study of the thermal conductivity of a graphene membrane excited by a laser.

We seek stationary solutions of the heat equation with radial symmetry, $\theta(r,t) = \theta_s(r)$, which obey

$$\nabla^2\theta_s + \frac{Q_0}{\alpha}\, e^{-r^2/a^2} = 0, \tag{4.13a}$$

$$\theta_s(r = R) = \theta_0, \quad \lim_{r\to 0} |\partial_r\theta_s(r)| < \infty. \tag{4.13b}$$

Equation (4.13) is solved along the same lines as in ref. [51], with the result

$$\theta_s(r) = \theta_0 + \frac{\Delta\theta}{2}\int_{r/a}^{R/a} dx\, \frac{1 - e^{-x^2}}{x}, \quad \Delta\theta = \frac{Q_0 a^2}{\alpha}. \tag{4.14}$$

We plot this stationary temperature profile for several values of $\Delta\theta$ in Fig. 4.6. We do not consider the transitory decay of the temperature profile to this steady solution, since graphene is a very good thermal conductor [51]. Thus, we expect the time scale for the decay to this steady profile to be much shorter than those associated to the increase or the decrease of the voltage bias in the STM experiments. In any case, we would like to stress that taking into account the transient to the stationary state does not alter our conclusions.

The STM tip also has an electrostatic interaction with the sample, which is included in our model by adding an external-field term $\Delta\mathcal{H}$ to the Hamiltonian (4.1),

$$\Delta\mathcal{H} = -\sum_{ij} h_{ij}\sigma_{ij}. \tag{4.15}$$

Note that the external field breaks the up-down symmetry of the pseudospins, which gives rise to a preferred sign of the curvature in Eq. (4.9). In ref. [130], the field h_{ij} decays exponentially from the center of the tip over a characteristic length of a few hundreds of the graphene lattice constant, which is consistent with the long-range character of the electrostatic interaction. In our work, we consider samples with 1650 atoms inside the circle of unit diameter. For such small samples, the field experiences almost no decay and, therefore, we simply take $h_{ij} = h$, independent of (i, j). Since the strength of the electrostatic interaction increases with the applied bias V, we identify h with V. Thus, the current is $I = \Delta\theta/V$ and the width of the source term, a, is three lattice constants in our simulations. For the sake of clarity, we sum up the key parameters of the model that control the behaviour showed in the simulations in Table 4.1.

Table 4.1: Main parameters controlling the behavior of the system in the inhomogeneous heating process, for an applied bias V and a tunneling current I spread over a region of characteristic length a, as expressed by Eqs. (4.12)-(4.15).

Parameter	Role	Controlling
κ	Pseudospins' anti-ferro interaction	Lower critical temperature θ_2, the system buckles for $\theta > \theta_2$.
$\Delta\theta \propto IVa^2$	Strength of the Joule effect	Temperature at the center of the sample: should be larger than θ_2 to induce buckling.
h	Strength of the tip-sample electrostatic interaction	Sign of the curvature (breaks up-down symmetry).

To mimic the experimental procedure in ref. [130], we fix I in each simulation, increase V at a certain constant rate and track the height of the central atom, see Fig. 4.7. In this way, we are driving the system in the parameter region where there is a first order phase transition as described in the previous section. Except for not having averaged the oscillations in our numerical results, the behavior displayed in Fig. 4.7 is completely analogous to that observed in ref. [130], see Fig. 4.1. For small I, the increase in V produces a reversible pulling that increases the global magnetization and the height of the central atom but does not produce overall buckling. Here, reversible means that if the voltage is decreased back to zero from its maximum value, the same curves are swept. This notwithstanding, once I reaches a certain critical value, *non-reversible* buckling appears (upper-curve): the membrane remains buckled when the voltage is decreased back to zero.

In the STM experiments, the buckling (when it occurs) comprises two steps: apart from the large jump in height at a certain value of the voltage V_c, there appears a smaller "bump" in height at a smaller voltage $V_1 < V_c$. Interestingly, even this fine detail of the experimental results is reproduced by our model without having to assume a jump in the correlation length ξ as in ref. [130]. As energy is injected, first the maximum of the temperature profile (at the center $r = 0$) exceeds the critical value $\theta_2 \simeq 0.15$ at $V \simeq V_1 \simeq 0.025$ and this brings about the small height bump observed in Fig. 4.7 between $V = 0.025$ and V=0.035. Second, as the voltage bias is further increased to $V_c > V_1$, there is a large enough region of the system in which the temperature is above θ_2, which makes the system buckle.

In the considered range of V, $0 \leq V \leq 0.06$, heating ($I \neq 0$) is absolutely necessary to produce membrane buckling because the external field is not strong enough by itself. However, if we further raise V, it would reach a value at which the system buckles even without heating ($I = 0$). Therefore, our model may also be useful to investigate the buckling phenomena observed when strong electrostatic forces are applied, as in refs. [93, 136].

It is worth stressing some further aspects of our numerical results in Fig. 4.7. First, we increase the voltage at a specific rate and, therefore, different curves are obtained for different rates. Of course, a rate-independent equilibrium curve is obtained if the voltage is increased slowly enough, that is, quasi-statically. Second, our numerical results show some time oscillations. Therefore, the present model allows us to resolve the time evolution of the membrane over a finer scale than that of the currently available experimental results, which are time-averaged.

4.5 Conclusions

Our spin-membrane model exhibits a first order phase transition from rippled-flat to buckled membrane for appropriately small values of the non-dimensional temperature and spin-spin coupling. The main parameter to be fixed is κ, that is, the strength of the antiferromagnetic pseudo-spin interaction. Once κ has been chosen in the range where the low-temperature first order phase

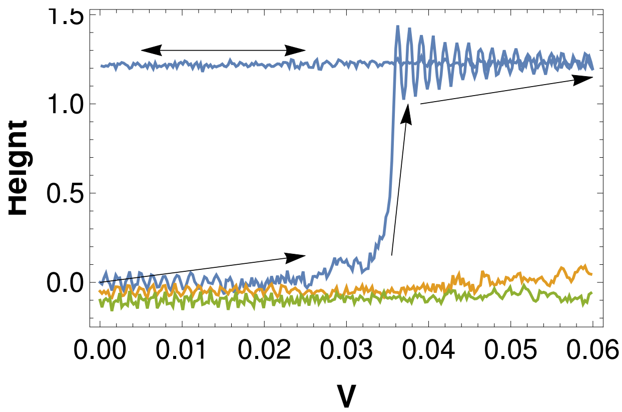

Figure 4.7: Central atom height vs. voltage bias V. The simulations have been conducted in a circular membrane having $N = 1650$ sites. From top to bottom, the lines correspond to tunneling currents $I = \Delta\theta/V = 1$, 2, and 6. The voltage V increases at a constant rate from 0 to $V_{\max}$ in steps $V_{\max}/250$, during a total time $t_{total} = 250$. For clarity, we have shifted downwards the two lowest curves. The curve for $I = 6$ exhibits a small bump around $V \simeq 0.025$, which coincides with the maximum of θ_s reaching 0.15. Once we have reached $V_{\max}$ for $I = 6$, we decrease back the voltage to 0 and then height follows the almost flat upper curve. This shows that the jump at $V \simeq 0.035$ is irreversible.

transition is present, it also determines the temperature θ_2 above which the membrane buckles. The additional quantities controlling the system behavior are I and V, which govern the strength of the Joule effect that heats the membrane, so that the temperature $\theta > \theta_2$, and makes it buckle. Conversely, the characteristic length a (which estimates the radius of interaction between the STM tip and the sample) does not play a key role: changing its value only shifts the range of V and I over which driving through the transition is observed.

Membrane buckling arises from the long range interaction among spins induced by the spin-membrane coupling and the metastable state of a flat membrane with ripples stems from the short-range antiferromagnetic spin-spin coupling. To model the results of Schoelz *et al*'s experiments, we need to drive the system through the first order phase transition by an appropriate control of temperature and the electrostatic interaction between the STM tip and the graphene membrane.

Control of a homogeneous bath temperature induces irreversible buckling but the connection between the parameters of this process and those in the STM experiment is not transparent. Moreover, the STM should heat inhomogeneously the sample. Therefore, we have assumed that the bath temperature adopts the inhomogeneous profile that solves the heat equation with a Gaussian source term. Furthermore, we have introduced an external field term in the spin energy that mimics STM electrostatic force. The latter breaks the spin up-down symmetry which, in turn (via the spin-membrane coupling), breaks the up-down symmetry of the vertical membrane displacements.

The combination of the two above mechanisms produces numerical results that contain every feature of STM buckling experiments, including the existence of a critical value of the current. Our numerical results strongly suggest that both the electrostatic force and heat dissipation are playing a role in the buckling phenomenon observed in ref. [130]. In addition, our spin-membrane model improves that in ref. [130] because it explicitly shows the membrane ripples and it does not need to change the sign of the spin-spin coupling to induce buckling.

There are some hurdles that need to be overcome before finding a microscopic model closer to first principles that explains STM induced buckling of graphene membranes. Firstly, as experiments become more accurate, they may allow for a better definition of all parameters in mesoscopic models, improving the current physical understanding of graphene rippling. Secondly, starting from an electron-phonon Hamiltonian for a suspended graphene sheet, it is possible to derive stationary saddle-point equations for vertical displacements coupled to some auxiliary fields [70]. From these equations, critical temperatures below which there is buckling can be found [30]. These results are qualitatively similar to those found with our spin-membrane model. It seems worth investigating modeling the interaction between the graphene membrane and the STM tip at the level of saddle-point equations. Then some inhomogeneous heating program similar to that in the present paper could be used to explain Schoelz *et al*'s experiments from "first principles".

Finally, note that the buckling transition has been also observed in experiments in which only an electrostatic force is applied to the sample, with no energy injection. Our model can also explain this effect, since the external field term favors that the spins have a well-defined sign, that is, that the sign of the membrane curvature is well-defined. In this respect, a detailed experimental study of buckling in graphene, in which both the temperature (via an energy injection mechanism) and the electrostatic force can be independently changed, would greatly improve our insight into the internal interactions that govern buckling.

Chapter 5

Critical radius and temperature for buckling in graphene

5.1 Introduction

In [70], Guinea *et al.* have developed a model for suspended graphene based in the coupling between flexural phonons and electrons. They consider a 2D membrane in equilibrium that is embedded in a $2 + d$ dimension space, where there are d dimensional *out-of-membrane* displacements ($d = 1$ in the physical situation). Then they eliminate the in-plane phonons, ignore the frequency dependence of the resulting couplings, use the self-consistent screening approximation and perform a saddle-point analysis of the free energy in the limit as $d \to \infty$. The resulting saddle-point equations (SPEs) are time-independent and will be analyzed in the present paper. They consist of one von Kármán type plate equation for the physical out-of-plane displacement coupled to two equations for two auxiliary fields: one "scalar" stress associated to membrane curvature and a field associated to charge fluctuations. We expect these equations to describe buckling and ripples of the graphene membrane in a stable stationary (equilibrium) configuration after all possible transients have decayed. We find *flat membrane* solutions with constant non-zero auxiliary fields. The linearization of the *stationary* SPEs about these solutions accompanied by appropriate boundary conditions provide an eigenvalue problem that yields critical values of temperature and membrane size corresponding to the bifurcation of buckling states from the flat membrane. Why?

The stationary SPEs provide stationary solutions to *not yet derived* dynamic SPEs that should describe the graphene membrane out of equilibrium. Among them, we have found the stationary flat membrane solution. Other solutions may bifurcate from it at appropriate parameter values. To find them, we have to solve the eigenvalue problem that governs the linear stability of the stationary flat membrane solution to dynamic SPEs. The corresponding eigenvalues give the growth of disturbances about the stationary solution. We do not know the precise shape of the dynamic SPEs but we may surmise that stationary solutions bifurcating from the flat membrane appear when these eigenvalues are zero. But linearized dynamic SPEs with zero eigenvalues are the same as linearized stationary SPEs, which we know from [70]. These linearized stationary SPEs have nonzero solutions only for particular values of the constant auxiliary fields that correspond to critical temperature and membrane sizes. The eigenmodes solving these equations give the shape of the buckling states near bifurcation points. A combination of eigenmodes may characterize ripples in graphene.

The rest of the chapter is as follows. In section 5.2 we briefly revise the derivation of the stationary saddle-point equations [70] and write them in real (not Fourier) space. In section 5.3, we find the flat membrane solution of the SPEs for constant auxiliary fields. In Section 5.4, we linearize the plate equation that forms part of the stationary SPE about the flat solution and add appropriate boundary conditions for a finite circular graphene sheet. Thus we obtain an eigenvalue problem for critical values of the constant auxiliary fields. From the critical auxiliary fields, we get critical values of temperature and membrane size at which non-flat buckled solutions may bifurcate from flat ones. The linearized plate equations are solved for a circular monolayer of graphene with two different boundary conditions corresponding to a free graphene layer and to a clamped sample. We obtain different eigenmodes (corresponding to vertical deformations of the layer) together with their respective critical temperatures and radii. The critical radii allow us to predict the minimal size that allows a graphene layer to buckle. Moreover the combination of the different bifurcating modes could be used to characterize ripples in graphene. The last section contains our conclusions.

5.2 Model and saddle-point equations

In [70], Guinea, Le Doussal and Wiese have considered the graphene sheet to be a 2D membrane embedded in a larger space of dimension $d+2$ and interacting with $N_f d$ copies of a free Dirac fermion. The real physical system has $N_f = 4$ (four flavors, two valleys and two spins) and $d = 1$ but Guinea *et al* have derived saddle-point equations involving the out-of-plane displacement in the limit as $d \to \infty$. Here we analyze buckling of the graphene membrane using the saddle-point equations. Let us briefly recall the model, the saddle-point equations and their meaning. The model Hamiltonian consists of:

- The deformation energy of the graphene sheet is the sum of kinetic energy, H_{kin}, and of curvature and elastic energy, H_{elas}, with

$$H_{elas} = \frac{1}{2}\int d^2x[\kappa(\nabla^2 h_a)^2 + \lambda u_{ii}^2 + 2\mu u_{ij}^2]. \tag{5.1}$$

Here u_i, $i = 1, 2$, are the in-plane phonon displacements, h_a, $a = 1, ..., d$ are the out-of-plane flexural phonon modes, $u_{ij} := \frac{1}{2}(\partial_i u_j + \partial_j u_i + \partial_i h_a \partial_j h_a)$, λ and μ are the Lamé constants, and κ is the bending energy.

- The energy of the free Dirac fermions (in units such that $\hbar = 1$),

$$H_e = \int d^2x \sum_{\gamma=1}^{N_f d} \bar{\Psi}_\gamma[-v_F \boldsymbol{\sigma} \cdot (-i\nabla)]\Psi_\gamma. \tag{5.2}$$

Here $\boldsymbol{\sigma} = (\sigma_x, \sigma_y)$ are the Pauli matrices, v_F is the Fermi velocity of Dirac electrons in graphene such that, in these units, $\frac{v_F}{a} = 5$ eV ($a = 1.4$ Å is the side of a graphene hexagon).

- The electron-phonon coupling

$$H_{e-ph} = -g_0 \int d^2x \delta\rho(x) u_{ii}(x), \tag{5.3}$$

$$\delta\rho(x) = \rho(x) - \rho_0 = \frac{1}{d}\sum_{\gamma=1}^{N_f d} \bar{\Psi}_\gamma \mathbb{1} \Psi_\gamma - \rho_0, \tag{5.4}$$

where $\delta\rho(x)$ is the the charge distribution on the graphene layer, ρ_0 is the equilibrium carrier density, and g_0 is in the range between 4 and 50 eV.

- Finally the Coulomb interaction has the form

$$H_{ee} = \frac{1}{2}\int \frac{d^2q}{(2\pi)^2} V_0(q)|\rho(q)|^2, \tag{5.5}$$

where $V_0(q) = \frac{2\pi e^2}{\epsilon_0 q}$ is the Fourier transform of the electrostatic potential, $V_0(r) = e^2/(\epsilon_0 r)$, ϵ_0 is the dielectric constant of the environment and $-e < 0$ is the charge of the electron.

Once all interactions are defined, the resultant Hamiltonian is integrated over the in-plane phonons, leading to a coupled theory of flexural phonon modes and electrons. The frequency dependence of the resulting couplings is ignored, as it is important only for temperatures below 90 K [9], that we do not consider here. In this process, the Coulomb interaction becomes

$$\hat{V}(q) = \frac{2\pi e^2}{\epsilon_0 q} - \frac{g_0^2}{\lambda + 2\mu}. \tag{5.6}$$

The effective Hamiltonian, depending only on the electrons and flexural phonon modes, is used to build a Matsubara equilibrium partition function. For later convenience, this partition function is transformed using two fluctuating auxiliary fields, σ and α, defined through the relation,

$$\begin{aligned} \begin{pmatrix} \sigma(x) \\ \alpha(x) \end{pmatrix} &= \int_{x'} \begin{pmatrix} K_0 & -g \\ -g & \hat{V} \end{pmatrix}_{xx'} \begin{pmatrix} \Phi(x') \\ \delta\rho(x') \end{pmatrix} \\ &= \begin{pmatrix} K_0\Phi(x) - g\delta\rho(x) \\ -g\Phi(x) + \int_{x'} \hat{V}(x-x')\delta\rho(x') \end{pmatrix}. \end{aligned} \tag{5.7}$$

Here $g = \frac{2\mu}{2\mu+\lambda} g_0 \sim g_0$, $K_0 = 4\mu(\mu+\lambda)/(2\mu+\lambda)d$, $(K_0)_{xx'} = K_0\delta(x-x')$, $(g)_{xx'} = g\delta(x-x')$ and table 5.1 gives the dimensions of parameters and variables. In (5.7), $\Phi(x)$ is

$$\Phi(x) = \frac{1}{d}\sum_{a=1}^{d} \frac{1}{2} P_{ij}^T(\partial)\partial_i h_a \partial_j h_a, \tag{5.8}$$

where $P_{ij}^T = \delta_{ij} - \frac{\partial_i\partial_j}{\nabla^2}$ is the transversal projector. With this definition, $\Phi(x)$ is related to the Gaussian curvature ($\mathcal{K}$) through the relation $\Phi(q) = \mathcal{K}(q)/q^2$. In (5.7), $\sigma(x)$ is a local linear combination of $\Phi(x)$ and the charge disturbance $\delta\rho(x)$, whereas $\alpha(x)$ is a nonlocal linear combination, as it involves the potential energy of one electron in x with respect to the charge disturbance distribution in x', $\int_{x'} \hat{V}(x-x')\delta\rho(x')$. The action corresponding to the Matsubara partition function is

$$\begin{aligned} S = &\int d^2x \int_0^\beta d\tau \sum_{a=1}^{d} \left[\frac{\rho}{2}(\partial_\tau h_a)^2 + \frac{\kappa}{2}(\nabla^2 h_a)^2\right] + \frac{1}{\beta}\sum_{\omega_n'} \int_q \Bigg\{ \sum_{\gamma=1}^{N_f d} \bar{\Psi}_\gamma(-q,-\omega_n') \\ &[-v_F\sigma\cdot(-i\nabla) - (i\omega_n' + \mu)\mathbb{1}]\Psi_\gamma(q,\omega_n') \Bigg\} + \int_{x\tau} \Bigg\{ \sigma(x) \left[\frac{1}{2}P_{ij}^T(\partial)\sum_{a=1}^{d} \partial_i h_a \partial_j h_a\right] \\ &+ \alpha(x)\sum_{\gamma=1}^{N_f d} \bar{\Psi}_\gamma \mathbb{1}\Psi_\gamma \Bigg\} - \frac{d}{2}\int_{xx'\tau} \begin{pmatrix} \sigma & \alpha \end{pmatrix}_{x\tau} \begin{pmatrix} K_0 & -g \\ -g & \hat{V} \end{pmatrix}^{-1}_{xx'} \begin{pmatrix} \sigma \\ \alpha \end{pmatrix}_{x'\tau}, \end{aligned} \tag{5.9}$$

Dimensions of variables									
$\sigma(x)$	$\alpha(x)$	K_0	g	$V(x)$	$\hat{V}(q)$	$\Phi(x)$	$\delta\rho(x)$	v_F	κ
$\frac{E}{L^2}$	E	$\frac{E}{L^2}$	E	E	EL^2	1	L^{-2}	EL	E

Table 5.1: Dimensions of the parameters and variables appearing in equations (5.7), (5.11) and (5.12). E for energy and L for length dimension.

where μ is the chemical potential. We now decompose the vertical displacements into an average and a fluctuating part, $h_a = \langle h_a \rangle + \delta h_a$, and assume symmetry breaking in the direction $a = 1$, $\langle h_a \rangle = \delta_{a1} h_1 \neq 0$. Integrating over the fermions and the fluctuating part of the vertical displacements, the action is [70]

$$\begin{aligned}\frac{S'}{d} &= \frac{1}{2}\mathrm{tr}\ln(-\rho\partial_\tau^2 + \kappa\nabla^4 - \left[P^T_{ij}(\partial)\sigma(x,\tau)\right]\partial_i\partial_j) - \frac{N_f}{2}\mathrm{tr}\ln(-v_F\left[\sigma\cdot(-i\nabla)\right] \\ &+ \left[\alpha(x,\tau) - \mu - \partial_\tau\right]\mathbb{1}) - \frac{1}{2}\int\limits_{xx'\tau}\begin{pmatrix}\sigma & \alpha\end{pmatrix}_{x\tau}\begin{pmatrix}K_0 & -g\\ -g & \hat{V}\end{pmatrix}^{-1}_{xx'}\begin{pmatrix}\sigma\\ \alpha\end{pmatrix}_{x'\tau} \\ &+ \frac{1}{d}\int\limits_{x,\tau}\left[\frac{\kappa}{2}(\nabla^2 h_1)^2 + \frac{\rho}{2}(\partial_\tau h_1)^2 + \frac{\sigma}{2}P^T_{ij}(\partial)\partial_i h_1\partial_j h_1\right]. \end{aligned} \tag{5.10}$$

To obtain the saddle-point equations, we vary (5.10) with respect to σ, α and h_1, thereby obtaining

$$\int_{x'}\begin{pmatrix}K_0 & -g\\ -g & \hat{V}\end{pmatrix}^{-1}_{xx'}\begin{pmatrix}\sigma_0(x')\\ \alpha_0(x')\end{pmatrix} =$$
$$\begin{pmatrix} P^T_{ij}\partial_{x_i}h(x)\partial_{x_j}h(x) - \frac{1}{2\beta}\sum_{\omega_n}P^T_{ij}\partial_{x_i}\partial_{x_j}[\rho\omega_n^2 + \kappa\Delta_y^2 - P^T_{lm}\sigma_0(y)\partial_{y_l}\partial_{y_m}]^{-1}_{xx} \\ \frac{4}{\beta}\sum_{\omega_n'}(i\omega_n')[(i\omega_n' - \alpha_0(y) + \mu)^2 + v_F^2\nabla_y^2]^{-1}_{xx}\end{pmatrix}. \tag{5.11}$$

$$-\kappa\Delta^2 h + \partial_{x_i}(\sigma_{ij}\partial_{x_j}h) = 0, \tag{5.12}$$

$$\partial_{x_i}\sigma_{ij} = 0, \tag{5.13}$$

$$\sigma_{ij} = P^T_{ij}\sigma_0 = (\delta_{ij} - \partial_{x_i}\partial_{x_j}\Delta^{-1})\sigma_0, \tag{5.14}$$

where we have replaced $h_1 = h$ and not yet made $\mu = 0$ as in [70]. Eq. (5.11) provides the average fields $\sigma_0 = \langle\sigma(x)\rangle$ and $\alpha_0 = \langle\alpha\rangle$ in terms of h. The average auxiliary fields are related to the averages of the charge distribution (5.4) and of the field (5.8),

$$\Phi_0(x) = \frac{1}{d}\left\langle \sum_{a=1}^{d} \frac{1}{2} P^T_{ij}(\partial)\partial_i h_a \partial_j h_a \right\rangle, \quad \delta\rho_0(x) = \langle \delta\rho(x) \rangle, \tag{5.15}$$

by the linear equation (5.7), which also holds for the averages of the corresponding quantities. (5.12), (5.13) and (5.14) are von Karman plate equations (they appear in Fourier transform form in [70]). The stress tensor σ_{ij} is generated by the average auxiliary field σ_0 and it is automatically in equilibrium as $\partial_{x_i} P^T_{ij} = 0$. P^T_{ij} is the transversal projector, and $\omega_n = 2\pi n/\beta$ and $\omega'_n = 2\pi(n + \frac{1}{2})/\beta$ are the bosonic and fermionic Matsubara frequencies. The matrix Green function appearing in (5.11) satisfies

$$\begin{aligned} \int_{x''} \begin{pmatrix} K_0 & -g \\ -g & \hat{V} \end{pmatrix}_{xx''} \begin{pmatrix} K_0 & -g \\ -g & \hat{V} \end{pmatrix}^{-1}_{x''x'} &\equiv \int_{x''} \begin{pmatrix} K_0 & -g \\ -g & \hat{V} \end{pmatrix}_{xx''} \mathcal{G}(x'', x') \\ &= \begin{pmatrix} 1 & 0 \\ 0 & 1 \end{pmatrix} \delta(x - x'), \end{aligned} \tag{5.16}$$

and $\mathcal{G}(x'', x')$ can be computed from (5.16) as

$$\begin{aligned} \mathcal{G}(x, x') &= \frac{1}{4\pi^2} \int_q e^{iq(x-x')} \frac{1}{\left(K_0 \hat{V}(q) - g^2\right)} \begin{pmatrix} \hat{V}(q) & g \\ g & K_0 \end{pmatrix} \\ &\equiv \frac{1}{4\pi^2} \int_q e^{iq(x-x')} \hat{\mathcal{G}}(q). \end{aligned} \tag{5.17}$$

It is clear from (5.17) that $\mathcal{G}(x, x') = \mathcal{G}(x - x')$. Using this translation invariant Green's function, we can write (5.11) as

$$\begin{aligned} &\begin{pmatrix} \sigma(x) \\ \alpha(x) \end{pmatrix} = \int_y \begin{pmatrix} K_0 & -g \\ -g & \hat{V} \end{pmatrix}_{xy} \\ &\begin{pmatrix} P^T_{ij}\partial_{y_i} h(y) \partial_{y_j} h(y) - \frac{1}{2\beta} \sum_{\omega_n} P^T_{ij} \partial_{y_i} \partial_{y_j} [\rho\omega_n^2 + \kappa\Delta_z^2 - P^T_{lm}\sigma(z)\partial_{z_l}\partial_{z_m}]^{-1}_{yy} \\ \frac{4}{\beta} \sum_{\omega'_n} (i\omega'_n)[(i\omega'_n - \alpha(z) + \mu)^2 + v_F^2 \nabla_z^2]^{-1}_{yy} \end{pmatrix} \end{aligned} \tag{5.18}$$

Henceforth from this equation we suppress the subscript 0 in all average quantities.

Let us now set $\mu = 0$ as in [70]. It is important to note that the flat membrane $h(x) = 0$ is always a solution of (5.12). However, the right side of (5.18) is not zero for $h(x) = 0$ and therefore the trivial solution ($h = \sigma = \alpha = 0$) is not a valid solution of the SPEs. As we will see in the next section,

$h = 0$ and non-zero σ and α is a valid solution. Nonzero auxiliary fields σ and α provide a residual stress that induces plate buckling and rippling below a certain critical temperature and over a critical plate size. In a mathematically related phenomenon, a growing bacterial biofilm can be modeled as a plate with a growth tensor that modifies the elastic part of strain, acts as residual stress and may trigger ripples (called wrinkles in that application) [48]. The critical growth term may then be sought by solving an appropriate eigenvalue problem for $h(x)$ coming from the linearized plate equations [44].

5.3 Flat membrane with constant auxiliary fields

We now seek simple solutions of equations (5.12)-(5.14) and (5.18) with $\mu = 0$, $\sigma(x) = \sigma$ (a constant), $\alpha(x) = \alpha$ (a constant) and $h(x) = 0$. Using that

$$P_{ij}^T \partial_{x_i} \partial_{x_j} = 0, \quad [(i\omega_n' - \alpha(y))^2 + v_F^2 \nabla_y^2]_{xx}^{-1} = \int_q \frac{1}{(i\omega_n' - \alpha)^2 - v_F^2 q^2}, \tag{5.19}$$

and (5.17), Equation (5.18) now becomes

$$\begin{pmatrix} \sigma \\ \alpha \end{pmatrix} = \begin{pmatrix} K_0 & -g \\ -g & \hat{V}(0) \end{pmatrix} \begin{pmatrix} 0 \\ \frac{4}{\beta} \sum_{\omega_n'} \int_q \frac{i\omega_n'}{(i\omega_n' - \alpha)^2 - v_F^2 q^2} \end{pmatrix}, \tag{5.20}$$

where $\hat{V}(0) \approx V(q = 0) = 2\pi e^2 R/\epsilon_0$ ($1/R$ is an infrared cutoff resulting from the graphene sheet radius) is its regularized version and the constant appearing in (5.6) has been neglected. The right side of (5.20) is computed separately in Appendix B.2 with the result

$$\frac{4}{\beta} \int_q \sum_{\omega_n'} \frac{i\omega_n'}{(i\omega_n' - \alpha)^2 - v_F^2 q^2} \sim \frac{v_F \Lambda^2 - 2\alpha\Lambda}{2\pi v_F} + \frac{\alpha^2}{2\pi v_F^2} - \frac{\pi}{6\beta^2 v_F^2}, \tag{5.21}$$

where $\Lambda = 2\pi/a$ is an ultraviolet momentum cutoff (a is the side of a graphene hexagon). The term $\Lambda^2/2\pi$ in (5.21) is proportional to the area of the Brillouin zone, and it will play a key role in the computation of the critical temperature and radius for the graphene layer. We discuss in Appendix B.3 other possible interpretations of (5.20) that do not involve setting the chemical potential $\mu = 0$ and turn out to be unphysical. From (5.20) we obtain

$$\sigma = -\frac{\alpha g}{V(0)}, \tag{5.22}$$

$$\frac{\alpha}{V(0)} \sim \frac{v_F \Lambda^2 - 2\alpha\Lambda}{2\pi v_F} + \frac{\alpha^2}{2\pi v_F^2} - \frac{\pi}{6\beta^2 v_F^2}. \tag{5.23}$$

The left side of (5.23) is much smaller than the right side and it can be ignored, thereby producing the solution

$$\frac{\alpha}{v_F\Lambda} \sim 1 \pm \frac{\pi}{\sqrt{3}\beta v_F\Lambda}, \tag{5.24}$$

which gives σ by insertion in (5.22).

5.4 Linearized equation and eigenvalue problem

We want to ascertain the linear stability of the solution found in the previous section, $h = 0$ and constant auxiliary fields. For this we need to know the dynamics and to linearize the corresponding SPEs about this solution. Let us assume that the dynamic SPEs are

$$\mathcal{F}(\mathbf{u};p) = \mathcal{G}\left(\frac{\partial \mathbf{u}}{\partial t}, \frac{\partial^2 \mathbf{u}}{\partial t^2}\right), \quad \mathbf{u} = \left(\begin{array}{c} h \\ \sigma \\ \alpha \end{array}\right), \tag{5.25}$$

so that

$$\mathcal{F}(\mathbf{u};p) = \mathbf{0}, \quad \mathcal{G}(\mathbf{0},\mathbf{0}) = \mathbf{0}, \tag{5.26}$$

are the stationary SPEs (5.12)-(5.14) and (5.18). Let $\mathbf{u}_0(p)$ be the flat solution $h = 0$ and constant $\sigma(p)$ and $\alpha(p)$ of (5.22) and (5.24). Here p is a bifurcation parameter, later to be identified as the temperature or the radius of a circular graphene membrane. Linear stability about $\mathbf{u}_0$ follows from substituting $\mathbf{u}(t) = \mathbf{u}_0 + e^{\upsilon t}\mathbf{U}$ in (5.25) and keeping terms of order $\mathbf{U}$ in the result. We obtain the eigenvalue problem

$$\frac{\delta\mathcal{F}}{\delta\mathbf{u}}(\mathbf{u}_0(p);p)\mathbf{U} = \upsilon\left[\frac{\delta\mathcal{G}}{\delta\partial\mathbf{u}/\partial t}(\mathbf{0},\mathbf{0}) + \upsilon\frac{\delta\mathcal{G}}{\delta\partial^2\mathbf{u}/\partial t^2}(\mathbf{0},\mathbf{0})\right]\mathbf{U}, \tag{5.27}$$

where $\frac{\delta\mathcal{F}}{\delta\mathbf{u}}$, $\frac{\delta\mathcal{G}}{\delta\partial\mathbf{u}/\partial t}$ and $\frac{\delta\mathcal{G}}{\delta\partial^2\mathbf{u}/\partial t^2}$ are functionals acting upon $\mathbf{U} \equiv \mathbf{U}(x)$. For appropriate values of p, the real parts of all eigenvalues υ are negative and the flat constant solution $\mathbf{u}_0(p)$ is linearly stable. Then zero eigenvalues or eigenvalues with zero real part give the critical values at which non-flat solutions bifurcate from the flat constant solution. Stationary solutions bifurcate from $\mathbf{u}_0(p)$ at those critical values of p for which $\upsilon = 0$. At such p_c, (5.27) becomes

$$\frac{\delta\mathcal{F}}{\delta\mathbf{u}}(\mathbf{u}_0(p_c);p_c)\mathbf{U} = \mathbf{0}. \tag{5.28}$$

While the dynamic SPEs are not known, (5.28) are the *known* linearized stationary SPEs about the flat constant solution. We consider (5.28) as an eigenvalue problem for the critical values p_c and proceed to determine "eigenvalues" p_c. The corresponding eigenvectors $\mathbf{U}$ are buckling modes of the membrane issuing forth from the flat constant solution. When many of these modes become active we may have generated a variety of rippling states of the graphene sheet.

To solve the linearized stationary SPEs, we need appropriate boundary conditions. To solve the linearized plate equation (5.12), we need the value of σ_{ij} in (5.13) for the constant σ and α of (5.22) and (5.24). Now $u = \Delta^{-1}\sigma$ solves the equation $\Delta u = \sigma$ with appropriate boundary conditions. A solution is

$$u = \frac{\sigma}{4}|\mathbf{x}|^2 + u_0, \quad \Delta u_0 = 0.$$

For a circular plate with zero data Dirichlet boundary conditions at $r = R$ the solution is $u = \frac{\sigma}{4}(r^2 - R^2)$. Then, by (5.13) and (5.14), $\sigma_{ij} = \sigma\delta_{ij}/2$, and (5.12) becomes

$$\Delta^2 h = \frac{\sigma}{2\kappa}\Delta h. \tag{5.29}$$

There are different eigenvalue problems associated to solving Equation (5.29) with different boundary conditions for a finite graphene membrane. Each of these problems yield its critical temperature and size and allows us to know the shape of different eigenmodes that appear as buckled solutions of the suspended layer of graphene. We consider a finite circular layer of graphene with a free border (natural boundary conditions) or a graphene sheet clamped to a circular hole. Suspended graphene sheets are clamped at their boundaries but the case of a free border is easier to treat mathematically, so we start by analyzing it.

5.4.1 Membrane with free border

The natural boundary conditions to solve (5.29) for a free circular graphene layer of radius R are

$$\Delta h = 0 \quad \text{and} \quad \left(\Delta - \frac{\sigma}{2\kappa}\right)\partial_r h = 0 \quad \text{at } r = R. \tag{5.30}$$

Let us first solve the eigenvalue problem for $H = \Delta h$: $\Delta H - \frac{\sigma}{2\kappa}H = 0$ with $H = 0$ at $r = R$. We find the solution

$$H_{n,m} = \frac{1}{a}e^{im\theta}J_m\left(\frac{\gamma_{n,m}r}{R}\right), \quad \frac{\sigma}{2\kappa} = -\frac{\gamma_{n,m}^2}{R^2}, \tag{5.31}$$

where $J_m(\gamma_{n,m}) = 0$, $n = 1, 2, \ldots$, $m = 0, 1, 2, \ldots$. The lowest possible value of σ in (5.31) corresponds to the first zero $\gamma_{1,0} = 2.4048$ of the Bessel function $J_0(x)$. Note that $\gamma_{1,0} < \gamma_{1,1} < \gamma_{1,2} < \gamma_{2,0} < \gamma_{1,3}$. Thus there are two eigenvalues corresponding to azimuthal eigenfunctions ($m = 1, 2$) between the first two eigenvalues corresponding to radially symmetric eigenfunctions with $m = 0$.

The solution of $\Delta h = H$ that satisfies the other boundary condition is

$$h_{n,0}(r) = \frac{R^2}{a\gamma_{n,0}^2}\left[1 - J_0\left(\frac{r\gamma_{n,0}}{R}\right)\right], \tag{5.32}$$

for $m = 0$ (normalized so that $h_{n,0}(0) = 0$), and

$$h_{n,m}(r, \theta) = -\frac{R^2}{a\gamma_{n,m}^2} e^{im\theta} J_m\left(\frac{\gamma_{n,m} r}{R}\right), \tag{5.33}$$

for $m > 0$.

We are interested in computing the critical temperature and radii. To this end, we use (5.31) with equations (5.22) and (5.24), and find that ripples appear below the critical temperature

$$T_c = \frac{2\sqrt{3}v_F}{a}\left|1 - \frac{e^2}{\epsilon_0 v_F}\frac{2a\kappa}{Rg}\gamma_{1,0}^2\right|. \tag{5.34}$$

Note that the critical temperature decreases as the size R decreases. As $R/a \to \infty$, the critical temperature tends to $\frac{2\sqrt{3}v_F}{a} \approx 16.05$ eV (about 186,000 K). For finite membrane size, (5.34) with $\gamma_{n,m}$ instead of $\gamma_{1,0}$ produces the following numerical estimate,

$$1 - 5.4 \times 10^{-6}\, T_{n,m} = \frac{1.6\, \gamma_{n,m}^2}{R}. \tag{5.35}$$

Here $T_{n,m}$ is the temperature (measured in Kelvin) at which the mode $h_{n,m}$ appears and R is measured in nanometers. The values considered for the parameters are $g = 3.9$ eV (the lowest value considered in [70]) and $\kappa = 1$ eV. At room temperature, equation (5.35) gives us different critical radii above which the different modes $h_{n,m}$ (characterised by $\gamma_{n,m}$) appear, see table 5.2 and figure 5.1.

5.4.2 Clamped Membrane

In this more realistic case, the boundary conditions are $\tilde{h} = 0$ and $\partial_r \tilde{h} = 0$ at $r = R$ instead of (5.30). We use $\tilde{h}$ instead of h to distinguish the out-of-plane displacement in the clamped case. Following the same procedure as

h:	$h_{1,0}$	$h_{1,1}$	$h_{1,2}$	$h_{2,0}$
R_c (nm):	9	24	43	50

Table 5.2: Critical radii given by Equation (5.35) for a circular layer graphene at room temperature with natural boundary conditions. Mode $h_{n,m}$ appears from the flat solution for $R > R_c$.

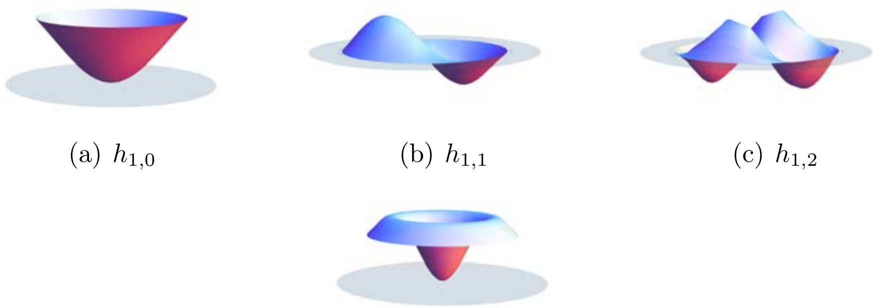

(a) $h_{1,0}$ (b) $h_{1,1}$ (c) $h_{1,2}$ (d) $h_{2,0}$

Figure 5.1: (Color online) Modes appearing over their respective critical radii, see table 5.2. For a suspended layer of graphene of radius R and free boundaries, all modes with $R_c < R$ can combine to produce ripples or buckling. The grey disk is the plane $h = 0$.

for equations (5.31) and (5.32), we get

$$H_{n,m} = \frac{1}{a} e^{im\theta} J_m(kr), \quad k^2 = -\frac{\sigma}{2\kappa}, \tag{5.36}$$

instead of (5.31), and in which k is not yet determined. Now the radial part $\tilde{h}_m(r)$ satisfies

$$\left(\partial_r^2 + \frac{1}{r}\partial_r - \frac{m^2}{r^2}\right)\tilde{h}_m = \frac{1}{a} J_m(kr). \tag{5.37}$$

For $m = 0$, this equation is

$$\partial_r(r\partial_r\tilde{h}) = \frac{r}{a} J_0(kr) \Longrightarrow r\partial_r\tilde{h} = \frac{1}{ka}[rJ_1(kr) - RJ_1(kR)],$$

in which we have used the boundary condition $\tilde{h}'(R) = 0$. Integrating once and using $\tilde{h}(R) = 0$, we obtain

$$\tilde{h}(r) = \frac{1}{k^2 a}[J_0(kR) - J_0(kr)] - \frac{R}{ka} \ln\left(\frac{r}{R}\right) J_1(kR).$$

The vertical displacement is unbounded at $r = 0$ unless

$$J_1(kR) = 0 \Longrightarrow \frac{\sigma}{2\kappa} = -\frac{\gamma_{n,1}^2}{R^2}. \tag{5.38}$$

Then

$$\tilde{h}_{n,0}(r) = \frac{R^2}{\gamma_{n,1}^2 a}\left[J_0(\gamma_{n,1}) - J_0\left(\frac{\gamma_{n,1} r}{R}\right)\right]. \tag{5.39}$$

Similarly, for $m > 0$ the solution of $\Delta\tilde{h} = H_{n,m}$ is

$$\tilde{h}_{n,m}(r,\theta) = \left(\frac{c_1}{r^m} + c_2 r^m\right) e^{im\theta} + \frac{r^m}{a} e^{im\theta} \int_0^r \frac{dr}{r^{2m+1}} \int_0^r ds\, s^{m+1} J_m(ks). \tag{5.40}$$

Clamped boundary conditions yield

$$c_2 = -\frac{1}{a}\int_0^R \frac{dr}{r^{2m+1}} \int_0^r ds\, s^{m+1} J_m(ks) - \frac{c_1}{R^{2m}}, \tag{5.41}$$

$$c_1 = \frac{1}{2ma}\int_0^R ds\, s^{m+1} J_m(ks) = \frac{R^{m+2}}{2ma}\int_0^1 ds\, s^{m+1} J_m(kRs) = \frac{R^{m+1}}{2mka} J_{m+1}(kR). \tag{5.42}$$

The condition that $\tilde{h}_{n,m}$ be bounded at $r = 0$ produces $c_1 = 0$. Thus $J_{m+1}(kR) = 0$, i.e., $k = \gamma_{n,m+1}/R$ and therefore

$$\frac{\sigma}{2\kappa} = -\frac{\gamma_{n,m+1}^2}{R^2}. \tag{5.43}$$

$\tilde{h}$:	$\tilde{h}_{1,0}$	$\tilde{h}_{1,1}$	$\tilde{h}_{1,2}$	$\tilde{h}_{2,0}$
R_c (nm):	24	43	66	80

Table 5.3: Critical radii given by Equation (5.35) for a circular layer graphene at room temperature with clamped boundary conditions. Mode $\tilde{h}_{n,m}$ appears from the flat solution for $R > R_c$.

Equation (5.40) becomes

$$\begin{aligned}\tilde{h}_{n,m}(r,\theta) &= \frac{r^m}{a}e^{im\theta}\int_R^r \frac{dr}{r^{2m+1}}\int_0^r ds\, s^{m+1}J_m\Big(\frac{\gamma_{n,m+1}s}{R}\Big) \\ &= -\frac{R^2 e^{im\theta}}{\gamma_{n,m+1}a}\Big(\frac{r}{R}\Big)^m\int_{r/R}^1 \frac{ds}{s^m}J_{m+1}(\gamma_{n,m+1}s) \\ &= \frac{R^2 e^{im\theta}}{a\gamma_{n,m+1}^2}\Big\{\Big(\frac{r}{R}\Big)^m J_m(\gamma_{n,m+1}) - J_m\Big(\gamma_{n,m+1}\frac{r}{R}\Big)\Big\}, \qquad (5.44)\end{aligned}$$

which agrees with (5.39) for $m = 0$.

According to (5.43), the critical radii are given by (5.35) with $\gamma_{n,m+1}$ instead of $\gamma_{n,m}$. Then the critical radii of table 5.3 are greater than those in table 5.2, and buckling of a clamped graphene membrane should be observable only for radii over 24 nm. Thus a clamped membrane remains flat for larger radii than in the case of natural free boundary conditions. This is according to our intuition that it is harder to buckle a clamped membrane than a membrane with a free border. The lowest possible value of σ in (5.31) corresponds to $\gamma_{1,1} = 3.8317$. Note that $\gamma_{1,1} < \gamma_{1,2} < \gamma_{1,3} < \gamma_{2,1}$. Again there are two eigenvalues corresponding to azimuthal eigenfunctions ($m = 1, 2$) between the first two eigenvalues corresponding to radially symmetric eigenfunctions with $m = 0$. These first four modes given by (5.44) are depicted in figure 5.2.

5.5 Conclusions

In conclusion, the stationary saddle-point equations give the vertical displacement of a graphene membrane and auxiliary fields associated to curvature and to charge fluctuations, provided elasticity and phonon-electron interaction are considered [70]. We have solved these equations for a flat circular graphene sheet under constant auxiliary fields. We have then solved

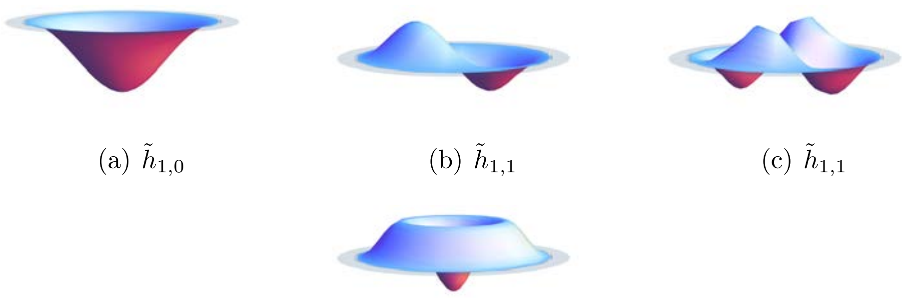

(a) $\tilde{h}_{1,0}$ (b) $\tilde{h}_{1,1}$ (c) $\tilde{h}_{1,1}$

(d) $\tilde{h}_{2,0}$

Figure 5.2: (Color online) Modes appearing over their respective critical radii, see table 5.2. In a suspended layer of graphene clamped on a circular hole of radius R all modes with $R_c < R$ can appear and combine to form ripples and buckling. The grey disk is the substrate plane $h = 0$.

the SPEs linearized about the flat membrane solution and subject to either free or clamped boundary conditions. The latter problem has nonzero solutions only for discrete values of the auxiliary fields. These discrete values correspond to critical values of temperature and membrane radius at which buckling membrane solutions issue forth from the flat membrane. The flat membrane is stable only for temperatures larger than critical and radii smaller than critical. For an infinite membrane, the predicted critical temperature is extremely large and unphysical (186,000 K). However, critical radii at room temperature are in the nanometer range. Different modes of membrane buckling appear below specific critical temperatures and over specific critical radii, see tables 5.2 and 5.3. The stability of these modes is to be analytically determined, but experiments describing rippling [99] and buckling [130] of graphene show that the flat solution is not stable in most cases: Flat graphene has only been observed when it stands over a substrate [95].

The calculated critical radii (tables 5.2 and 5.3) suggest that the different modes appearing in figures 5.1 and 5.2 could be observed for a specific temperature and membrane size. This brings the opportunity to develop new experiments, as no buckling should appear below the minimum critical radius R_c. Similar experimental procedures to the ones in [93, 136, 143], where suspended graphene layers were forced to buckle using an external electrical potential or a STM, could be used to determine the value of R_c and the validity of our results. For this purpose, suspended graphene layers may be clamped to holes of different dimensions, under different temperatures. Checking when the layer may or not buckle, it should be possible to get a better estimation of g and κ by fitting the results of experiments with equation (5.34).

A different approach to study the effects due to the existence of non-flat modes would be experiments with graphene resonators [37, 47]. In this setting, when the external driving force is sufficiently strong to deform the graphene layer close to one of the stable buckling modes (away from the flat configuration), the response of the resonator should be extremely nonlinear. Instead of oscillating around a single potential well (more or less parabolic) corresponding to the rippled configuration, the system may oscillate under influence of two different potential wells (the buckling modes). This effect could be measured by observing oscillation damping once the driving force is turned off.

Characterization of ripples in suspended graphene is not yet accurate enough to compare with our results. Once the experimental techniques have been improved, experiments with suspended graphene layers clamped to holes of different radii should show ripples that are combination of the possible bifurcating modes for these membranes (table 5.3).

The study of different solutions of the SPEs with position-dependent auxiliary fields σ and α is left as future work. From a theoretical point of view, it is also interesting to take into account the influence of external forces, such as an electrostatic force, and to study the resulting dynamical effects. Then we may be able to reproduce the transition from the flat membrane with superimposed ripples to the buckled membrane and compare with existing STM experimental results [130].

Part II

Dynamics and chaos in semiconductor superlattices

Motivation

A doped, weakly coupled semiconductor superlattice (SSL) represents an almost ideal spatially one-dimensional nonlinear dynamical system with a large number of degrees of freedom, the nonlinearity of which is due to sequential resonant tunneling between adjacent quantum wells. Fluctuations of the layer thicknesses, electron density, energy levels, and inter-well coupling transform a weakly coupled SSL into a complex nonlinear system, in which the electron transport is strongly dissipative. A great richness of nonlinear transport behavior has been observed in weakly coupled SSLs, including the formation of stationary electric-field domains, periodic as well as quasi-period current self-oscillations, and even driven as well as undriven chaos [20, 27]. The oscillatory behavior is due to the recycling and motion of domain walls separating low and high electric field domains [27]. Only very recently, spontaneous chaotic [75] and quasi-periodic [74] current self-oscillations were observed at room temperature in GaAs/(Al,Ga)As SSLs using an Al content of 45%, which results in the largest direct barrier for this materials system.

Fast random number generators (RNGs) are relied upon for many applications including, inter alia, data encryption systems, stochastic modeling, and secure communication [56, 106, 134]. In many cases, the RNG is substituted by a numerical algorithm that produces a seemingly unpredictable sequence of numbers when a short random 'seed' is entered as input [11]. While this approach is convenient and inexpensive, the resulting number sequences are only pseudorandom, i.e. the algorithm will produce identical number sequences given identical seeds. To eliminate this vulnerability, it is necessary to find fast and reliable physical sources of entropy that produce true random number sequences. Recently, chaotic semiconductor lasers [78, 101, 116, 131, 137] and superlattices [92] have been used for fast generation of truly random numbers at a rate of tens or hundreds of Gb/s. In both cases, quantum fluctuations are coupled with chaotic dynamics to produce a macroscopic fluctuating signal that is detectable using conventional electronics. However, while semiconductor lasers require a mixture of optical and electronic components, semiconductor superlattices (SSLs) are entirely electronic submicron devices that are more readily integrated into complex circuits, see Figure 7.1. Hence SSLs could be vastly useful, as the security of digital computers and networks relies on fast generation of truly random numbers.

Chapter 6

Noise-enhanced chaos in a weakly coupled GaAs/(Al,Ga)As superlattice

6.1 Introduction

With the continuous advancement of nonlinear science and the theory of random dynamical systems, we have become aware of the fact that noise should not always be considered as a disturbing factor. Actually, a small amount of noise may enhance the dynamics of a system so that it becomes better defined and controllable. Constructive effects of noise in nonlinear systems have been investigated extensively in the context of stochastic resonances and coherence resonances. By stochastic resonance, noise can optimize the response of a bistable system to periodic external signal and induce stochastic phase synchronization to the external force [57, 142]. For a coherence resonance, pure noise without an external signal can generate a coherent oscillation in the system, which has been observed in excitable systems [58, 149].

Both theoretical and experimental results have proven that noise can affect the charge transport in weakly coupled GaAs/AlAs SSLs [19, 73]. A noise-enhanced coherence resonance has been observed in a weakly coupled GaAs/AlAs SSL at 77 K [76]. The main reason for the existence of such a coherence resonance in such a SSL is related to the interaction between the noise and the two oscillation modes existing in weakly coupled SSL oscillators such as the well-to-well hopping mode and the dipole-motion mode. On this basis, numerical simulations have shown that noise enhances spontaneous chaos at room temperature [5, 21].

In this chapter, we report clear evidence for noise-enhanced spontaneous chaos in a doped, weakly coupled GaAs/$Al_{0.45}Ga_{0.55}As$ SSL at room temperature. We find that, with increasing noise amplitude, spontaneous chaotic oscillations appear over a wider range of voltages. The experimentally observed results are qualitatively very well validated by numerical simulations based on a discrete resonant tunneling model that captures the main features of vertical transport in doped, weakly coupled SSLs [5, 21]. The chapter is organized as follows. In the next section, we describe the sample structure and measurement techniques followed by the experimental results of the current-voltage characteristics, the current self-oscillations, and attractors extracted from the experimental results. In Sec. 6.3, we present the discrete resonant-tunneling model and the results of the numerical simulations. Finally, we summarize the obtained results and conclude in Sec. 6.4.

6.2 Experimental results

6.2.1 Sample structure and measurement techniques

The sample consists of a doped, weakly coupled GaAs/(Al,Ga)As SSL with 50 periods, each period consisting of a GaAs quantum well and an $Al_{0.45}Ga_{0.55}As$ barrier. The central 3 nm of each 7-nm-thick GaAs well are doped with Si at a density of 2×10^{17} cm^{-3}. The thickness of the $Al_{0.45}Ga_{0.55}As$ barriers is 4 nm, resulting in a rather weak coupling between adjacent quantum wells. The SSL is sandwiched between two highly doped GaAs contact layers forming an n^+-n-n^+ diode. For more details of the sample structure, see Ref. [91]. After plasma etching and providing Ohmic contacts of AuGe/Ni/Au with 35/10/500 nm using electron beam evaporation followed by rapid thermal annealing at 420 °C, square mesas with a side length of 30 μm are investigated. Single devices are wire bonded for electrical measurements. All experimental measurements are performed at room temperature. The DC bias voltage V_{DC} and the noise with amplitudes V_{noise} are applied using the function generator Agilent 33220A. The current-time traces and the frequency spectra are recorded with a 6 GHz oscilloscope LeCroy Wavepro 760Zi-A. For the current-time traces, the oscilloscope records voltage pulses, which are then converted in current values using the I-V characteristics. A schematic of the measurement circuit is shown in Fig. 6.1, which is the same as the one in Ref. [76].

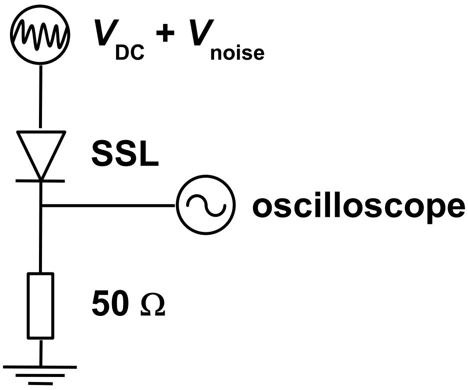

Figure 6.1: Schematic of the experimental setup. The DC bias voltage V_{DC} and the noise with amplitudes V_{noise} are supplied by a function generator. The current-time traces and the frequency spectra are recorded with a 6 GHz oscilloscope over a 50 Ω resistor.

6.2.2 Current-voltage characteristics

A typical current-voltage characteristic of the the doped, weakly coupled SSL device is shown in Fig. 6.2. In the voltage range between 850 and 860 mV, the DC current rapidly increases from 1.24 to 1.55 mA, followed by a current plateau between 860 and 930 mV. In this voltage range, electric-field domains are formed with a charge accumulation layer forming the domain boundary. As the voltage increases further to 940 mV, the current decreases to 1.50 mA and then continues down to 1.31 mA.

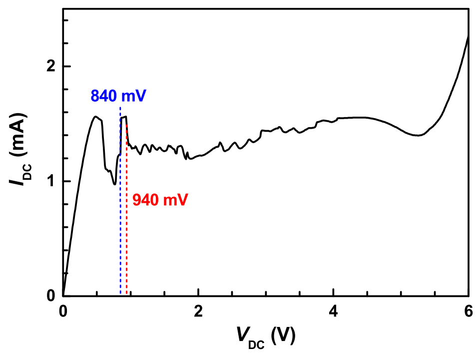

Figure 6.2: Measured current I_{DC} versus voltage V_{DC} of the doped, weakly coupled GaAs/$\mathrm{Al_{0.45}Ga_{0.55}As}$ SSL at room temperature. At $V_{\mathrm{DC}} = 840$ and 940 mV, the frequency spectra are dominated by broad-band noise.

6.2.3 Current self-oscillations and frequency spectra

The frequency spectra displayed in Fig. 6.3(a) recorded between V_{DC} = 800 and 960 mV without any external noise do not show any current self-oscillations for V_{DC} values between 840 and 940 mV. For V_{DC} values outside this region, i. e., smaller than 840 or larger than 940 mV, the frequency spectra exhibit periodic oscillations with higher-order harmonics, and the fundamental frequency depends on V_{DC}. At V_{DC} = 840 and 940 mV, where the transitions between current oscillations and no current oscillations occur, the frequency spectra are dominated by an abrupt decrease to zero frequency. These transitions are accompanied by an abrupt change of the current as shown in Fig. 6.2. This observation may indicate an infinite period collision of the oscillatory attractor with a homoclinic orbit. Numerical simulations confirm this scenario for the SSL model.

Figures 6.3(b) and 6.3(c) show the frequency spectra for applying additional external noise with amplitudes of V_{noise} = 20 and 80 mV, respectively. For V_{noise} = 20 mV in Fig. 6.3(b), the chaotic oscillations in the transition regions appear over a larger voltage interval than without any external

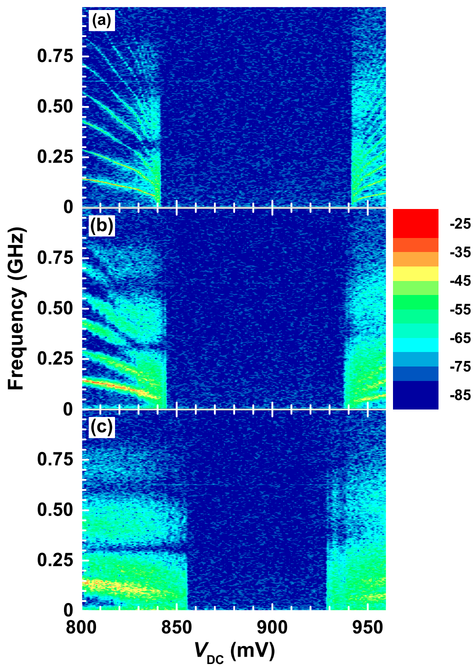

Figure 6.3: Measured frequency spectra of the current versus V_{DC} recorded between 800 and 960 mV (a) without noise, (b) with V_{noise} = 20 mV, and (c) with V_{noise} = 80 mV.

noise [cf. Fig. 6.3(a)]. The voltage region with no current oscillations becomes narrower. Increasing the noise amplitude to 80 mV results in a further shrinkage of the voltage region with no current oscillations, and the voltage range of seemingly chaotic oscillations extends to 855 and 929 mV as shown in Fig. 6.3(c). At the same time, the frequency spectra become broader with increasing noise amplitude. These experimental data clearly demonstrate that noise can significantly enhance the chaos generated in doped, weakly coupled SSLs. This was shown theoretically for the case of internal (shot and thermal) noise by the results of the numerical simulations in Ref. [5]. The present results show that chaos enhancement can also be achieved more generally by adding appropriate external noise.

Current traces as a function of time have been recorded for two noise amplitudes at $V_{\mathrm{DC}} = 939$ mV as shown in Fig. 6.4. Note that the current traces are recorded only with AC coupling so that the information about the DC current level is lost. For $V_{\mathrm{noise}} = 20$ mV, the current trace contains several irregularly spaced spikes as shown in Fig. 6.4(a). When the noise amplitude is increased to 80 mV, the current trace exhibits more spikes with somewhat smaller amplitudes as shown in Fig. 6.4(b). Similar current traces are observed for $V_{\mathrm{DC}} = 844$ mV (not shown). There are typically two oscillation

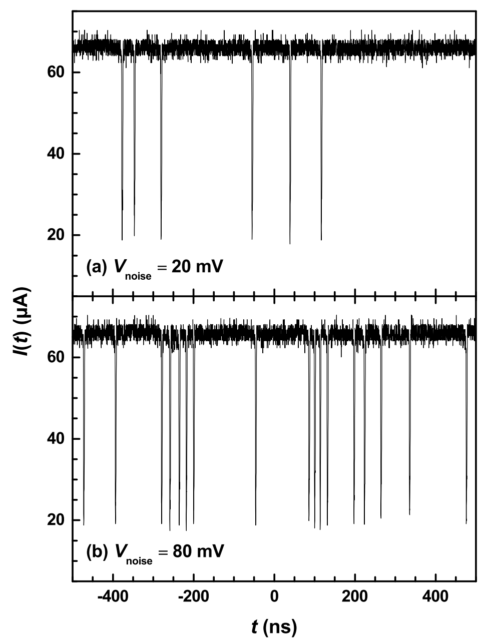

Figure 6.4: Measured current oscillations $I(t)$ recorded for different noise amplitudes (a) $V_{\mathrm{noise}} = 20$ mV and (b) $V_{\mathrm{noise}} = 80$ mV. V_{DC} was fixed at 939 mV.

modes present in doped, weakly coupled SSLs, the dipole motion mode and the well-to-well hopping mode. When the noise level is low, the dipoles are formed at the emitter moving toward the collector with a large interval of noise spikes. As the noise amplitude is increased, a continuous motion of the well-to-well hopping of the domain boundary occurs, introducing fast current oscillations in the SSL.

The power spectrum shown in Fig. 6.5(a) recorded at $V_{\mathrm{DC}} = 944$ mV clearly demonstrates that, even without any external noise, the doped, weakly coupled SSL can already exhibit a broad-band spectrum, indicating the possibility of the presence of chaotic oscillations even without external noise. When noise is added as in Fig. 6.5(b), the power spectrum becomes even broader. At the transition regions between periodic oscillations and no oscillations, the system appears with increasing external noise amplitude to exhibit a chaotic attractor, which leads to spontaneous chaos at room temperature. As predicted by the results of the numerical simulations reported in Ref. [5], internal noise enhances spontaneous chaos. The same effect of chaos enhancement is observed when we add external noise with increasing amplitude as will be further discussed below. At the same time, the frequency spectra in the periodic region are dominated by an oscillation with a single frequency, but with increasing bandwidth as the noise amplitude

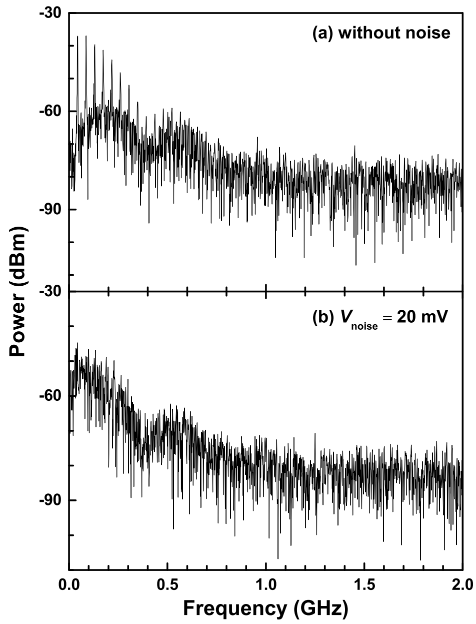

Figure 6.5: Measured frequency spectra recorded (a) without any external noise and (b) with $V_{\mathrm{noise}} = 20$ mV. V_{DC} was fixed at 944 mV.

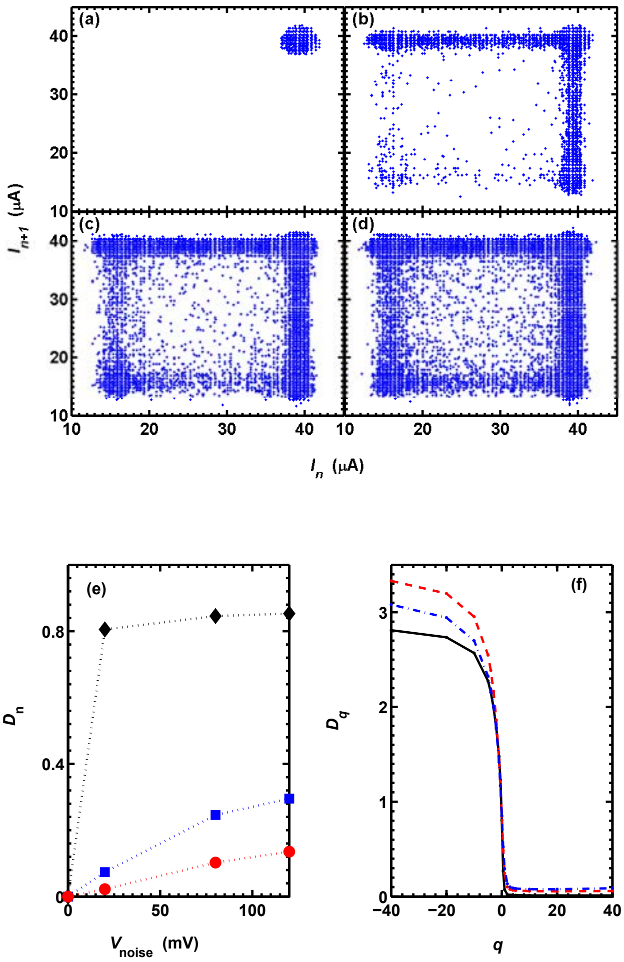

Figure 6.6: Poincaré maps extracted from experimental current traces versus time for (a) no external noise as well as with external noise of amplitude (b) $V_{\text{noise}} = 20$, (c) 80, and (d) 120 mV. (e) Values of the capacity dimension D_0 (diamonds), the information dimension D_1 (squares), and the correlation dimension D_2 (circles) as a function of V_{noise}. (f) Multifractal spectra. $V_{\text{noise}} = 20$ (solid line), 80 (dashed line) and 120 (dash-dotted line). V_{DC} was fixed at 845 mV.

is increased. Noise can significantly enhance the chaos generated in doped, weakly coupled SSLs.

6.2.4 Attractors obtained from experimental results

Figures 6.6(a), 6.6(b), 6.6(c), and 6.6(d) show reconstructed Poincaré maps from the experimental current traces versus time for no noise as well as

$V_{\text{noise}} = 20$, 80, and 120 mV, respectively, at $V_{\text{DC}} = 845$ mV. In the absence of external noise, the deterministic attractor is stationary, and the Poincaré map should consist of a single point. In Fig. 6.6(a), the unavoidable internal noise produces many points concentrated in a small region. When external noise is added, the Poincaré maps explore a region that becomes larger and fuller as the external noise amplitude increases as shown in Figs. 6.6(b), 6.6(c), and 6.6(d). Similar Poincaré maps are extracted from experimental current traces versus time at $V_{\text{DC}} = 940$ mV. Figure 6.6(e) shows the values of the capacity dimension D_0, the information dimension D_1, and the correlation dimension D_2 as a function of the external noise amplitude, which all increase with increasing noise amplitude. Without external noise, the SSL is in a stationary state with zero fractal dimension. When the external noise is turned on and increased, time-dependent oscillations appear, and the fractal dimension D_0 increases abruptly demonstrating evidence of chaotic oscillations induced by noise. Figure 6.6(f) shows the multifractal dimension for the different noise amplitudes. For large positive values of q, the fractal dimension D_q corresponds to regions of the attractor that are more often visited by the system trajectory and does not increase that much with external noise. For $q < 0$ and $|q|$ large, D_q is due to the least sampled regions of the attractor, and it increases more strongly when the external noise increases. We conclude that increasing the external noise expands the regions in phase space that are visited by the system trajectory, an effect that is obvious from the sequence shown in Figs. 6.6(b)–6.6(d).

6.3 Model and simulated results

6.3.1 Discrete resonant tunneling model

Numerical results are obtained using a discrete resonant tunneling model that captures the main features of doped, weakly coupled SSL [20, 27]. The model consists of dynamical equations describing the evolution of the variables such as the electric field $-F_i$ as well as the two-dimensional (2D) electron density n_i at well i, the tunneling current density $J_{i\to i+1}$ from well i to $i+1$, and the SSL total current density $J(t)$.

The numerical values of the parameters correspond to the experimental configuration described in Sec. 6.2 with an equivalent 2D doping density due to the doping of the central part of the quantum well of $N_D = 6\times 10^{10}$ cm^{-2}. The effective mass of the electrons in the GaAs/Al$_x$Ga$_{1-x}$As SSL is $m^* = (0.063 + 0.083x)m_e$, where m_e denotes the free-electron mass. The well and barrier widths are $l_w = 7$ and $l_b = 4$ nm, respectively, as for the experimentally investigated SSL so that the period of the SSL is $l = l_b + l_w = 11$ nm. The transversal area of the SSL is assumed to be $A = s^2$ with $s = 30$ μm. Finally, the relative permittivity of the SSL is $\epsilon = l/[l_w/\epsilon_w + l_b/\epsilon_b]$ with $\epsilon_w = 12.9\epsilon_0$ and $\epsilon_b = 10.9\epsilon_0$ referring to the relative permittivity of the well and barrier material, respectively. ϵ_0, $-e < 0$, k_B, T, and σ_0 denote the vacuum permittivity, the electron charge, Boltzmann's constant, the lattice temperature, and the contact conductivity, respectively.

Poisson equation in the superlattice reads,

$$n_i = N_D + \frac{\epsilon}{e}(F_i - F_{i-1}), \tag{6.1}$$

and together with charge continuity we get,

$$\epsilon \frac{dF_i}{dt} + J_{i\to i+1} = J(t), \tag{6.2}$$

expression relating the total current with electric field and tunneling current at well i. The overall voltage drop between the ends of the SSL $\sum_{i=1}^{N} F_i/l$ is equal to the DC voltage bias V_{DC}, while a noise voltage amplitude $\eta(t)$ is considered and corresponds to V_{noise}, both provided in the experiment by the function generator in Fig. 6.1,

$$\sum_{i=1}^{N} F_i = \frac{V_{\mathrm{DC}} + \eta(t)}{l}, \quad \eta(t) = \eta_{th}(t) + \eta_c(t), \tag{6.3}$$

where N denotes the number of periods of the SSL. Voltage noise $\eta(t)$ has two components: (i) $\eta_{th}(t)$, which is related to the intrinsic noise of the source, and (ii) the external noise $\eta_c(t)$. In addition, a linear approximation for the contact conductivity is considered,

$$J_{0\to 1} = \sigma_0 F_0, \quad J_{N\to N+1} = \sigma_0 \frac{n_N}{N_D} F_N. \tag{6.4}$$

Resonant tunneling currents are computed as,

$$J_{i\to i+1} = \frac{en_i}{l} v^{(f)}(F_i) - J^{-}_{i\to i+1}(F_i, n_{i+1}, T), \tag{6.5}$$

$$J^{-}_{i\to i+1}(F_i, n_{i+1}, T) = \frac{em^* k_B T}{\pi\hbar^2 l} v^{(f)}(F_i) \ln\left[1 + e^{-\frac{eF_i l}{k_B T}}\left(e^{\frac{\pi\hbar^2 n_{i+1}}{m^* k_B T}} - 1\right)\right], \tag{6.6}$$

where the forward electron velocity $v^{(f)}(F_i)$ is a function with peaks corresponding to the discrete energy levels in every well calculated using a

Table 6.1: Values of the potential barrier V_{barr} and the first three energy levels E_1, E_2, and E_3 for the doped, weakly coupled GaAs/$\mathrm{Al}_{0.45}\mathrm{Ga}_{0.55}$As SL.

V_{barr} (meV)	E_1 (meV)	E_2 (meV)	E_3 (meV)
388	45	173	346

Kronig-Penney model for the investigated SSL configuration as summarized in Tab. 6.1. Specifically, $v^{(f)}$ takes the form,

$$v^{(f)}(F_i) = \sum_{j=1}^{n} \frac{\frac{\hbar^3 l(\gamma_{C1}+\gamma_{C_j})}{2m^{*2}} \mathcal{T}_i(\epsilon_{C1})}{(\epsilon_{C1} - \epsilon_{C_j} + eF_i l)^2 + (\gamma_{C1} + \gamma_{C_j})^2}, \tag{6.7}$$

$$\mathcal{T}_i(\epsilon) = \frac{16k_i^2 k_{i+1}^2 \alpha_i^2 (k_i^2 + \alpha_i^2)^{-1} (k_{i+1}^2 + \alpha_i^2)^{-1}}{(l_w + \alpha_{i-1}^{-1} + \alpha_i^{-1})(l_w + \alpha_{i+1}^{-1} + \alpha_i^{-1}) e^{2\alpha_i l_b}}, \tag{6.8}$$

$$\hbar k_i = \sqrt{2m^*\epsilon}, \quad \hbar k_{i+1} = \sqrt{2m^*(\epsilon + elF_i)}, \tag{6.9}$$

$$\hbar\alpha_{i-1} = \sqrt{2m^*\left[eV_B + e\left(l_b + \frac{l_w}{2}\right)F_i - \epsilon\right]}, \tag{6.10}$$

$$\hbar\alpha_i = \sqrt{2m^*\left[eV_B - \frac{el_wF_i}{2} - \epsilon\right]}, \tag{6.11}$$

$$\hbar\alpha_{i+1} = \sqrt{2m^*\left[eV_B - e\left(l_b + \frac{3l_w}{2}\right)F_i - \epsilon\right]}. \tag{6.12}$$

where ϵ_{C_j} stands for the position of the j energy level at every quantum well and γ_{C_j} stands for its energy broadening due to scattering. A detailed derivation of these expressions can be found in references [21, 27].

The contact conductivity σ_0 is derived from a linear approximation of the emitter current density $J_{0\to1}$, which depends on the structure of the contact. We use $\sigma_0 = 0.763$ A/(V m), which qualitatively reproduces the experimental current-voltage characteristic shown in Fig. 6.2 for a barrier height $V_{\mathrm{barr}} = 388$ meV.

In the simulations, the thermal noise $\eta_{th}(t)$ is simulated by picking random numbers every 5×10^{-11} s from a zero mean distribution with a standard deviation of 1.6×10^{-3} V. The external noise $\eta_c(t)$ is simulated by picking random numbers every 5×10^{-9} s from a zero mean distribution with a tunable standard deviation.

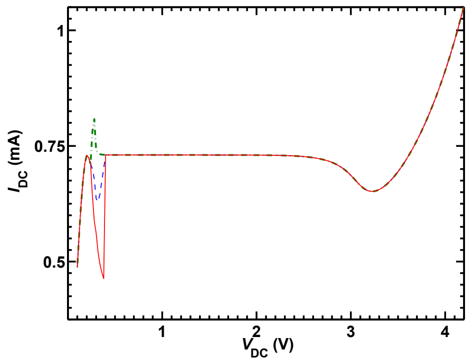

Figure 6.7: Results of the numerical simulations of the current I_{DC} versus voltage V_{DC} for $\sigma = 0.763$ A/(V m). The dash-dotted, the dashed, and the solid line correspond to the maximum, mean, and minimum current, respectively. In the voltage region between 0.26 and 0.4 V, current oscillations occur. The simulated curves are shifted to lower voltages compared with the experimental curve due to built-in fields and a voltage drop at an external resistance. Nevertheless, the oscillatory region is qualitatively similar to the one found in the experiments as shown in Fig. 6.2.

6.3.2 Results of numerical simulations

Figure 6.7 depicts the simulated current-voltage characteristic for the deterministic equations of our model [$\eta(t) = 0$)]. The mean current (dashed line) should be compared with the experimental one in Fig. 6.2. The average current for voltages at which there are current oscillations in Fig. 6.7 is qualitatively similar to the first part of Fig. 6.2. There is a shift between the theoretical and experimental curves due to the built-in voltage and a voltage drop at an external resistance that are absent in our model equations. In the experiment, there is a voltage region of stationary current between two regions of current oscillations. This window of stationary currents is absent in the simulations of our model. However, the end of the first voltage region with current oscillations in Fig. 6.2 is similar to the end of the voltage region with current oscillations in Fig. 6.7.

Figures 6.8(a), 6.8(b), 6.8(c), and 6.8(d) show the results of the numerical simulations for the current oscillations for different noise amplitudes (a) $V_{\mathrm{noise}} = 1$ (only thermal noise is present), (b) 8, (c) 33, and (d) 46 mV, respectively, at $V_{\mathrm{DC}} = 380$ mV, which lies in the oscillatory region of the current-voltage curve presented in Fig. 6.7. The internal and external noise are numerically generated as explained above. With increasing V_{noise}, the oscillations become less periodic, contain more spikes in the same time interval, and the amplitude becomes more and more irregular. The corresponding frequency spectra as determined by a numerical Fourier transform are displayed in Fig. 6.8(e), 6.8(f), 6.8(g), and 6.8(h), respectively. The number of peaks in the frequency spectra decreases with increasing noise amplitude, while the width of the frequency spectra increases. We have repeated the simulations for a voltage of 460 mV, for which the deterministic system is in a stationary state. The behavior with increasing noise amplitude is very similar to the one shown in Figs. 6.8(b)–6.8(d) with some differences in the details of the current oscillations and frequency spectra. In comparison to Fig. 6.8(a), it looks of course different, because there are no current oscillations in this case. Overall, the experimental trend with increasing noise amplitude is reproduced, i. e., the larger the controlled noise amplitude, the more random the current oscillations become. Note that simulations of the field distribution (not shown) indicate that the current spikes in the simulated current traces in Figs. 6.8(a)–6.8(d) are caused by the generation of a small charge dipole, which is generated at the emitter contact and moves toward the collector contact. When the front part of the dipole reaches the collector contact, it disappears, while the back part of the dipole rebuilds the domain wall, which existed before the current spike.

We have also constructed phase portraits from the calculated electric field in well number 47 versus well number 3. We can build alternative Poincaré maps based on the intersection of the trajectories in these phase portraits with an appropriate segment of a straight line. Period doubling scenarios or quasi-periodic attractors could be visualized using such Poincaré maps. Thus, these phase portraits give information on the chaotic state of the system. Figures 6.9(a), 6.9(b), 6.9(c), and 6.9(d) show the phase portraits for different noise amplitude (a) $V_{\text{noise}} = 1$, (b) 8, (c) 33, and (d) 46 mV, respectively, at $V_{\text{DC}} = 380$ mV, which lies in the oscillatory region of the current-voltage curve presented in Fig. 6.7 and corresponds to the simulated data in Fig. 6.8. When only *thermal* noise is present [cf. Fig. 6.9(a)], the oscillations are periodic, even though they are somewhat distorted by noise. However, when controlled noise is added as shown in Figs. 6.9(b)–6.9(d), the oscillations loose their periodicity and become more and more distorted with increasing noise amplitude, i. e. the complexity of the phase portraits strongly increases, indicating increasing chaotic behavior. The phase portraits for a voltage of 460 mV (not shown), for which the deterministic system is in a stationary state, look qualitatively very similar to the ones shown in Fig. 6.9, except for the first one with only *thermal* noise, because there are no current oscillations in this case. Note that the *thermal* noise does not distort the periodicity, since it only introduces some small fluctuations. However, by introducing a

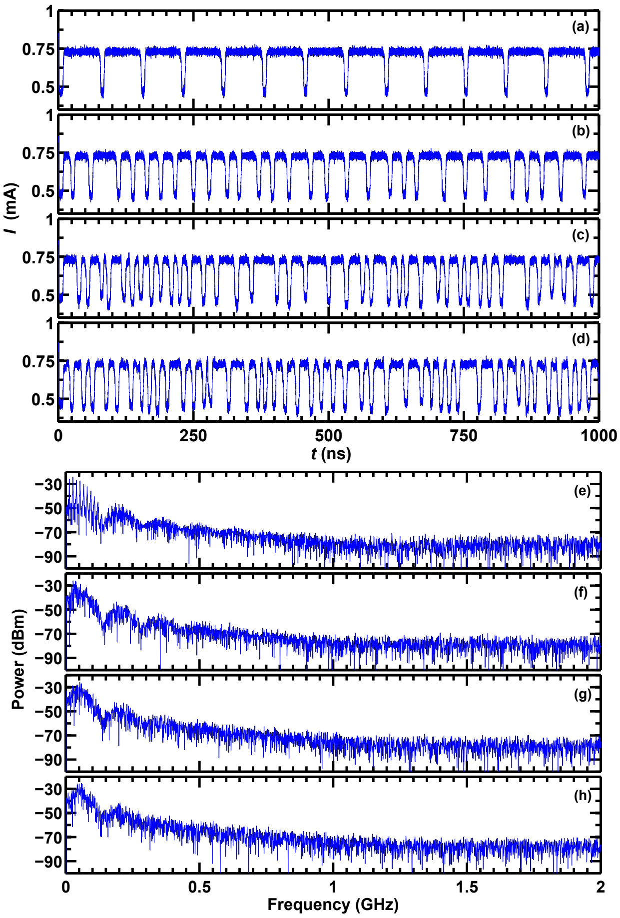

Figure 6.8: Results of the numerical simulations for the current oscillations $I(t)$ for different noise amplitude (a) $V_{\text{noise}} = 1$, (b) 8, (c) 33, and (d) 46 mV at $V_{\text{DC}} = 380$ mV in the oscillatory region of the current-voltage characteristics presented in Fig. 6.7. The corresponding frequency spectra as determined by a numerical Fourier transform are shown in (e), (f), (g), and (h), respectively.

longer time-correlated (*controlled*) noise, clear chaotic behavior is obtained.

6.4 Summary and conclusions

We have observed that the external noise can induce spontaneous chaotic oscillation in a narrow voltage interval in a doped, weakly coupled GaAs/AlAs SSL at room temperature. Results of numerical simulations of nonlinear transport based on a discrete tunneling model qualitatively confirm the experimentally observed features. While in a noise-free SSL static domain boundaries are formed, the domain boundary moves into the collector, new domain walls are formed near the emitter, and chaotic current oscillations are induced, when noise is added. Therefore, with increasing noise amplitude, chaotic current oscillations can be enhanced in semiconductor superlattices. This approach is consequently a very robust method of producing chaotic current oscillations in doped, weakly coupled semiconductor superlattices.

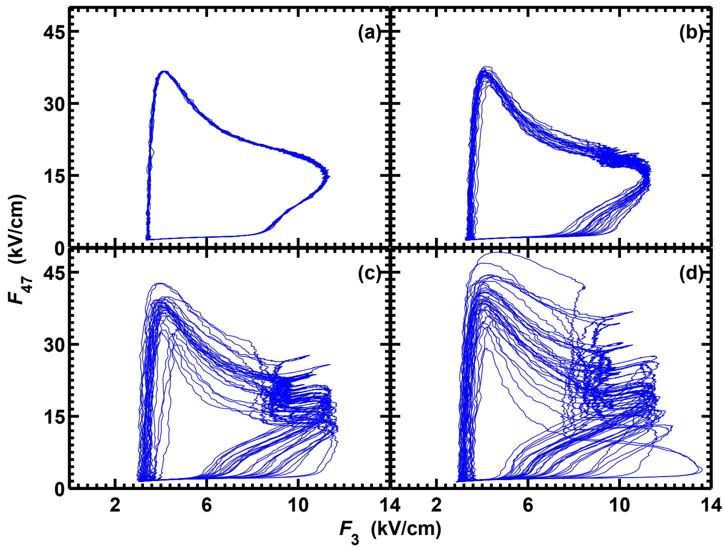

Figure 6.9: Results of the numerical simulations for the phase portraits, where the electric field in well number 47 is presented versus the electric field in well number 3. The noise amplitude increases from (a) $V_{\text{noise}} = 1$, (b) 8, (c) 33, to (d) 46 mV at $V_{\text{DC}} = 380$ mV in the oscillatory region of the current-voltage characteristics presented in Fig. 6.7. Loops correspond to oscillations depicted in Fig. 6.8.

Chapter 7

Enhancing Chaotic Behavior at room temperature in GaAs/(Al,Ga)As Superlattices

7.1 Introduction

Two different time scales are involved in the dynamics of SSLs. The inter-site tunneling and inter-subband relaxation processes occur on much shorter timescales than the dielectric relaxation processes [26, 28]. Therefore, the long timescale dynamics of semiconductor lasers [131] and superlattices [5, 27] are typically modeled using semiclassical equations, while the short timescale processes are treated stochastically. In weakly coupled GaAs/AlAs superlattices, chaos driven by ac voltage bias was predicted [36] and observed in experiments [96] at ultralow temperatures in the 1990s. Spontaneous chaos was also observed in 1996 experiments [148]. Different oscillation types were observed and also abrupt transitions from periodic to chaotic oscillations. However, simulations based on the sequential tunneling model failed to find spontaneous chaos for the same superlattice configurations. For much longer superlattices (100 periods), numerical sumulations showed spontaneous chaos based on the period doubling route [6]. Recently, Huang *et al.* have argued [75] that phonon-assisted transport though the X-valley of AlAs allows a thermal distribution of carriers to diffuse through the SSL. This $\Gamma - X$ electron transfer mechanism eliminates self-sustained oscillations and spontaneous chaos at higher temperatures. When the concentration of Al at the barriers is 45%, the Γ and X minima have the same energy. Then the X level energy is the same as the barrier height between wells and there is no $\Gamma - X$ transfer, see section 1.2.1. They subsequently observed current

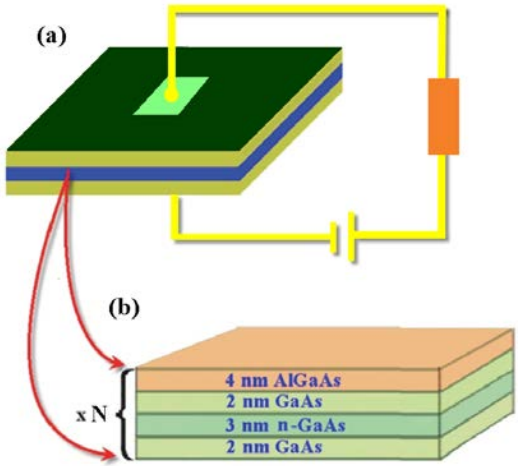

Figure 7.1: Simplified image of a semiconductor superlattice. A external voltage is applied between the contacts at the top and bottom of the device, which consists of N periods of GaAs/Al$_x$Ga$_{1-x}$As. The 7nm GaAs wells are divided into three zones to prevent doping diffusion.

self-oscillations and spontaneous chaos in dc-biased 50-period SSLs at room temperature for the first time [74, 75]. Weak noise-enhanced chaos has been found in simulations for 50-periods SSL [5], which opened the way to new perspectives that could optimize the chaotic behavior in SSLs.

In this chapter, we investigate the behavior of the sequential resonant tunneling (SRT) model, discussed in section 6.3 of previous chapter, for shorter SSLs at room temperature and without noise. We consider two different barrier heights corresponding to an Aluminum content of 45% (as in recent experiments [74, 75]) and a different concentration of 70% to study the possible effect of increasing the barrier height on the dynamical behavior. We observe a period doubling route to chaos on wide voltage intervals for a 10-period SSL. Moreover, the chaotic self-oscillations occur at much higher frequencies for these shorter superlattices, increasing the possible rate of random number generation. The outline of the chapter is as follows. The results of our numerical simulations are reported in section 7.2, and a discussion of our results is contained in section 7.3.

7.2 Results

We analyze the sequential resonant tunneling model of 10-period semiconductor superlattices such that GaAs/Al$_{0.7}$Ga$_{0.3}$As and GaAs/Al$_{0.45}$Ga$_{0.55}$As

T (K)	N_D (cm^{-2})	l_b (nm)	l_w (nm)	s (μm)
295	6×10^{10}	4	7	60

V$_{barr}$ (meV)	E$_1$ (meV)	E$_2$ (meV)	E$_3$ (meV)
600	53	207	440
388	45	173	346

Table 7.1: (Top) The design parameters of the superlattice. (Bottom) Values of the potential barrier and energy levels for GaAs/$Al_{0.7}Ga_{0.3}As$ and GaAs/$Al_{0.45}Ga_{0.55}As$ superlattices, first and second row, respectively. In the simulations the value of the contact conductivity has been taken to reproduce the experimental results with $N = 50$: $\sigma_0 = 0.783$ A/Vm for $V_{barr} = 388$ meV ($x = 0.45$) and $\sigma_0 = 0.06$ A/Vm for $V_{barr} = 600$ meV ($x = 0.7$), where V_{barr} is the height of the barrier [5, 75].

are considered, using the material parameters indicated in table 7.1. Equations described in section 6.3 are evolved in time for $t_f = 200$ ns using the forward Euler method. We remove the transient behavior due to the initial conditions by discarding first $t_i = 100$ ns of evolution at each bias voltage. Bifurcations are detected via the Poincaré map, which is depicted in Figures 7.3 and 7.4. First, the time-evolution is projected onto a two-dimensional slice through phase space, in this case, the F_4-F_6 plane was used. When $F_4(t)$ passes through its center value, and, in order to sample the trajectory only once per cycle, $\dot{F}_4(t^*) < 0$, the time t^* and the values of $F_6(t^*)$ and $\dot{F}_6(t^*)$ are stored. These sets of values form $\mathcal{P}F_6$ and $\mathcal{P}\dot{F}_6$.

The Poincaré map transforms the continuous time evolution in the $2N+1$-dimensional phase space (electric fields, electron densities and total current density) into a discrete map from a one-dimensional interval into itself [43]. Both, a stationary state and a periodic orbit will appear as a fixed point of the Poincaré map. A period-doubling bifurcation is identified when one-cycles transition to two-cycles. Chaotic regions are identified where a proliferation of period-doubling bifurcations yields fractal structure in the bifurcation diagram.

We support our analysis of the Poincaré map by comparing our conclusions against the power spectrum

$$P[J](f) = \left| \int_{t_i}^{t_f} dt\, e^{-i2\pi f t} J(t) \right|^2, \tag{7.1}$$

where f is the frequency. As in the Poincaré map, different spectra are associated with different dynamical structures: (a) periodic orbits correspond to a series of peaks with widths of the same order as the frequency bin size,

POWER SPECTRA AND BIFURCATION DIAGRAM

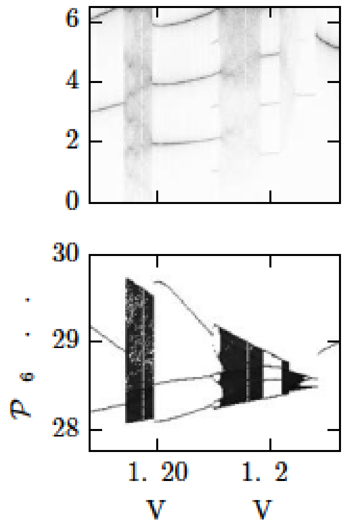

Figure 7.2: Power spectrum and bifurcation diagram for a 10-period GaAs/$Al_{0.45}Ga_{0.55}As$ SSL, in a voltage region where chaotic behavior is present. (Top row) The power spectrum of $J(t)$ plotted against the bias voltage. (Bottom row) The bifurcation diagram, plotting the Poincaré map against the bias voltage.

falling at integer multiples of the fundamental frequency, (b) period doubling bifurcations are recognized when the number of peaks in the spectrum changes by a factor of two, and a new peak appears in the power spectrum at half the fundamental frequency, (c) strange attractors have broadband spectra. These spectra may contain both sharp and broad peaks.

Figure 7.2 shows a voltage region where deterministic chaotic behavior is present in the simulations for the 10-period GaAs/$Al_{0.45}Ga_{0.55}As$ SSL, see Table 7.1. In contrast with the $N = 50$ case for the same aluminum content, there are observable windows of strong chaotic behavior, whereas chaotic dynamics for $N = 50$ appeared within very narrow voltage windows and were so weak that they became observable only by the addition of stochastic terms to the evolution equations that enhanced chaos [5]. Moreover, the simulations show that the lowest harmonic can reach frequencies up to 25 GHz, at least one order of magnitude higher than those observed in the 50-period SSLs.

The bifurcation diagram for the 10-period GaAs/$Al_{0.7}Ga_{0.3}As$ SSL, see Table 7.1, is presented in Figure 7.3, and several phase portraits are presented in Figure 7.4. Voltage windows where chaotic behavior is present are one

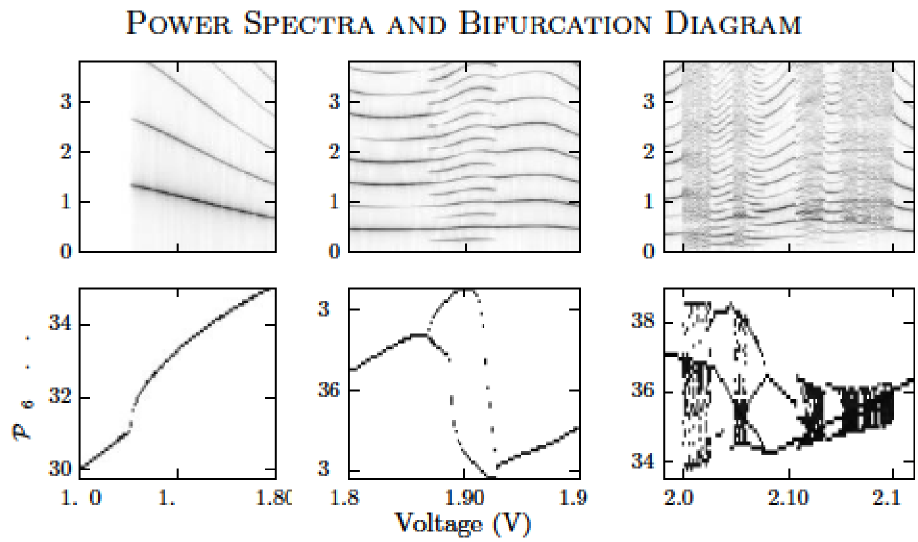

Figure 7.3: Power spectrum versus voltage and bifurcation diagrams for a 10-period GaAs/$Al_{0.7}Ga_{0.3}As$ SSL and different voltage regions. (Top row) Power spectrum of $J(t)$ versus voltage. (Bottom row) Bifurcation diagram of Poincaré map versus voltage. The Hopf bifurcation from the steady state is shown in the first column. A period doubling "bubble" is shown in the second column. A period-doubling cascade is shown in the third column.

order of magnitude wider than in the previous case, Figure 7.2. Combining the bifurcation diagram, power spectra and phase portraits of Figures 7.3 and 7.4, we characterize the dynamical instabilities of the SRT model for $N = 10$. At low voltages, $J(t)$ approaches a steady state. We observe the following bifurcations:

Supercritical Hopf bifurcation. In the leftmost column of Figure 7.3, we observe a transition from stationary state to periodic orbit. Subsequently, we observe a circle in the phase portrait at the top row of Figure 7.4, and the power spectrum contains peaks falling at integer multiples of a fundamental oscillation frequency.

Period doubling bifurcation. In the second column of Figure 7.3 and the second row of Figure 7.4, we observe a transition from one-cycles to two-cycles in the Poincarè map, so that a new peak in the power spectrum appears at half of the former fundamental frequency.

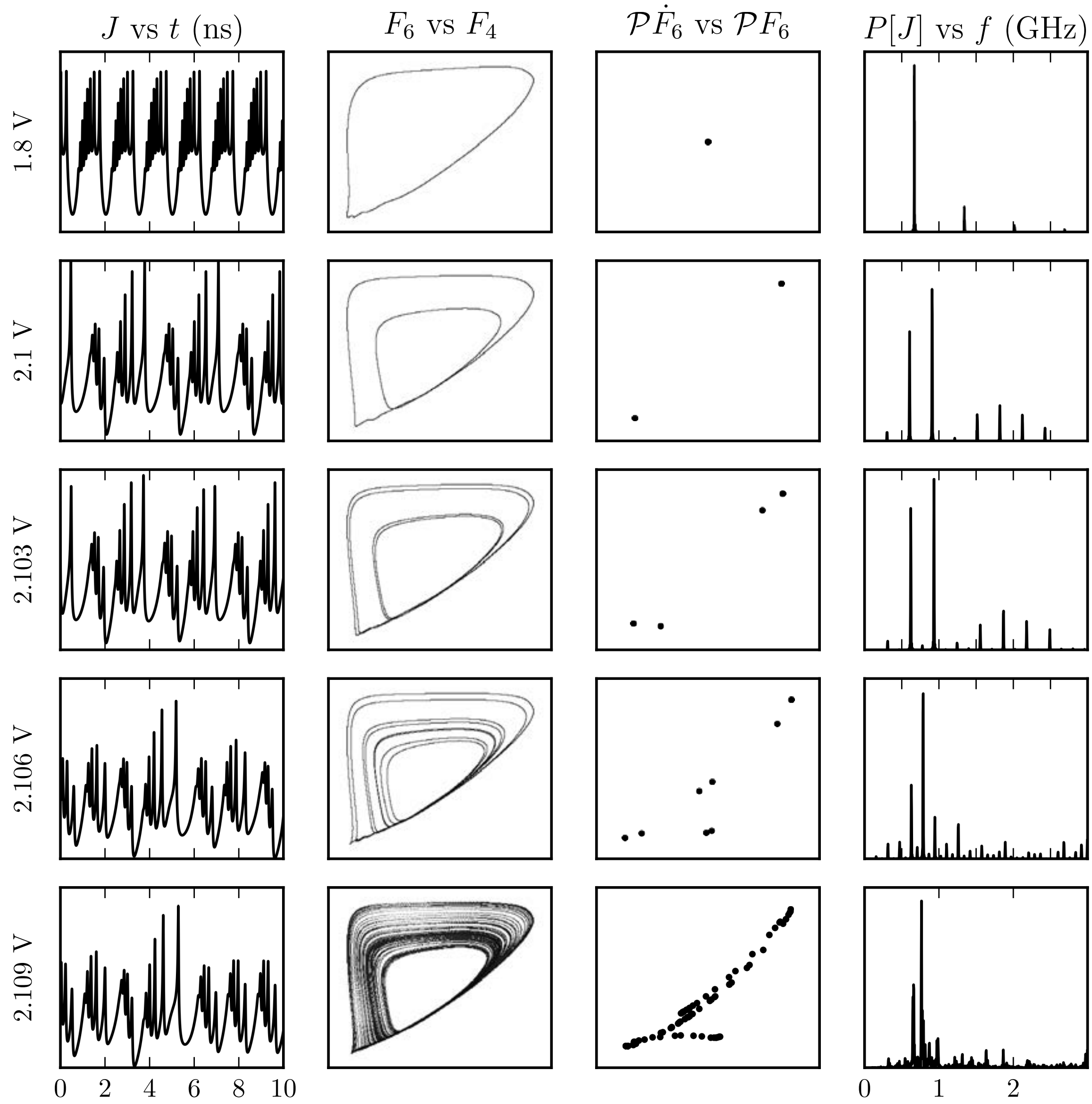

Figure 7.4: Representative phase portraits for the 10-period GaAs/$Al_{0.7}Ga_{0.3}As$ SSL. The first column shows the average current J plotted against time t. The second column shows the phase portrait $F_6(t)$ plotted against $F_4(t)$. The third column shows the Poincare map $\mathcal{P}\dot{F}_6(t^*)$ plotted against $\mathcal{P}F_6(t^*)$. The last column shows the power spectrum of $J(t)$. A periodic oscillation is shown in the first row. The period-doubling cascade to a chaotic attractor is shown in the bottom four rows.

Period doubling cascade. The period doubling of the periodic orbit continues into a period-doubling cascade, resulting in a strange attractor. In particular, we have determined the first Feigenbaum constant with less than 1% error. The rightmost column of Figure 7.3 and the bottom three rows of Figure 7.4 illustrate the period-doubling cascade. Based upon the emergence of a broad peak between the two strongest harmonics, we conclude that the invariant manifold is a strange attractor.

7.3 Conclusions

This work predicts that 10-period semiconductor superlattices (SSLs), in contrast with the 50-period SSLs typically used in experiments, exhibit a more robust intrinsic deterministic chaotic behavior with faster self-sustained current oscillations. In the same direction, to increase the voltage barrier height (through increasing the aluminum content) also enhances the chaotic behavior. The deterministic chaos found in simulations of the sequential resonant tunneling (SRT) model is characterized as a Feigenbaum period doubling cascade to chaos. These results open the possibility to create faster random number generators using these shorter superlattices.

We associate the bifurcations described in Section 7.2 with several potential applications. First, the Hopf bifurcation leads to nonlinear oscillations involving superharmonic frequencies reaching several tens of GHz. Hence these SSLs could be used as solid-state sources of electromagnetic radiation. Secondly, the half frequency found at the period doubling "bubble," see the middle column of Figure 7.3, could be used to compress information into a desirable frequency range or to squeeze out of it undesirable noise [67].

The SRT model has proven to robustly describe the essential behavior of SSLs over a wide parameter range, hence we put forward that the dynamical instabilities described in this work are the main mechanism triggering the experimentally observed chaos in SSLs. In addition, it is important to note that intrinsic quantum entropy sources are not taken into account in this work. In the real system, these quantum fluctuations are amplified by the deterministic dynamics, enabling the construction of true RNG [21, 101].

Concluding remarks

This thesis brings together part of the results obtained from fall 2013 to the summer of 2017. Our main efforts have been focused on understanding the physics behind mechanical properties of graphene. Nonetheless, the appearance of new experiments that showed chaotic behavior of semiconductor superlattices working at room temperature spurred our interest in these systems.

Rippling and buckling of graphene monolayers

Rippling and buckling of suspended graphene monolayers are reminiscent of some coupling between elastic deformations of the membrane and internal degrees of freedom, possibly, as proposed by [70, 139], charge carrier density fluctuations. Regardless the nature of the internal degrees of freedom coupled to the membrane deformations, an unloaded membrane, clamped and only under elastic energy would remain flat, let alone discussions about the stability of crystal order in 2-D [88].

Simple spin-string or spin-membrane models presented in chapters 2, 3 and 4 capture the main mechanical features of suspended graphene monolayers. This simple approach, where atomic vertical displacements are coupled to Ising spins (modelling some internal degrees of freedom), enables a detailed study of the phase diagram as well as the out-of-equilibrium dynamics of the system.

- Chapter 2 analytically derives the main properties of the phase diagram of the spin-string (1-D) model, once spin degrees of freedom are integrated out. It presents first and second order phase transitions, which are used in chapter 4 to emulate the STM driven transition from rippled to buckled graphene. A detailed explanation of the main features of the phase diagram is provided. Besides, a numerical integration of the Euler-Lagrange equations is carried out, which produces the string profiles and the corresponding order parameters for the different phases.

- The existence of static ripples on graphene monolayers motivates the extension of the spin-string model to a two-dimensional hexagonal lattice in chapter 3. Therein, and similarly to the one-dimensional model, the out-of-plane displacements are coupled to Ising spins, which also have a nearest-neighbour interaction. In addition, next-nearest-neighbor spin interactions are taken into account. Starting from random initial conditions, we look for the stable states that the system attains in the long time limit. A phase diagram for low temperatures is displayed, which shows different rippling patterns depending on the value of the spin-spin interactions. This proves that this simple model shows an ample range of experimentally observed rippling patterns, suggesting that a proper first-principles approach for suspended graphene monolayers may be reducible to this (or a similar) model. The phase diagram also includes a buckled phase, which makes it possible the appearance of a rippled to buckled phase transition.

- In chapter 4, the 2-D spin-membrane model derived in chapter 3 is used to explain recent experiments where STM drives a transition from rippled to buckled graphene [102, 130].We show the existence of stable and metastable buckled states, reminiscent of the phases in the phase diagram for the 1-D model, analyzed in chapter 2. Modelling the STM-graphene interactions as a current-dependent temperature plus an external field for the spins, qualitative results equivalent to the experimental ones are found. Starting from a metastable rippled state at low temperature, the interaction with the STM increases the temperature driving the system to the stable buckled state. This transition could also be driven by a electrostatic or mechanical interaction, instead of a temperature change, which can also be reproduced by our model.

The rich phenomena observed in the spin-membrane model, and its concordance with experimental results, supports the election of elastic models coupled with internal degrees of freedom to understand the mechanics of suspended graphene monolayers.

Chapter 5 deals with a first-principle model [70] to understand rippling in suspended graphene. Elastic energy for the membrane, with stretching and bending terms, is considered. Energy terms for charge carriers in graphene (free Dirac fermions), Coulomb interaction and coupling between charge density fluctuations and the strain tensor are also included.

The complexity of the model does not allow us to derive either the out-of-equilibrium dynamics or a complete phase diagram, as we have done in the spin-membrane model. However, the inclusion of boundary conditions not considered in [70] enables a linear stability analysis approach that helped us pinpoint the bifurcation where the flat solution becomes unstable. Considering two different boundary conditions, free and clamped, different critical radii at room temperature are obtained. Below these critical radii, which are in the nanometric range, the flat solution is stable, whereas different critical modes bifurcate for larger membranes. The combination of many of these modes for micrometric membranes would give rise to the experimentally observed ripples.

We hope our work may help to better understand the phenomenology observed in the mechanics of suspended graphene monolayers. Nevertheless, there are still opened questions to address regarding these issues.

- Spin-membrane models have been extensively studied during this work. Even though the main features for the 1-D case have been analytically derived and the 2-D case has been numerically studied, there are still potential results to find out. The agreement between mechanical graphene phenomenology and this model with clamped boundary conditions (BC) could be complemented with periodic boundary conditions. Comparison between the spin-membrane model with periodic BC for two sides and carbon nanotubes would add more insight in the relation of this model with real systems. In addition to that, a derivation of this model from a first-principles approach is missing and would be greatly desirable.

- Even when the addition of boundary conditions to the first-principles model studied in chaper 5 has proven to be essential for the linear stability analysis that can explain the instability of the flat solution, more work is still necessary. The BCs were imposed over the results of Guinea *et al.* [70] and a consistent derivation of the same results taking into account the BC from the beginning is necessary. This could quantitatively modify our results, although we do not expect them to be qualitatively different. A discrete model, where a lattice instead of a continuous space is used, can also be useful to impose the boundary conditions in a more consistent way and to conserve the intrinsic discrete nature of graphene, which could bring new phenomenology.

Chaotic behavior in semiconductor superlattices

The main purpose of chapters 6 and 7 is to characterize the chaotic behavior of SLs and to find out some ways to enhance it, which could be applied to the generation of true random numbers.

- Chapter 6 presents theoretical and experimental results where a source of external noise is used to enhance the chaotic behavior of semiconductor superlattices. The dynamical behavior of the system depends on the external applied voltage V, which is taken very close to an infinite period bifurcation V_b. For $V < V_b$ the current is periodically oscillating whereas for $V > V_b$ the current is constant. Adding amplitude-controlled noise to the voltage source produces seemingly chaotic behavior. Theoretical and experimental results qualitatively agree, opening the possibility of true random number generation using this setup.

- To better understand the way to use semiconductor superlattices as true random number generators, chapter 7 addresses the existence of deterministic chaos, and the route to it. Studying a sequential resonant tunneling model describing electron transport in semiconductor superlattices, a period doubling cascade to chaos is found. It is also observed that the reduction of the number of wells or the increase of Aluminum quantity in the barriers greatly enhance the deterministic chaotic behavior. Entropy sources are not taken into account in this model, such as quantum uncertainty in the resonant tunneling currents. In the real system, the deterministic chaos acts as an amplifier of these quantum uncertainties, opening the possibility of true random number generation.

We do believe that semiconductor superlattices can be a feasible candidate for fast generation of true random numbers. Their possible competitiveness against other random sources as chaotic laser reside in its scalability, what would enable them to be included in micrometric circuits. Nevertheless, to accomplish a full understanding of their behavior more work is necessary:

- Even when the sequential resonant tunneling model have proven to be a reliable selection for modelling SSL behavior in multiple occasions, [27], some features could be studied in more detail. Specifically, the linear approximation of the contact conductivity could be modified to account for more realistic effects. In addition, inhomogeneities in the quantum well and barrier properties could also be considered.

- The improvement of the understanding of the contact physics as well as a better fitting of all the parameters appearing in the model (miniband energies, broadening ...) would improve the prospect for proposing new device configurations that would work in experiments as desired.

- We think it is worth trying to experimentally enhance the chaotic behavior of SLs using the approaches explained in chapter 7. Decreasing the number of wells, or increasing the Aluminium quantity in the barriers (while decreasing the contact conductivity), are two possibilities that should translate in greater chaotic behavior.

Part III

Appendix

Appendix A

Appendices for chapter 2

A.1 Stability of the low temperature string profiles

At low temperatures $\theta \to 0^+$, the Euler-Lagrange equation becomes equivalent to

$$\frac{1}{\pi^2}u'' + \mathrm{sgn}(u)\eta(|u| - 2\kappa) = 0, \qquad u(0) = u(1) = 0. \tag{A.1}$$

We focus on the solution of the Euler-Lagrange equation with no internal nodes, which is [123]

$$u^{(0)}(x) = \pm \begin{cases} \frac{\pi^2}{2}(1 - 2x_0)x, & x < x_0, \\ 2\kappa + \frac{\pi^2(x-x_0)(1-x_0-x)}{2}, & x_0 < x < 1 - x_0, \\ \frac{\pi^2}{2}(1 - 2x_0)(1 - x), & x > 1 - x_0. \end{cases} \tag{A.2}$$

The parameter x_0 is obtained by imposing that $u_0(x)$ is continuous at x_0 (or $1 - x_0$), that is,

$$\frac{\pi^2}{2}x_0(1 - 2x_0) = 2\kappa, \tag{A.3}$$

which has two solutions, symmetrical with respect to $1/4$, $x_{0,1} < 1/4 < x_{0,2}$, as given by Eq. (2.22), provided that $\kappa < \kappa_M^{(0)} = \pi^2/32$. For $\kappa = \kappa_M^{(0)}$, it is $x_{0,1} = x_{0,2} = 1/4$, and for $\kappa > \kappa_M^{(0)}$, there are no buckled solutions.

In order to analyse the local stability of the buckled solutions with $x_{0,1}$ and $x_{0,2}$, we have to linearise the Euler-Lagrange equation around $u^{(0)}(x)$, that is, we write

$$u(x) = u^{(0)}(x) + \Delta u(x). \tag{A.4}$$

For parity reasons, the stability results are the same for the two possible signs in Eq. (A.2), and thus we carry out this analysis for the solution with the plus sign. Then, the linearised equation is

$$\frac{1}{\pi^2}\Delta u'' + \delta(u^{(0)}(x) - 2\kappa)\Delta u = 0. \tag{A.5}$$

According to the stability conditions described in Sec. 2.2.1, we have to solve the above equation with the boundary conditions

$$\Delta u(0) = \Delta u(a) = 0, \quad a \leq 1. \tag{A.6}$$

If Eqs. (A.5) and (A.6) has only the trivial solution $\Delta u(x) \equiv 0$ for any $a \leq 1$, $u^{(0)}(x)$ is stable, if there is a non-trivial solution for some $a < 1$, $u^{(0)}(x)$ is unstable.

Equation (A.5) tells us that $\Delta u(x)$ is composed of straight lines, the slopes of which have jumps at the points $x_J = x_0$ or $1 - x_0$, where $u^{(0)}(x) = 2\kappa$. The change of slope is obtained by integrating Eq. (A.5) in a narrow interval around these points, which gives the result

$$\Delta u'(x_J^+) - \Delta u'(x_J^-) = -\frac{2}{1-2x_0}\Delta u(x_J), \tag{A.7a}$$

in which x_J can be equal to either x_0 or $1 - x_0$. Now we proceed to seek non-trivial solutions of the linearised equation (A.5), which allows us to choose the initial slope $\Delta u'(0) = 1$ [62]. Then, $\Delta u(0^+) > 0$ and the stability of $u^{(0)}(x)$ can be elucidated by looking at $\Delta u(1)$: if $\Delta u(1) < 0$, it means that $\Delta u(x)$ vanishes at some intermediate point $a \leq 1$ and the profile $u^{(0)}(x)$ is unstable.

Let us denote by c_2 and c_3 the slopes of $\Delta u(x)$ in the intervals $(x_0, 1-x_0)$ and $(1 - x_0, 1)$, respectively. As stated above, the initial slope is $c_1 = 1$ in the interval $(0, x_0)$. By using Eq. (A.7), we readily obtain that

$$c_2 = c_1\frac{1-4x_0}{1-2x_0}, \qquad c_3 = -c_1, \tag{A.8}$$

which entails that

$$\begin{aligned} \Delta u(x_0) &= c_1 x_0, \quad \Delta u(1-x_0) = c_1(1-3x_0), & \text{(A.9a)} \\ \Delta u(1) &= c_1(1-4x_0). & \text{(A.9b)} \end{aligned}$$

On the one hand, if $x_0 > 1/4$, we have that $\Delta u(1) < 0$ and the linearised equation does have a non-trivial solution with boundary conditions Eq. (A.6). This means that the necessary condition for $u^{(0)}(x)$ corresponding to a minimum does not hold, and the buckled profile with $x_0 > 1/4$ is unstable. On the other hand, if $x_0 < 1/4$, we have $\Delta u(1) > 0$ and $\Delta u(x)$ does not change sign in $[0, 1]$. This implies that there is no choice of $a \leq 1$ that gives a non-vanishing solution of the linearised equation, the sufficient conditions for $u^{(0)}(x)$ giving a relative minimum of the free energy hold, and this profile is stable.

A.2 Effective Hamiltonian for the pseudo-spins

We start by deriving the pseudo-spins' marginal probability $\mathcal{P}(\boldsymbol{\sigma})$ by integrating the canonical distribution $\mathcal{P}(\boldsymbol{u}, \boldsymbol{p}, \boldsymbol{\sigma})$ over the string degrees of freedom. To do so, we rewrite Eq. (2.1) in matrix form,

$$\mathcal{H} = \frac{1}{2m}\boldsymbol{p}^{\boldsymbol{T}}\boldsymbol{p} + \frac{k}{2}\boldsymbol{u}^{\boldsymbol{T}}\boldsymbol{K}\boldsymbol{u} - f\boldsymbol{u}^{\boldsymbol{T}}\boldsymbol{\sigma} + J\boldsymbol{\sigma}^{\boldsymbol{T}}\boldsymbol{J}\boldsymbol{\sigma}, \tag{A.10}$$

in which $(\boldsymbol{u}, \boldsymbol{p}, \boldsymbol{\sigma})$ are now column matrices of dimension N, $(\boldsymbol{u}^{\boldsymbol{T}}, \boldsymbol{p}^{\boldsymbol{T}}, \boldsymbol{\sigma}^{\boldsymbol{T}})$ are their respective transpose matrices, and $\boldsymbol{J}$ and $\boldsymbol{K}$ are symmetric matrices of dimension N, namely

$$\boldsymbol{J} = \begin{bmatrix} 0 & \frac{1}{2} & & & \\ \frac{1}{2} & 0 & \frac{1}{2} & & \\ & \frac{1}{2} & 0 & \frac{1}{2} & \\ & & & \ddots & \\ & & & \frac{1}{2} & 0 \end{bmatrix}, \qquad \boldsymbol{K} = \begin{bmatrix} 2 & -1 & & & \\ -1 & 2 & -1 & & \\ & -1 & 2 & -1 & \\ & & & \ddots & \\ & & & -1 & 2 \end{bmatrix}. \tag{A.11}$$

Also, we make the following change of variables, $\boldsymbol{u} = \boldsymbol{v} + fk^{-1}\boldsymbol{\Lambda}\boldsymbol{\sigma}$, where $\boldsymbol{\Lambda}$ is the inverse of the matrix $\boldsymbol{K}$,

$$\boldsymbol{\Lambda}_{ij} = \frac{1}{N+1}j(N-i+1) > 0, \quad \forall i \geq j, \quad \boldsymbol{\Lambda}_{ij} = \boldsymbol{\Lambda}_{ji}, \tag{A.12}$$

see below for details on the derivation of the elements of $\boldsymbol{\Lambda}$.

Interestingly, the variables $(\boldsymbol{v}, \boldsymbol{p})$ and $\boldsymbol{\sigma}$ become decoupled in the Hamiltonian, making it easy to integrate the canonical distribution over $(\boldsymbol{v}, \boldsymbol{p})$. The result is

$$\mathcal{P}(\boldsymbol{\sigma}) \propto e^{-\mathcal{H}_{\text{eff}}(\boldsymbol{\sigma})/\theta}, \quad \mathcal{H}_{\text{eff}}(\boldsymbol{\sigma}) = \kappa\,\boldsymbol{\sigma}^{\boldsymbol{T}}\boldsymbol{J}\boldsymbol{\sigma} - \frac{\pi^2}{2N^2}\boldsymbol{\sigma}^{\boldsymbol{T}}\boldsymbol{\Lambda}\boldsymbol{\sigma}, \tag{A.13}$$

which is Eq. (2.23) of the main text.

Now, we derive the explicit expression of the elements of the matrix $\boldsymbol{\Lambda} = \boldsymbol{K}^{-1}$. From equation Eq. (A.11), we can directly calculate the determinant of the matrix $\boldsymbol{K}_n$ ($\boldsymbol{K}$-matrix with dimension n) as

$$\det(\boldsymbol{K}_1) = 2, \quad \det(\boldsymbol{K}_2) = 3, \tag{A.14a}$$
$$\det(\boldsymbol{K}_n) = 2\det(\boldsymbol{K}_{n-1}) - \det(\boldsymbol{K}_{n-2}). \tag{A.14b}$$

Hence,

$$\det(\boldsymbol{K}_n) = n+1. \tag{A.15}$$

We take advantage of $\boldsymbol{K}$ being a symmetric matrix $\boldsymbol{K} = \boldsymbol{K^T}$, and impose $i \geq j$ when calculating $\boldsymbol{\Lambda}_{ij}$, which is also symmetric. Then, for dimension N

$$\begin{aligned}\boldsymbol{\Lambda}_{ij} &= \frac{1}{N+1}(-1)^{i+j}\det(\boldsymbol{K}_{j-1})(-1)^{i-j}\det(\boldsymbol{K}_{N-i}) \\ &= \frac{1}{N+1}j(N-i+1),\end{aligned} \tag{A.16}$$

where we have made use of

$$\det\begin{pmatrix}\boldsymbol{A} & \boldsymbol{0} \\ \boldsymbol{B} & \boldsymbol{C}\end{pmatrix} = \det(\boldsymbol{A})\det(\boldsymbol{C}), \tag{A.17}$$

in which $\boldsymbol{A}$, $\boldsymbol{B}$ and $\boldsymbol{C}$ are non-zero matrices and $\boldsymbol{0}$ the zero matrix.

A.3 Effective Hamiltonian landscape

We want to characterise the $\mathcal{H}_{\text{eff}}$ landscape as κ is modified, where the phase space is formed by all possible configurations of $\boldsymbol{\sigma}$. For small enough κ, the completely ferromagnetic configuration with all the pseudo-spins pointing up (or down) minimises Eq. (A.13). On the other hand, as κ increases the configuration minimising Eq. (A.13) changes. Let us start from a completely ordered ferromagnetic configuration $\boldsymbol{\sigma}_{\text{ferro}}$, in which $\sigma_i = +1$, $\forall i$, and change the sign of σ_l, thereby obtaining the configuration $R_l\boldsymbol{\sigma}_{\text{ferro}}$. The additional contribution to the free energy is

$$\Delta\mathcal{H}_{\text{eff}} \equiv \mathcal{H}_{\text{eff}}(R_l\boldsymbol{\sigma}_{\text{ferro}}) - \mathcal{H}_{\text{eff}}(\boldsymbol{\sigma}_{\text{ferro}}) = \frac{\pi^2}{2N^2}\sum_{i\neq l}^{N}\boldsymbol{K}^{-1}_{l,i} - \kappa, \tag{A.18}$$

where

$$\sum_{i\neq l}^{N}\boldsymbol{K}^{-1}_{l,i} = \frac{(N-1)(N+1-l)l}{2(N+1)}. \tag{A.19}$$

This positive expression has a maximum at the centre, $l = (N+1)/2$, and therefore $\Delta\mathcal{H}_{\text{eff}}$ is minimum when the flipping pseudo-spins are those at the borders of the chain. This suggests that, as κ increases, the most probable (minimum free energy) state will become antiferromagnetic at both boundaries while remaining ferromagnetic in the bulk.

Now we can analyse the behaviour of this global minimum with increasing κ. In light of the discussion above, we restrict ourselves to configurations in which n_a consecutive antiferromagnetic links have been created at each boundary, see Fig. 2.3. We denote by $\mathcal{H}_{\text{eff}}(n_a)$ the value of the effective

Hamiltonian for such a configuration. Since n_a increases by two, we are interested in evaluating $\mathcal{H}_{\text{eff}}(n_a) - \mathcal{H}_{\text{eff}}(n_a - 2)$. Using Eq. (A.13), taking into account the symmetries of $\boldsymbol{K}$ and $\boldsymbol{J}$, and that we only have to take care of the terms that change their sign from $\mathcal{H}_{\text{eff}}(n_a)$ to $\mathcal{H}_{\text{eff}}(n_a - 2)$, we get the expression

$$\begin{aligned}\mathcal{H}_{\text{eff}}(n_a) - \mathcal{H}_{\text{eff}}(n_a - 2) = \frac{4\pi^2}{N^2}\Bigg[\sum_{j=1}^{n_a-1}(-1)^j \frac{j(N-n_a+1)}{N+1} \\ + \sum_{i=n_a+1}^{N-n_a} \frac{n_a(N-i+1)}{N+1} + \sum_{i=N-n_a+2}^{N}(-1)^{i+1}\frac{(N-i+1)n_a}{N+1}\Bigg] - 8\kappa. \qquad \text{(A.20)}\end{aligned}$$

After some simplifications,

$$\mathcal{H}_{\text{eff}}(n_a) - \mathcal{H}_{\text{eff}}(n_a - 2) = \frac{2\pi^2}{N^2}\left[-1 + (1 + N - 2n_a)\, n_a\right] - 8\kappa, \qquad \text{(A.21)}$$

which is Eq. (2.26) of the main text.

Appendix B

Appendices for chapters 3 and 4

B.1 Geometrical expressions for the 2-D spin-membrane model

We want our hexagonal lattice to have equal overall length and height. Let $n \equiv i_{max}$ be the total number of rows. Then

$$j_{max} = \text{IntegerPart}\left[\frac{3(n-1)+1}{\sqrt{3}} + 1\right], \tag{B.1}$$

is the total number of columns, and the height of the hexagonal lattice is

$$\tilde{L} = \frac{3(n-1)+1}{2}\tilde{l}, \tag{B.2}$$

where $\tilde{l}$ is the length of the side of a unit hexagonal cell. With these expressions, if $n = 25$, then $j_{max} = 43$ and the vertical and horizontal side of the lattice are 1 and 0.997 respectively, in units of $\tilde{L}$. Our finite hexagonal lattice is then roughly inscribed in a square and the nondimensional side of the unit hexagonal cell is $l = \tilde{l}/\tilde{L} = 0.027$.

B.2 Matsubara frequency sum

The sum over Matsubara frequencies in the expression on the right side of equation (5.20) gives [107]

$$\frac{1}{\beta}\sum_{\omega_n'}\frac{i\omega_n'}{(i\omega_n'-\alpha)^2-v_F^2q^2}=\frac{1}{2\beta}\sum_{\omega_n'}\left(\frac{1}{i\omega_n'-\alpha-v_Fq}+\frac{1}{i\omega_n'-\alpha+v_Fq}\right.$$
$$\left.+\frac{2\alpha}{(i\omega_n'-\alpha)^2-v_F^2q^2}\right)=\frac{1}{2}\left(\frac{1}{1+e^{\beta(\alpha+v_Fq)}}+\frac{1}{1+e^{\beta(\alpha-v_Fq)}}\right)\tag{B.3}$$
$$+\frac{\alpha}{2qv_F}\left(\frac{1}{1+e^{\beta(\alpha+v_Fq)}}-\frac{1}{1+e^{\beta(\alpha-v_Fq)}}\right)=\frac{1}{2qv_F}\times\left(\frac{\alpha+v_Fq}{1+e^{\beta(\alpha+v_Fq)}}\right.$$
$$\left.-\frac{\alpha-v_Fq}{1+e^{\beta(\alpha-v_Fq)}}\right)=\frac{1}{2qv_F}\left(\frac{\alpha+v_Fq}{1+e^{\beta(\alpha+v_Fq)}}-\frac{v_Fq-\alpha}{1+e^{\beta(v_Fq-\alpha)}}\right)+\frac{v_Fq-\alpha}{2qv_F}.$$

Then

$$\frac{4}{\beta}\int_q\sum_{\omega_n'}\frac{i\omega_n'}{(i\omega_n'-\alpha)^2-v_F^2q^2}=\frac{1}{\pi v_F}\int_0^\Lambda\left(\frac{\alpha+v_Fq}{1+e^{\beta(\alpha+v_Fq)}}-\frac{v_Fq-\alpha}{1+e^{\beta(v_Fq-\alpha)}}\right)dq$$
$$+\frac{1}{\pi}\int_0^\Lambda\left(q-\frac{\alpha}{v_F}\right)dq=\frac{v_F\Lambda^2-2\alpha\Lambda}{2\pi v_F}-\frac{1}{\pi\beta^2v_F^2}\left(\int_{e^{-\beta(v_F\Lambda+\alpha)}}^{e^{-\beta\alpha}}\frac{\ln t\,dt}{1+t}-\int_{e^{-\beta(v_F\Lambda-\alpha)}}^{e^{\beta\alpha}}\frac{\ln t\,dt}{1+t}\right)\tag{B.4}$$

We now split the last integral on the right hand side of (B.4) as

$$\int_{e^{-\beta(v_F\Lambda-\alpha)}}^{e^{\beta\alpha}}\frac{\ln t\,dt}{1+t}=\left(\int_{e^{-\beta(v_F\Lambda-\alpha)}}^{1}+\int_1^{e^{\beta\alpha}}\right)\frac{\ln t\,dt}{1+t}$$
$$=\int_{e^{-\beta(v_F\Lambda-\alpha)}}^{1}\frac{\ln t\,dt}{1+t}-\int_1^{e^{\beta\alpha}}\frac{\ln t\,dt}{(1+t)t}+\frac{1}{2}(\ln t)^2\Big|_1^{e^{\beta\alpha}}\tag{B.5}$$
$$\sim\frac{\alpha^2\beta^2}{2}+\int_0^1\frac{\ln t\,dt}{1+t}-\int_1^\infty\frac{\ln t\,dt}{(1+t)t}=\frac{\alpha^2\beta^2}{2}-\frac{\pi^2}{6}.$$

The result is

$$\frac{4}{\beta}\int_q\sum_{\omega_n'}\frac{i\omega_n'}{(i\omega_n'-\alpha)^2-v_F^2q^2}\sim\frac{v_F\Lambda^2-2\alpha\Lambda}{2\pi v_F}+\frac{\alpha^2}{2\pi v_F^2}-\frac{\pi}{6\beta^2v_F^2},\tag{B.6}$$

because the other integrals are of order $O(e^{-\beta\alpha})\ll 1$. In these computations q is upper bounded by $\Lambda=2\pi/a$.

B.3 Selecting the chemical potential

Keeping a nonzero chemical potential, (5.20) and (5.21) yield

$$\sigma = -\frac{g\alpha}{V(0)}, \ \frac{\alpha}{V(0)} = \frac{4}{\beta}\int_q \sum_{\omega'_n} \frac{i\omega'_n}{(i\omega'_n - \alpha + \mu)^2 - v_F^2 q^2} \sim \frac{(\alpha - \mu - v_F\Lambda)^2 - \frac{\pi^2}{3\beta^2}}{2\pi v_F}. \tag{B.7}$$

These are two equations for three unknowns, σ, α and μ, so that we can give a value to μ and solve for σ and α. We have already seen the consequences of setting $\mu = 0$. What do we get from other choices?

1. Assume that μ is selected so that $\mu + v_F\Lambda = 0$ and therefore the right hand side of (B.7) (which represents the Fermionic propagator in real space for $x = 0$) becomes finite as $\Lambda \to \infty$. Following the same steps as in previous sections, e.g. using equations (5.23) and (5.31), we get (the minus sign corresponds to $g < 0$)

$$\frac{8\kappa\pi e^4}{g v_F^2 \epsilon_0^2}\gamma_{nm} = 1 \pm \sqrt{1 + \frac{2\pi^2 e^4}{9\epsilon_0^2 v_F^4 \beta^2}\frac{R^2}{\beta^2}}. \tag{B.8}$$

The right hand side of this equation contains the product $R/\beta = RT$. This produces a critical radius (at which the graphene sheet starts buckling) that decreases when the temperature increases. This is unphysical because increasing temperature would favor rippling, contrary to experimental evidence [13].

2. Let us set $R = \infty$ and $\alpha = 0$ in (B.7), thereby obtaining

$$\mu + v_F\Lambda = \pm\frac{\pi}{\sqrt{3}\beta}. \tag{B.9}$$

If α is no longer zero for finite radius, (5.23) gives

$$\alpha\left(\alpha \mp \frac{2\pi}{\sqrt{3}\beta} - \frac{2\pi v_F^2}{V(0)}\right) = 0. \tag{B.10}$$

Then either $\alpha = 0$ and $\sigma = 0$, which contradicts (5.31), or

$$\alpha = 2\pi\left(\pm\frac{1}{\sqrt{3}\beta} + \frac{v_F^2}{V(0)}\right). \tag{B.11}$$

In this case, the same arguments based on Equations (5.23) and (5.31) provide

$$\gamma_{nm}^2 = \frac{g\pi v_F^2\epsilon_0^2}{\kappa e^4} \pm \frac{g\pi\epsilon_0}{\sqrt{3}\kappa e^2}\frac{R}{\beta}. \tag{B.12}$$

Once the numerical values of the constants are taken into account, we notice that the left hand side of (B.12) is positive, whereas the second term in the right hand side of this equation (the minus sign corresponds to $g < 0$) is proportional to TR, and this again produces the same unphysical effect as before.

Thus we conclude that the physically meaningful choice of chemical potential is $\mu = 0$ as in [70]. We do not renormalize the parameters of the model and leave the natural ultraviolet and infrared cutoffs $\Lambda = 2\pi/a$ and $q_0 = 2\pi/R$, respectively, in terms of the lattice constant a and the radius R.

Bibliography

[1] AlGaAs Band structure and carrier concentration. http://www.ioffe.ru/SVA/NSM/Semicond/AlGaAs/bandstr.html. Accessed: 2017-06-13.

[2] Random.org. https://www.random.org/. Accessed: 2017-06-13.

[3] N. Abedpour, M. Neek-Amal, R. Asgari, F. Shahbazi, N. Nafari, and M. R. R. Tabar. Roughness of undoped graphene and its short-range induced gauge field. *Physical Review B*, 76(19):195407, 2007.

[4] M. Ackerman, P. Kumar, M. Neek-Amal, P. Thibado, F. Peeters, and S. Singh. Anomalous dynamical behavior of freestanding graphene membranes. *Physical Review Letters*, 117(12):126801, 2016.

[5] M. Alvaro, M. Carretero, and L. L. Bonilla. Noise-enhanced spontaneous chaos in semiconductor superlattices at room temperature. *EPL (Europhysics Letters)*, 107(3):37002, 2014.

[6] A. Amann, J. Schlesner, A. Wacker, and E. Schöll. Chaotic front dynamics in semiconductor superlattices. *Physical Review B*, 65(19):193313, 2002.

[7] D. J. Amit and V. Martin-Mayor. *Field theory, the renormalization group, and critical phenomena: graphs to computers*. World Scientific Publishing Co Inc, 2005.

[8] B. Amorim, A. Cortijo, F. de Juan, A. Grushin, F. Guinea, A. Gutiérrez-Rubio, H. Ochoa, V. Parente, R. Roldán, P. San-Jose, et al. Novel effects of strains in graphene and other two dimensional materials. *Physics Reports*, 617:1–54, 2016.

[9] B. Amorim, R. Roldán, E. Cappelluti, A. Fasolino, F. Guinea, and M. Katsnelson. Thermodynamics of quantum crystalline membranes. *Physical Review B*, 89(22):224307, 2014.

[10] J. A. Aronovitz and T. C. Lubensky. Fluctuations of solid membranes. *Physical Review Letters*, 60(25):2634, 1988.

[11] S. Asmussen and P. W. Glynn. *Stochastic simulation: algorithms and analysis*, volume 57. Springer Science & Business Media, 2007.

[12] U. Bangert, M. H. Gass, A. L. Bleloch, R. R. Nair, and A. K. Geim. Manifestation of ripples in free-standing graphene in lattice images obtained in an aberration-corrected scanning transmission electron microscope. *Phys. Status Solidi A*, 206(6):1117, 2009.

[13] W. Bao, F. Miao, Z. Chen, H. Zhang, W. Jang, C. Dames, and C. N. Lau. Controlled ripple texturing of suspended graphene and ultrathin graphite membranes. *Nature Nanotechnology*, 4(9):562–566, 2009.

[14] L. Berthier and J.-P. Bouchaud. Geometrical aspects of aging and rejuvenation in the ising spin glass: A numerical study. *Physical Review B*, 66(5):054404, 2002.

[15] E. Bertin, J. Bouchaud, J. Drouffe, and C. Godreche. The kovacs effect in model glasses. *Journal of physics A: mathematical and general*, 36(43):10701, 2003.

[16] K. Binder and A. P. Young. Spin glasses: Experimental facts, theoretical concepts, and open questions. *Reviews of Modern physics*, 58(4):801, 1986.

[17] M. K. Blees, A. W. Barnard, P. A. Rose, S. P. Roberts, K. L. McGill, P. Y. Huang, A. R. Ruyack, J. W. Kevek, B. Kobrin, D. A. Muller, et al. Graphene kirigami. *Nature*, 524(7564):204–207, 2015.

[18] K. I. Bolotin, K. Sikes, Z. Jiang, M. Klima, G. Fudenberg, J. Hone, P. Kim, and H. Stormer. Ultrahigh electron mobility in suspended graphene. *Solid State Communications*, 146(9):351–355, 2008.

[19] Y. Bomze, R. Hey, H. Grahn, and S. Teitsworth. Noise-induced current switching in semiconductor superlattices: observation of nonexponential kinetics in a high-dimensional system. *Physical Review Letters*, 109(2):026801, 2012.

[20] L. L. Bonilla. Theory of nonlinear charge transport, wave propagation, and self-oscillations in semiconductor superlattices. *Journal of Physics: Condensed Matter*, 14(14):R341, 2002.

[21] L. L. Bonilla, M. Alvaro, and M. Carretero. Chaos-based true random number generators. *Journal of Mathematics in Industry*, 7(1):1, 2016.

[22] L. L. Bonilla and A. Carpio. Model of ripples in graphene. *Physical Review B*, 86:195402, Nov 2012.

[23] L. L. Bonilla and A. Carpio. Ripples in a graphene membrane coupled to glauber spins. *Journal of Statistical Mechanics: Theory and Experiment*, 2012(09):P09015, 2012.

[24] L. L. Bonilla, A. Carpio, C. Gong, and J. Warner. Measuring strain and rotation fields at the dislocation core in graphene. *Physical Review B*, 92(15):155417, 2015.

[25] L. L. Bonilla, A. Carpio, A. Prados, and R. Rosales. Ripples in a string coupled to glauber spins. *Physical Review E*, 85(3):031125, 2012.

[26] L. L. Bonilla, J. Galán, J. Cuesta, F. Martínez, and J. Molera. Dynamics of electric-field domains and oscillations of the photocurrent in a simple superlattice model. *Physical Review B*, 50(12):8644, 1994.

[27] L. L. Bonilla and H. T. Grahn. Non-linear dynamics of semiconductor superlattices. *Reports on Progress in Physics*, 68(3):577, 2005.

[28] L. L. Bonilla, G. Platero, and D. Sánchez. Microscopic derivation of transport coefficients and boundary conditions in discrete drift-diffusion models of weakly coupled superlattices. *Physical Review B*, 62(4):2786, 2000.

[29] L. L. Bonilla, A. Prados, and A. Carpio. Nonequilibrium dynamics of a fast oscillator coupled to glauber spins. *Journal of Statistical Mechanics: Theory and Experiment*, 2010(09):P09019, 2010.

[30] L. L. Bonilla and M. Ruiz-Garcia. Critical radius and temperature for buckling in graphene. *Physical Review B*, 93(11):115407, 2016.

[31] L. L. Bonilla and S. W. Teitsworth. *Nonlinear wave methods for charge transport*. John Wiley & Sons, 2009.

[32] A. Bray. An introduction to the kinetics of first-order phase transitions. *Adv. Phys.*, 43:357, 1994.

[33] J. Brey and A. Prados. Calculation of the entropy from master equations with time-dependent transition probabilities. *Physical Review A*, 42(2):765, 1990.

[34] J. Brey and A. Prados. Dynamical behavior of a one-dimensional ising model submitted to continuous heating and cooling processes. *Physical Review B*, 49(2):984, 1994.

[35] A. Buhot. Kovacs effect and fluctuation–dissipation relations in 1d kinetically constrained models. *Journal of Physics A: Mathematical and General*, 36(50):12367, 2003.

[36] O. Bulashenko and L. L. Bonilla. Chaos in resonant-tunneling superlattices. *Physical Review B*, 52(11):7849, 1995.

[37] J. S. Bunch, A. M. Van Der Zande, S. S. Verbridge, I. W. Frank, D. M. Tanenbaum, J. M. Parpia, H. G. Craighead, and P. L. McEuen. Electromechanical resonators from graphene sheets. *Science*, 315(5811):490–493, 2007.

[38] D. C. Cabra, A. Honecker, and P. Pujol. *Modern theories of many-particle systems in condensed matter physics*, volume 843. Springer Science & Business Media, 2012.

[39] A. Carpio and L. L. Bonilla. Periodized discrete elasticity models for defects in graphene. *Physical Review B*, 78(8):085406, 2008.

[40] C. Carraro and D. R. Nelson. Grain-boundary buckling and spin-glass models of disorder in membranes. *Physical Review E*, 48(4):3082, 1993.

[41] P. M. Chaikin and T. C. Lubensky. *Principles of condensed matter physics*. Cambridge university press, 2000.

[42] C. J. Chen. *Introduction to scanning tunneling microscopy*, volume 4. Oxford University Press on Demand, 1993.

[43] P. Collet and J.-P. Eckmann. *Iterated maps on the interval as dynamical systems*. Springer Science & Business Media, 2009.

[44] J. Dervaux and M. B. Amar. Morphogenesis of growing soft tissues. *Physical Review Letters*, 101(6):068101, 2008.

[45] J. F. Dynes, Z. L. Yuan, A. W. Sharpe, and A. J. Shields. A high speed, postprocessing free, quantum random number generator. *applied physics letters*, 93(3):031109, 2008.

[46] S. F. Edwards and P. W. Anderson. Theory of spin glasses. *Journal of Physics F: Metal Physics*, 5(5):965, 1975.

[47] A. Eichler, J. Moser, J. Chaste, M. Zdrojek, I. Wilson-Rae, and A. Bachtold. Nonlinear damping in mechanical resonators made from carbon nanotubes and graphene. *Nature Nanotechnology*, 6(6):339–342, 2011.

[48] D. Espeso, A. Carpio, and B. Einarsson. Differential growth of wrinkled biofilms. *Physical Review E*, 91(2):022710, 2015.

[49] J. Evans, P. Thiel, and M. C. Bartelt. Morphological evolution during epitaxial thin film growth: Formation of 2d islands and 3d mounds. *Surface Science Reports*, 61(1):1–128, 2006.

[50] A. Fasolino, J. Los, and M. I. Katsnelson. Intrinsic ripples in graphene. *Nature Materials*, 6(11):858–861, 2007.

[51] C. Faugeras, B. Faugeras, M. Orlita, M. Potemski, R. R. Nair, and A. Geim. Thermal conductivity of graphene in corbino membrane geometry. *ACS Nano*, 4(4):1889–1892, 2010.

[52] J. Feder and E. Pytte. Statistical mechanics of the collective jahn-teller phase transition. *Physical Review B*, 8(8):3978, 1973.

[53] M. J. Feigenbaum. Quantitative universality for a class of nonlinear transformations. *Journal of statistical physics*, 19(1):25–52, 1978.

[54] M. J. Feigenbaum. Universal behavior in nonlinear systems. *Physica D: Nonlinear Phenomena*, 7(1-3):16–39, 1983.

[55] R. P. Feynman. *Statistical mechanics: a set of lectures*. Hachette UK, 1998.

[56] R. G. Gallager. *Principles of digital communication*, volume 1. Cambridge University Press Cambridge, UK:, 2008.

[57] L. Gammaitoni, P. Hänggi, P. Jung, and F. Marchesoni. Stochastic resonance. *Reviews of Modern Physics*, 70(1):223, 1998.

[58] H. Gang, T. Ditzinger, C.-Z. Ning, and H. Haken. Stochastic resonance without external periodic force. *Physical Review Letters*, 71(6):807, 1993.

[59] D. Gazit. Correlation between charge inhomogeneities and structure in graphene and other electronic crystalline membranes. *Physical Review B*, 80(16):161406, 2009.

[60] D. Gazit. Theory of the spontaneous buckling of doped graphene. *Physical Review B*, 79(11):113411, 2009.

[61] A. K. Geim. Random walk to graphene (nobel lecture). *Angewandte Chemie International Edition*, 50(31):6966–6985, 2011.

[62] I. Gelfand and S. Fomin. Calculus of variations,(translated and edited by silverman, ra), 2000.

[63] A. Georgi, P. Nemes-Incze, B. Szafranek, D. Neumaier, V. Geringer, M. Liebmann, and M. Morgenstern. Apparent rippling with honeycomb symmetry and tunable periodicity observed by scanning tunneling microscopy on suspended graphene. *Physical Review B*, 94(18):184302, 2016.

[64] R. J. Glauber. Time-dependent statistics of the ising model. *Journal of Mathematical Physics*, 4(2):294–307, 1963.

[65] C. Godreche. Dynamics of condensation in zero-range processes. *Journal of Physics A: Mathematical and General*, 36(23):6313, 2003.

[66] J. González. Rippling transition from electron-induced condensation of curvature field in graphene. *Physical Review B*, 90(16):165402, 2014.

[67] R. Graham. Squeezing and frequency changes in harmonic oscillations. *Journal of Modern Optics*, 34(6-7):873–879, 1987.

[68] R. B. Griffiths. Thermodynamic model for tricritical points in ternary and quaternary fluid mixtures. *The Journal of Chemical Physics*, 60(1):195–206, 1974.

[69] F. Guinea, B. Horovitz, and P. Le Doussal. Gauge field induced by ripples in graphene. *Physical Review B*, 77(20):205421, 2008.

[70] F. Guinea, P. Le Doussal, and K. J. Wiese. Collective excitations in a large-d model for graphene. *Physical Review B*, 89(12):125428, 2014.

[71] E. Guitter, F. David, S. Leibler, and L. Peliti. Crumpling and buckling transitions in polymerized membranes. *Physical Review Letters*, 61(26):2949, 1988.

[72] P. Hänggi, P. Talkner, and M. Borkovec. Reaction-rate theory: fifty years after kramers. *Reviews of modern physics*, 62(2):251, 1990.

[73] J. Hizanidis, A. Balanov, A. Amann, and E. Schöll. Noise-induced front motion: signature of a global bifurcation. *Physical Review Letters*, 96(24):244104, 2006.

[74] Y. Huang, W. Li, W. Ma, H. Qin, H. T. Grahn, and Y. Zhang. Spontaneous quasi-periodic current self-oscillations in a weakly coupled gaas/(al, ga) as superlattice at room temperature. *Applied Physics Letters*, 102(24):242107, 2013.

[75] Y. Huang, W. Li, W. Ma, H. Qin, and Y. Zhang. Experimental observation of spontaneous chaotic current oscillations in gaas/al 0.45 ga 0.55 as superlattices at room temperature. *Chinese Science Bulletin*, 57(17):2070–2072, 2012.

[76] Y. Huang, H. Qin, W. Li, S. Lu, J. Dong, H. T. Grahn, and Y. Zhang. Experimental evidence for coherence resonance in a noise-driven gaas/alas superlattice. *EPL (Europhysics Letters)*, 105(4):47005, 2014.

[77] J. Kanamori. Crystal distortion in magnetic compounds. *Journal of Applied Physics*, 31(5):S14–S23, 1960.

[78] I. Kanter, Y. Aviad, I. Reidler, E. Cohen, and M. Rosenbluh. An optical ultrafast random bit generator. *Nature Photonics*, 4(1):58–61, 2010.

[79] M. Kardar. *8.334 Statistical Mechanics II: Statistical Physics of Fields*. Massachusetts Institute of Technology, 2014.

[80] E. Kats and V. Lebedev. Asymptotic freedom at zero temperature in free-standing crystalline membranes. *Physical Review B*, 89(12):125433, 2014.

[81] M. Katsnelson and A. Geim. Electron scattering on microscopic corrugations in graphene. *Philosophical Transactions of the Royal Society of London A: Mathematical, Physical and Engineering Sciences*, 366(1863):195–204, 2008.

[82] M. I. Katsnelson. *Graphene: carbon in two dimensions*. Cambridge University Press, 2012.

[83] E.-A. Kim and A. C. Neto. Graphene as an electronic membrane. *EPL (Europhysics Letters)*, 84(5):57007, 2008.

[84] D. Kirilenko, A. Dideykin, and G. Van Tendeloo. Measuring the corrugation amplitude of suspended and supported graphene. *Physical Review B*, 84(23):235417, 2011.

[85] W. Kob and R. Schilling. Dynamics of a one-dimensional glass model: Ergodicity and nonexponential relaxation. *Physical Review A*, 42(4):2191, 1990.

[86] J. Kotakoski, F. R. Eder, and J. C. Meyer. Atomic structure and energetics of large vacancies in graphene. *Physical Review B*, 89(20):201406, 2014.

[87] Y. A. Kuznetsov. *Elements of applied bifurcation theory*, volume 112. Springer Science & Business Media, 2013.

[88] L. D. Landau and E. M. Lifshitz. *Course of theoretical physics*. Elsevier, 2013.

[89] C. Lee, X. Wei, J. W. Kysar, and J. Hone. Measurement of the elastic properties and intrinsic strength of monolayer graphene. *Science*, 321(5887):385–388, 2008.

[90] O. Lehtinen, S. Kurasch, A. Krasheninnikov, and U. Kaiser. Atomic scale study of the life cycle of a dislocation in graphene from birth to annihilation. *Nature Communications*, 4, 2013.

[91] W. Li, Y. Aviad, I. Reidler, H. Song, Y. Huang, K. Biermann, M. Rosenbluh, Y. Zhang, H. T. Grahn, and I. Kanter. Chaos synchronization in networks of semiconductor superlattices. *EPL (Europhysics Letters)*, 112(3):30007, 2015.

[92] W. Li, I. Reidler, Y. Aviad, Y. Huang, H. Song, Y. Zhang, M. Rosenbluh, and I. Kanter. Fast physical random-number generation based on room-temperature chaotic oscillations in weakly coupled superlattices. *Physical Review Letters*, 111(4):044102, 2013.

[93] N. Lindahl, D. Midtvedt, J. Svensson, O. A. Nerushev, N. Lindvall, A. Isacsson, and E. E. Campbell. Determination of the bending rigidity of graphene via electrostatic actuation of buckled membranes. *Nano Letters*, 12(7):3526–3531, 2012.

[94] A. Locatelli, K. R. Knox, D. Cvetko, T. O. Mentes, M. A. Nino, S. Wang, M. B. Yilmaz, P. Kim, R. M. Osgood Jr, and A. Morgante. Corrugation in exfoliated graphene: an electron microscopy and diffraction study. *ACS Nano*, 4(8):4879–4889, 2010.

[95] C. H. Lui, L. Liu, K. F. Mak, G. W. Flynn, and T. F. Heinz. Ultraflat graphene. *Nature*, 462(7271):339–341, 2009.

[96] K. Luo, H. Grahn, K. Ploog, and L. Bonilla. Explosive bifurcation to chaos in weakly coupled semiconductor superlattices. *Physical review letters*, 81(6):1290, 1998.

[97] Y. Mao, W. L. Wang, D. Wei, E. Kaxiras, and J. G. Sodroski. Graphene structures at an extreme degree of buckling. *ACS Nano*, 5(2):1395–1400, 2011.

[98] J. Martin, N. Akerman, G. Ulbricht, T. Lohmann, J. v. Smet, K. Von Klitzing, and A. Yacoby. Observation of electron–hole puddles in graphene using a scanning single-electron transistor. *Nature Physics*, 4(2):144–148, 2008.

[99] J. C. Meyer, A. K. Geim, M. I. Katsnelson, K. S. Novoselov, T. J. Booth, and S. Roth. The structure of suspended graphene sheets. *Nature*, 446(7131):60–63, 2007.

[100] M. Mézard, G. Parisi, and M. Virasoro. *Spin glass theory and beyond: An Introduction to the Replica Method and Its Applications*, volume 9. World Scientific Publishing Co Inc, 1987.

[101] T. E. Murphy and R. Roy. Chaotic lasers: The world's fastest dice. *Nature Photonics*, 2(12):714–715, 2008.

[102] M. Neek-Amal, P. Xu, J. Schoelz, M. Ackerman, S. Barber, P. Thibado, A. Sadeghi, and F. Peeters. Thermal mirror buckling in freestanding graphene locally controlled by scanning tunnelling microscopy. *Nature Communications*, 5, 2014.

[103] D. Nelson and L. Peliti. Fluctuations in membranes with crystalline and hexatic order. *Journal de Physique*, 48(7):1085–1092, 1987.

[104] D. Nelson, T. Piran, and S. Weinberg. *Statistical mechanics of membranes and surfaces.* World Scientific, 2004.

[105] A. C. Neto, F. Guinea, N. M. Peres, K. S. Novoselov, and A. K. Geim. The electronic properties of graphene. *Reviews of Modern Physics*, 81(1):109, 2009.

[106] M. A. Nielsen and I. L. Chuang. Quantum computation and quantum information (cambridge series on information and the natural sciences). 2004.

[107] A. Nieto. Evaluating sums over the matsubara frequencies. *Computer Physics Communications*, 92(1):54–64, 1995.

[108] K. S. Novoselov, A. K. Geim, S. Morozov, D. Jiang, M. Katsnelson, I. Grigorieva, S. Dubonos, and A. Firsov. Two-dimensional gas of massless dirac fermions in graphene. *Nature*, 438(7065):197–200, 2005.

[109] K. S. Novoselov, A. K. Geim, S. V. Morozov, D. Jiang, Y. Zhang, S. V. Dubonos, I. V. Grigorieva, and A. A. Firsov. Electric field effect in atomically thin carbon films. *Science*, 306(5696):666–669, 2004.

[110] A. O'Hare, F. Kusmartsev, and K. Kugel. A stable "flat" form of two-dimensional crystals: Could graphene, silicene, germanene be minigap semiconductors? *Nano Letters*, 12(2):1045–1052, 2012.

[111] L. Onsager. Crystal statistics. i. a two-dimensional model with an order-disorder transition. *Physical Review*, 65(3-4):117, 1944.

[112] F.-J. Pérez-Reche, L. Truskinovsky, and G. Zanzotto. Driving-induced crossover: from classical criticality to self-organized criticality. *Physical review letters*, 101(23):230601, 2008.

[113] A. Prados, L. L. Bonilla, and A. Carpio. Phase transitions in a mechanical system coupled to glauber spins. *Journal of Statistical Mechanics: Theory and Experiment*, 2010(06):P06016, 2010.

[114] A. Prados, J. Brey, and B. Sánchez-Rey. A dynamical monte carlo algorithm for master equations with time-dependent transition rates. *Journal of statistical physics*, 89(3):709–734, 1997.

[115] E. Pytte. Dynamics of jahn-teller phase transitions. *Physical Review B*, 8(8):3954, 1973.

[116] I. Reidler, Y. Aviad, M. Rosenbluh, and I. Kanter. Ultrahigh-speed random number generation based on a chaotic semiconductor laser. *Physical Review Letters*, 103(2):024102, 2009.

[117] H. Rieger. Nonequilibrium dynamics and aging in the three-dimensional ising spin-glass model. *Journal of Physics A: Mathematical and General*, 26(15):L615, 1993.

[118] P. Rikvold. Stochastic model for the dynamics of a spin-oscillator coupled system. *Zeitschrift für Physik B Condensed Matter*, 26(2):195–199, 1977.

[119] P. Rikvold. (17) a spin-oscillator coupled approximation for the statics and dynamics of a fourth order anharmonic lattice. 1980.

[120] A. W. Robertson, K. He, A. I. Kirkland, and J. H. Warner. Inflating graphene with atomic scale blisters. *Nano Letters*, 14(2):908–914, 2014.

[121] R. Roldán, A. Fasolino, K. V. Zakharchenko, and M. I. Katsnelson. Suppression of anharmonicities in crystalline membranes by external strain. *Physical Review B*, 83(17):174104, 2011.

[122] M. A. Ruderman and C. Kittel. Indirect exchange coupling of nuclear magnetic moments by conduction electrons. *Physical Review*, 96(1):99, 1954.

[123] M. Ruiz-García, L. L. Bonilla, and A. Prados. Ripples in hexagonal lattices of atoms coupled to glauber spins. *Journal of Statistical Mechanics: Theory and Experiment*, 2015(5):P05015, 2015.

[124] M. Ruiz-García, L. L. Bonilla, and A. Prados. Stm-driven transition from rippled to buckled graphene in a spin-membrane model. *Physical Review B*, 94:205404, Nov 2016.

[125] M. Ruiz-García and A. Prados. Kovacs effect in the one-dimensional ising model: A linear response analysis. *Physical Review E*, 89(1):012140, 2014.

[126] R. Saito, G. Dresselhaus, and M. S. Dresselhaus. *Physical properties of carbon nanotubes*. World scientific, 1998.

[127] P. San-Jose, J. González, and F. Guinea. Electron-induced rippling in graphene. *Physical Review Letters*, 106(4):045502, 2011.

[128] S. Sarbach and M. E. Fisher. Tricritical coexistence in three dimensions: The multicomponent limit. *Physical Review B*, 20(7):2797, 1979.

[129] T. Schneider and E. Stoll. Molecular-dynamics investigation of structural phase transitions. *Physical Review Letters*, 31(20):1254, 1973.

[130] J. Schoelz, P. Xu, V. Meunier, P. Kumar, M. Neek-Amal, P. Thibado, and F. Peeters. Graphene ripples as a realization of a two-dimensional ising model: A scanning tunneling microscope study. *Physical Review B*, 91(4):045413, 2015.

[131] M. Sciamanna and K. A. Shore. Physics and applications of laser diode chaos. *Nature Photonics*, 9(3):151–162, 2015.

[132] H. Seung and D. R. Nelson. Defects in flexible membranes with crystalline order. *Physical Review A*, 38(2):1005, 1988.

[133] J. E. Shore and R. Zwanzig. Dielectric relaxation and dynamic susceptibility of a one-dimensional model for perpendicular-dipole polymers. *The Journal of Chemical Physics*, 63(12):5445–5458, 1975.

[134] D. R. Stinson. *Cryptography: theory and practice*. CRC press, 2005.

[135] S. H. Strogatz. Exploring complex networks. *Nature*, 410(6825):268–276, 2001.

[136] J. Svensson, N. Lindahl, H. Yun, M. Seo, D. Midtvedt, Y. Tarakanov, N. Lindvall, O. Nerushev, J. Kinaret, S. Lee, et al. Carbon nanotube field effect transistors with suspended graphene gates. *Nano Letters*, 11(9):3569–3575, 2011.

[137] A. Uchida, K. Amano, M. Inoue, K. Hirano, S. Naito, H. Someya, I. Oowada, T. Kurashige, M. Shiki, S. Yoshimori, et al. Fast physical random bit generation with chaotic semiconductor lasers. *Nature Photonics*, 2(12):728–732, 2008.

[138] J. van Hemmen and I. Morgenstern. Heidelberg colloquium on glassy dynamics. In *Lecture Notes in Physics, Berlin Springer Verlag*, volume 275, 1987.

[139] M. A. Vozmediano, M. Katsnelson, and F. Guinea. Gauge fields in graphene. *Physics Reports*, 496(4):109–148, 2010.

[140] P. R. Wallace. The band theory of graphite. *Physical Review*, 71(9):622, 1947.

[141] W. L. Wang, S. Bhandari, W. Yi, D. C. Bell, R. Westervelt, and E. Kaxiras. Direct imaging of atomic-scale ripples in few-layer graphene. *Nano letters*, 12(5):2278–2282, 2012.

[142] K. Wiesenfeld and F. Moss. Stochastic resonance and the benefits of noise: from ice ages to crayfish and squids. *Nature*, 373(6509):33, 1995.

[143] P. Xu, M. Neek-Amal, S. Barber, J. Schoelz, M. Ackerman, P. Thibado, A. Sadeghi, and F. Peeters. Unusual ultra-low-frequency fluctuations in freestanding graphene. *Nature Communications*, 5, 2014.

[144] P. Xu, Y. Yang, S. Barber, M. Ackerman, J. Schoelz, D. Qi, I. A. Kornev, L. Dong, L. Bellaiche, S. Barraza-Lopez, et al. Atomic control of strain in freestanding graphene. *Physical Review B*, 85(12):121406, 2012.

[145] J. M. Yeomans. *Statistical mechanics of phase transitions.* Clarendon Press, 1992.

[146] Z. Yin, H. Song, Y. Zhang, M. Ruiz-Garcia, M. Carretero, L. L. Bonilla, K. Biermann, and H. T. Grahn. Noise-enhanced chaos in a weakly coupled gaas/(al, ga) as superlattice. *Physical Review B*, 95:012218, 2017.

[147] R. Zan, C. Muryn, U. Bangert, P. Mattocks, P. Wincott, D. Vaughan, X. Li, L. Colombo, R. S. Ruoff, B. Hamilton, et al. Scanning tunnelling microscopy of suspended graphene. *Nanoscale*, 4(10):3065–3068, 2012.

[148] Y. Zhang, J. Kastrup, R. Klann, K. H. Ploog, and H. T. Grahn. Synchronization and chaos induced by resonant tunneling in gaas/alas superlattices. *Physical review letters*, 77(14):3001, 1996.

[149] C. Zhou, J. Kurths, and B. Hu. Array-enhanced coherence resonance: nontrivial effects of heterogeneity and spatial independence of noise. *Physical Review Letters*, 87(9):098101, 2001.